# Chapter 6

## Stratospheric Chemistry

**Lead Authors:** Martyn Chipperfield & Douglas Kinnison

**Co-Authors:** Slimane Bekki
Huisheng Bian
Christoph Brühl
Tim Canty
Irene Cionni
Sandip Dhomse
Lucien Froidevaux
Ryan Fuller
Rolf Müller
Michael Prather
Ross Salawich
Michelle Santee
Wenshou Tian
Simone Tilmes

**Acknowledgements:** Anu Dudhia, Ben Johnson, Ashley Jones, Perrine Lemennais, Beiping Luo, Alexei Rozanov, Virginie Poulain, Bjorn-Martin Sinnbuer, Jo Urban, Kaley Walker

## 6.1 Introduction

An accurate representation of atmospheric chemistry is a key component of a coupled CCM. Clearly, a realistic chemistry scheme is a requirement for reliable predictions of key trace gases, but it is also essential for realistic climate simulations. Aside from $CO_2$, the stratospheric distribution of the other major GHGs is partly determined by atmospheric chemistry.

CCMs are comprised of an underlying general circulation model (GCM) coupled to a chemistry module. The inclusion of detailed chemistry tends to add significantly to the computational cost both through the expense of solving the chemistry and the cost of additional tracers. The expense and complexity of the CCMs mean that evaluation of the models is difficult and time consuming. This is particularly true if the chemistry scheme has been developed 'online' within the CCM. A useful strategy for many CCMs is to use the same chemistry module in simpler models, *e.g.*, 3-D chemical transport models or 2-D models, so that more simulations can be performed. In any case, the evaluation of the climatological CCM simulations with observations is problematic. If enough observations exist then mean distributions can be compared but this is not generally possible with campaign data. Therefore, alternative approaches to evaluation are needed.

The aim of this chapter is to evaluate the chemical schemes of current CCMs using, where possible, a process-based approach or otherwise climatological observations. This builds on the proposals for chemical validation contained in Eyring *et al*. (2005), which are summarized in **Table 6.1**. The proposed processes to evaluate CCMs can be separated into the four areas of (i) photolysis rates, (ii) fast radical chemistry, (iii) reservoir and longer-lived species and (iv) polar chemistry. The remainder of this chapter is therefore structured along these lines. Section 6.2 describes some relevant aspects of how CCMs are formulated. The main results of the evaluation are contained in Section 6.3, which is divided into the 4 areas listed above and summarized in Table 6.1. Each subsection summarizes the performance of the models in the form of a grading. The overall performance of each model is then summarized in Section 6.4.

## 6.2 Formulation of Chemical Schemes

Details of the chemistry schemes included in the CCMs are given in Chapter 2. Although there are differences in detail, all of the models essentially contain a description of the main chemical species of relevance for stratospheric ozone, contained in the $O_x$, $HO_y$, $Cl_y$, $NO_y$, $Br_y$ chemical families (where x or y denotes the total components for the given family) and the relevant source gases (except E39CA does not include bromine chemistry). The models also contain a treatment of heterogeneous chemistry on sulfate aerosols and polar stratospheric clouds (PSCs). However, these aerosol/PSC schemes are based on an equilibrium approach where the models condense gas-phase species (*e.g.*, $H_2O$, $HNO_3$) onto a specified distribution of particle number density or size. Therefore, the models evaluated here do not contain explicit microphysics. The surface area density of sulfate aerosols in the CCMVal runs is specified from a provided climatology.

As stratospheric CCMs have evolved by a number of different pathways, a full chemistry evaluation needs to consider the explicit reactions schemes contained in the model. Clearly all CCMs aim to have a chemistry scheme sufficient to model stratospheric ozone accurately, but comparisons presented in this chapter, and elsewhere, can show very different model behaviour. Tables 6S.1, 6S.2 and 6S.3 in the Supplementary Material list the chemical species, gas-phase reactions and photolytic reactions, respectively, for each CCM and the photostationary state (PSS) model used in Section 6.3.2. The species and reactions listed are those important enough to be considered for inclusion in a global stratospheric CCM. Where individual models have ignored species and/or reactions the implications of this should be investigated further. Specific cases where the simplifications in the chemistry scheme have clearly affected model performance are mentioned below. Note that the description of the heterogeneous chemistry in the CCMs is provided in Chapter 2.

## 6.3 Evaluation of CCMs

This section evaluates the performance of the CCMs in four principal areas (see Table 6.1). Subsection 6.3.1 deals with photolysis rates. Subsection 6.3.2 covers fast radical chemistry outside of the polar winter/spring. Subsection 6.3.3 investigates reservoir species and long-lived tracers. Finally, Subsection 6.3.4 evaluates the performance of the models for chemistry related to polar ozone depletion. Throughout this analysis, output is taken from either the CCMVal-2 REF-B1 or REF-B2 simulations.

Throughout this chapter, quantitative estimates of CCM performance for a range of diagnostics have been obtained by using a formula based on the grades from Douglass *et al*. (1999) and Waugh and Eyring (2008):

$$g = 1 - \left( \frac{1}{N} \right) \left[ \sum \frac{| \mu^i_{CCM} - \mu^i_{obs} |}{n\sigma} \right] \qquad (6.1)$$

where $N$ is an averaging factor, $\mu_{CCM}$ is the model climatological mean and $\mu_{obs}$ is the observed climatological mean and $\sigma$ is a measure of the uncertainty. The value of $n$ can be chosen to give a spread in $g$; if $n = 3$ then a value of $g = 0$ indicates the model mean is three times the error away from the observed mean. More discussion of this approach

**Table 6.1:** List of core processes to validate chemistry in CCMs with a focus on their ability to accurately model stratospheric ozone. The diagnostics which are used as quantitative metrics for the overall model assessment are highlighted in gray.

| Process | Diagnostic | Variables | Data | References[a] |
|---|---|---|---|---|
| ***Photolysis Rates*** | | | | |
| Accuracy of high-sun photolysis rates | Single profiles (0-80 km), also with clouds and aerosols | $Js^b$ | None | *Prather and Remsberg (1993)* |
| Accuracy of low-sun photolysis rates (spherical atmospheres, polar chemistry) | Noon, midnight & average profiles | Js | None | |
| Accuracy of wavelength binning (290-400 nm) | Single profile (0-24 km) | J-$O_3$ ($^1$D), J-$O_3$, and J-$NO_2$ | IPMMI transfer std with TUV | |
| ***Short time scale chemical processes*** | | | | |
| Offline box model comparisons of fast chemistry | Profiles and tracer-tracer correlations of radical precursors | $N_2O$, O3, $NO_y^b$, $Cl_y^b$, $Br_y^b$ | Balloon, shuttle, aircraft, and satellite obs. | *Gao et al. (2001); Salawitch et al. (1994a)* |
| | Profiles, tracer-tracer correlations, and partitioning of radicals | O($^3$P), O($^1$D), $HO_x^b$, $NO_x^b$, ClO, BrO, $Cl_y$, $Br_y$, $NO_y$ | Same as above | *Pierson et al. (2000); Park et al. (1999)* |
| ***Long time scale chemical processes*** | | | | |
| Comparisons of source gases and reservoir species to observational climatologies | Tracer-tracer correlations | $NO_y$, $N_2O$, $CH_4$, $H_2O$ | Balloon, aircraft and MIPAS obs. | *Chang et al. (1996); Fahey et al. (1996); Müller et al. (1997)* |
| | Mean annual cycle @1hPa and 50hPa | BrO, CO, HCl, $ClONO_2$, $N_2O_5$, $N_2O$, $HNO_3$, $CH_4$, $H_2O$, $O_3$ | ACE-FTS, MIPAS, ODIN, SCIAMACHY | *Millard et al. (2002); Salawitch et al. (2002); Sen et al. (1998)* |
| | Mean Profiles @30°-60°S | Same as above | Same as above | Same as above |
| Long-term variation of reservoir and radical species | Comparison of total column at selected ground based stations | HCl, $ClONO_2$, $NO_2$ | NDACC | *Rinsland et al. (2003)* |
| | Evolution of model results from 1960-2100; PoLS; EqUS; ExtrpLS | $NO_y$, $Cl_y$, $Br_y$, $N_2O$, $CH_4$, $O_3$, $H_2O$ | None, model/ model comparison | *Eyring et al. (2007)* |
| | Summation of total organic and inorganic bromine and chlorine | $TCl_y^b$, $TBr_y^b$ | None, model/ model comparison | |
| ***Polar Processes*** | | | | |
| Denitrification / dehydration | Comparison of gas-phase $HNO_3$ and $H_2O$ on Eqlat / theta grid | $HNO_3$ and $H_2O$ (gas-phase) [*u,v,T* for Eqlat-$\theta^b$] | Aura-MLS | *Manney et al. (2007); Santee et al. (2007); Lambert et al. (2007)* |
| Chlorine activation | Comparison of HCl on Eqlat / theta grid (loss of HCl is proportional to $Cl_x$ activation) | HCl [*u,v,T* for Eqlat-θ] | Aura-MLS | *Froidevaux et al. (2008)* |

Table 6.1 continued.

| Process | Diagnostic | Variables | Data | References[a] |
|---|---|---|---|---|
| Stratospheric aerosol processes | Abundance of NAT[b] and ICE[b] SAD | SAD-NAT; SAD-ICE | None, model/ model comparison | |
| Chemical ozone depletion | Tracer-tracer chemical ozone loss | $O_3$, $N_2O$, [$u$,$v$,$T$ for Eqlat/θ] | HALOE-UARS | *Rex et al. (2004); Tilmes et al. (2004); Tilmes et al. (2007)* |
| | PACl[b] | $T$, EESC | UKMETO; ERA-40 | *Tilmes et al. (2007)* |

[a] *Listed references only provide examples.*

[b] *Abbreviations: Js=photolysis rate constants (sec$^{-1}$); IPMMI = International Photolysis Frequency Measurement and Modeling Intercomparison campaign; SAD = surface area density; $NO_y$ = total reactive nitrogen; $Cl_y$ = total inorganic; chlorine; $Br_y$ = total inorganic bromine; $TCl_y$ = total chlorine (inorganic + organic); $TBr_y$ (inorganic+organic); $HO_x$ = OH + $HO_2$; $NO_x$ = NO + $NO_2$; NAT = nitric acid trihydrate; ICE = water ice; Eqlat-θ = Equivalent latitude - potential temperature coordinate system; PoLS = polar lower stratosphere; EqUS = equatorial upper stratosphere; ExtrpLS = extratropical lower stratosphere; PACl = potential for chlorine activation.*

is given in Chapter 1.

## 6.3.1 Evaluation of Photolysis Rates

The accurate calculation of photolysis (J) rates is an essential component of any atmospheric chemical model. However, this calculation is complex and there are likely many causes for the differences between models. Models may differ in their treatment of radiative transfer, aerosols and clouds. Models may update the photolysis rates at a different time resolution. Although all CCM photolysis modules use standard absorption cross-sections (*e.g.* , Sander *et al*., 2006, hereafter JPL-2006), they likely differ in how they are implemented in terms of wavelength integration or temperature dependence.

For these reasons it is important to compare photolysis rates calculated by CCMs using a standard set of prescribed conditions (*e.g.*, $O_3$, temperature, and pressure profiles). Modelling groups need to use the code actually employed in the CCM for this comparison, which is based only on the final J-values – the quantity actually relevant for the chemical comparisons – and not on the separate components of the calculation. For example, it is not useful to plot and compare cross-sections since each model has their own algorithm for number of wavelength bins, the method of averaging the cross-sections with solar flux, and how to include temperature dependencies.

### 6.3.1.1 Introduction to PhotoComp

This photolysis benchmark (PhotoComp 2008) is a component of SPARC CCMVal and has been designed to evaluate how models calculate photolysis rates (and indirectly heating rates) in the stratosphere and troposphere. The primary goal is to improve model performance due to better calibration against laboratory and atmospheric measurements, and to provide more accurate numerical algorithms for solving the equation of radiative transfer. As with specific components of any major model comparison (*e.g.*, Prather and Remsberg, 1993), there may be numerous mistakes due to a different interpretation of the experiment, simple mistakes in model coding, different sources of physical data (solar fluxes, cross-sections, quantum yields) or different approximations of the exact solution. Any of these can make a model an "outlier" for one particular test, and thus the analysis must strive to identify these outliers as quickly as possible and provide clues as to the cause. This does not always mean that the majority rules, but in most cases, singularly unusual J-value profiles for a model are in error. The PhotoComp experiments are summarized in **Table 6.2**.

The PhotoComp 2008 participating models and the experiments they submitted are listed in **Table 6.3**. Details of the model photolysis schemes are given in the Supplementary Material in Table 6S-4. A total of 12 models (11 groups) performed at least some of the experiments and these included some stand-alone photolysis codes that have participated in other comparisons with models and measurements. Unfortunately, only 9 of the 18 CCMVal CCMs are represented. The missing CCMs should perform these tests in the future.

For PhotoComp 2008 we do not establish a single model as a reference standard, but instead define a robust mean and standard deviation from the ensemble of contributing models (see **Table 6.4**). The J-values (sec$^{-1}$) are converted to the natural logarithm of the J-value (ln(J)) and averaged. A lower altitude cutoff is made where J < $10^{-10}$ sec$^{-1}$ (or $10^{-14}$ sec$^{-1}$ for J-$O_2$). Models that fall more than

**Table 6.2:** PhotoComp 2008 experiments. The diagnostics which are used as quantitative metrics for the overall model assessment are highlighted in gray.

| Simulation | ALB | SZA | RS | CLD | AER | Figure | Comments |
|---|---|---|---|---|---|---|---|
| ***High Sun*** | | | | | | | |
| P1a | 0.1 | 15° | Y | N | N | 6.1, 6.4 | Clear sky, with Rayleigh scattering |
| P1b | 0.1 | 15° | Y | N | Y | 6.2 | Pinatubo aerosol in stratosphere |
| P1c | 0.1 | 15° | Y | Y | N | 6.3 | Stratus cloud in troposphere |
| ***Low Sun*** | | | | | | | |
| P2a | 0.1 | 84-96° | Y | N | N | 6.4 | 24-hour average |
| P2n | 0.1 | 84° | Y | N | N | 6.4 | Noontime |
| P2m | 0.1 | 96° | Y | N | N | 6.4 | Midnight |
| ***Wavelength Binning*** | | | | | | | |
| P3 | 0.0 | 15° | N | N | N | 6.5 | Beer's Law extinction only, test wavelength binning for J-$O_3$ and J-$NO_2$ |

*Abbreviations: Js=photolysis rate constants ($sec^{-1}$); SZA = solar zenith angle; ALB = surface albedo; RS= Rayleigh scattering; AER = aerosol; CLD = cloud.*

**Table 6.3:** Models contributing to CCMVal PhotoComp 2008. The eight CCMs are indicated in bold.

| Group | Model | Label | P1a | P1b | P1c | P2a | P2n | P2m | P3 | Participants |
|---|---|---|---|---|---|---|---|---|---|---|
| GFDL, USA | **AMTRAC** | AMTR | √ | | | √ | √ | √ | | J. Austin |
| NIES, Japan | **CCSRNIES** | CCSR | √ | √ | | √ | √ | √ | | H. Akiyoshi |
| MPI-C, Ger. | **EMAC** | EMAC | √ | | √ | √ | √ | | | R. Sander, C. Brühl |
| GSFC, USA | FastJX | GFJX | √ | √ | √ | √ | √ | √ | √ | H. Bian |
| GSFC, USA | **GEOSCCM** | Gtbl | √ | | | √ | √ | √ | | R. Kawa, R. Stolarski |
| CNRS, France | **LMDZrepro** (TUV4.1) | LMDZ | √ | √ | √ | √ | √ | √ | √ | S. Lefebvre,S. Bekki |
| NIWA, NZ | **NiwaSOCOL** | NIWA | √ | | √ | √ | √ | √ | | D. Smale, E. Rozanov |
| PMOD-WRC / ETH, CH | SOCOL | SOCOL | √ | | | √ | √ | √ | | E. Rozanov |
| NCAR, USA | TUV | TUVM | √ | √ | √ | √ | √ | √ | √ | S. Madronich |
| UCI, USA | FastJX & UCIref | UCIJ UClr | √ | √ | √ | √ | √ | √ | √ | M. Prather |
| U. Leeds, UK, U. Bremen, Ger. | **UMSLIMCAT** | SLIM | √ | | | √ | √ | √ | | M. Chipperfield, M. Sinnhuber |
| NCAR, USA | **WACCM** | WACC | √ | | | √ | √ | √ | √ | D. Kinnison |

2 standard deviations (in ln(J)) from the mean for levels starting 3 levels above the lowest altitude (step 2) up to ~74 km are dropped, and we recalculate this 'robust' mean ln(J) and standard deviation for the remaining models. The atmospheric average robust standard deviation (RSD) for the 60 J-values are reported in Table 6.4 and the profiles of the model deviations from the robust mean ln(J) for selected J-values are shown in Figures 6.1 and 6.4. This method quickly identified outlying models with obvious mistakes, and it also identifies specific J-values for which there is clearly a large uncertainty, even among the best models.

### 6.3.1.2 PhotoComp 2008 experiments

There were 3 parts to the photolysis comparison which are summarized below. Complete experimental details are

**Table 6.4:** Atmospheric averaged robust standard deviation of ln(J) (x100 = RSD in %), identifying Js and conditions for which there is general agreement among the models. Results are shown for high sun (P1a), polar noontime (P2n) and 24-hour average (P2a).

| No. | J-value | P1a | P2n | P2a | No. | J-value | P1a | P2n | P2a |
|---|---|---|---|---|---|---|---|---|---|
| 1 | NO | 19 | 30 | 34 | 31 | F115 | 15 | 20 | 26 |
| 2 | O2 | 7 | 9 | 10 | 32 | CCl4 | 4 | 5 | 6 |
| 3 | O3 | 18 | 14 | 16 | 33 | CH3Cl | 8 | 5 | 6 |
| 4 | O3 (1D) | 9 | 10 | 13 | 34 | MeCCl3 | 8 | 8 | 12 |
| 5 | H2COa | 12 | 32 | 45 | 35 | CHF2Cl | 24 | 31 | 33 |
| 6 | H2COt | 28 | 53 | 71 | 36 | F123 | 13 | - | 9 |
| 7 | H2O2 | 7 | 6 | 20 | 37 | F141b | 7 | 4 | 5 |
| 8 | CH3OOH | 7 | 10 | 22 | 38 | F142b | 24 | 13 | 13 |
| 9 | NO2 | 7 | 7 | 17 | 39 | CH3Br | 3 | 6 | 8 |
| 10 | NO3 | 7 | 10 | 19 | 40 | H1211 | 5 | 4 | 5 |
| 11 | N2O5 | 13 | 11 | 14 | 41 | H1301 | 3 | 4 | 5 |
| 12 | HNO2 | 3 | 4 | - | 42 | H2402 | 4 | 4 | 4 |
| 13 | HNO3 | 9 | 10 | 16 | 43 | CH2Br2 | 8 | 6 | 10 |
| 14 | HNO4 | 15 | 47 | 63 | 44 | CHBr3 | 8 | 28 | 34 |
| 15 | ClNO3a | 10 | 18 | 26 | 45 | CH3I | - | - | - |
| 16 | ClNO3t | 7 | 17 | 28 | 46 | CF3I | - | - | - |
| 17 | Cl2 | 11 | 9 | 22 | 47 | OCS | - | - | - |
| 18 | HOCl | 5 | 16 | 24 | 48 | PAN | 6 | 9 | 16 |
| 19 | OClO | 8 | 8 | 13 | 49 | CH3NO3 | - | - | - |
| 20 | Cl2O2 | 16 | 15 | 21 | 50 | ActAld | 41 | 45 | 49 |
| 21 | ClO | - | - | - | 51 | MeVK | 5 | - | - |
| 22 | BrO | 3 | 15 | 24 | 52 | MeAcr | 21 | - | - |
| 23 | BrNO3 | 6 | 9 | 15 | 53 | GlyAld | 24 | - | - |
| 24 | HOBr | 7 | 6 | 12 | 54 | MEKeto | - | - | - |
| 25 | BrCl | 10 | 6 | 15 | 55 | EAld | - | - | - |
| 26 | N2O | 3 | 5 | 13 | 56 | MGlyxl | 21 | 25 | 38 |
| 27 | CFCl3 | 4 | 4 | 10 | 57 | Glyxla | 74 | - | - |
| 28 | CF2Cl2 9 | 10 | 14 | 58 | 58 | Glyxlt | 39 | - | - |
| 29 | F113 | 10 | 8 | 9 | 59 | Acet-a | 12 | 35 | 36 |
| 30 | F114 | 5 | - | 6 | 60 | Acet-t | 11 | 34 | 36 |

available in the Supplementary Material for Chapter 6.

Part 1 is a basic test of all J-values for high sun (SZA = 15°) over the ocean (albedo = 0.10, Lambertian). Part 1a: Clear sky (only Rayleigh scattering) and no aerosols. Part 1b: Pinatubo aerosol in the stratosphere. Part 1c: Stratus cloud in the troposphere. The primary atmosphere was specified in terms of pressure layers, mean temperature, and column $O_3$ in each layer. Absorption by $NO_2$ or other species was not included in calculating optical depths.

Part 2 tests the simulation of a spherical atmosphere and twilight conditions that are critical to the polar regions. It used the same atmosphere as Part 1 without clouds or aerosols and assumed equinox (solar declination = 0°) and latitude of 84°N. The surface SZA (not including refraction) therefore varies from 84º (noon) to 96° (midnight). J-values were reported at noon, midnight, and the 24-hour average (integrating as done in the CCM).

Part 3 tests the accuracy of wavelength binning in the critical region 290-400 nm that dominates tropospheric photolysis. Rayleigh scattering and surface reflection were

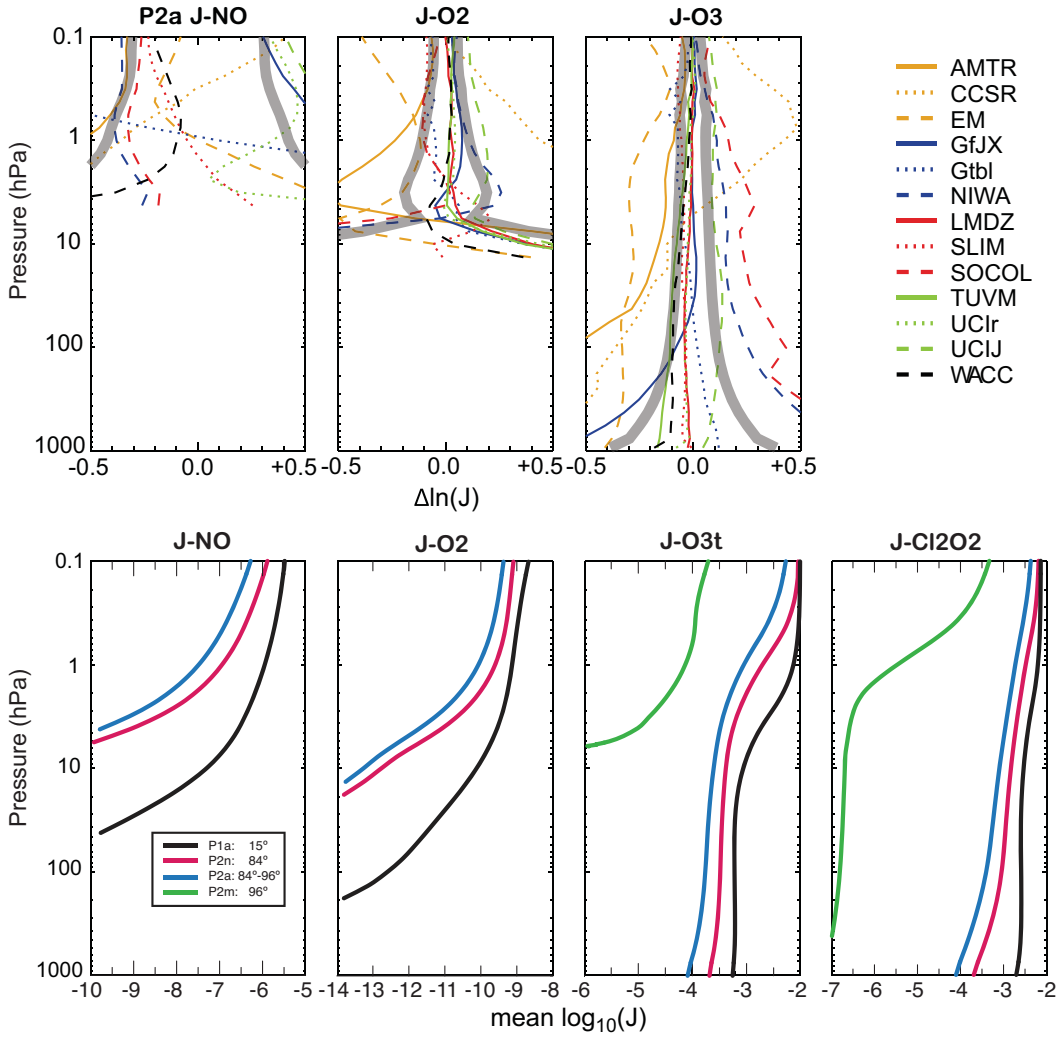


**Figure 6.1:** Model deviations in ln(J) ($sec^{-1}$) from the robust mean for nine selected J-values (NO, $O_2$, $O_3$, $O_3(^1D)$, $NO_2$, $H_2COa$, $CFCl_3$, $CF_2Cl_2$, $N_2O$) from PhotoComp experiment P1a (clear sky, SZA = 15°). The robust mean and standard deviation are derived as follows: (1) calculate the mean ln(J) from all contributing models; (2) drop all lower altitudes where mean J < $1x10^{-10}$ (or <$1x10^{-14}$ for J-$O_2$); (3) drop any model outside two standard deviations for levels starting 3 levels above the lowest altitude (step 2) up to ~74 km; (4) recalculate this robust mean ln(J) and standard deviation for the remaining models. The ±1 standard deviations are plotted as wide gray bands.

switched off (albedo = 0) giving effectively a simple Beer's Law calculation. The calculation repeated Part 1, but report only J-values for J-$O_3$ (*i.e.*, total), J-$O_3(^1D)$ [$O_3 \rightarrow O_2 + O(^1D)$], and J-$NO_2$ [$NO_2 \rightarrow NO + O$]. These are the two critical J-values for the troposphere, and they both have unusual structures in absorption cross-section and quantum yields. Reference runs were done using very high resolution (< 0.1 nm) cross-sections and solar fluxes and for different options (*e.g.*, JPL-2006 *vs.* IUPAC cross-sections) to provide a benchmark. Results for Part 3 focus on J-values below 24 km.

A standard atmosphere was specified, whose primary definition is in terms of the air mass (pressure thickness), ozone mass, and mean temperature in each layer. This chosen atmosphere is typical of the tropics with total ozone column of 260 DU. The use of JPL-2006 data (same as main CCM runs) was encouraged. High-resolution solar fluxes as a reference (sun-earth distance = 1.0 astronomical unit, averaged over the 11-year solar cycle) were also provided.

### 6.3.1.3 PhotoComp 2008 results and discussion

**Figure 6.1** shows the deviations in ln(J) from the robust mean for nine selected J-values from experiment P1a. The agreement among the core models (those within 2

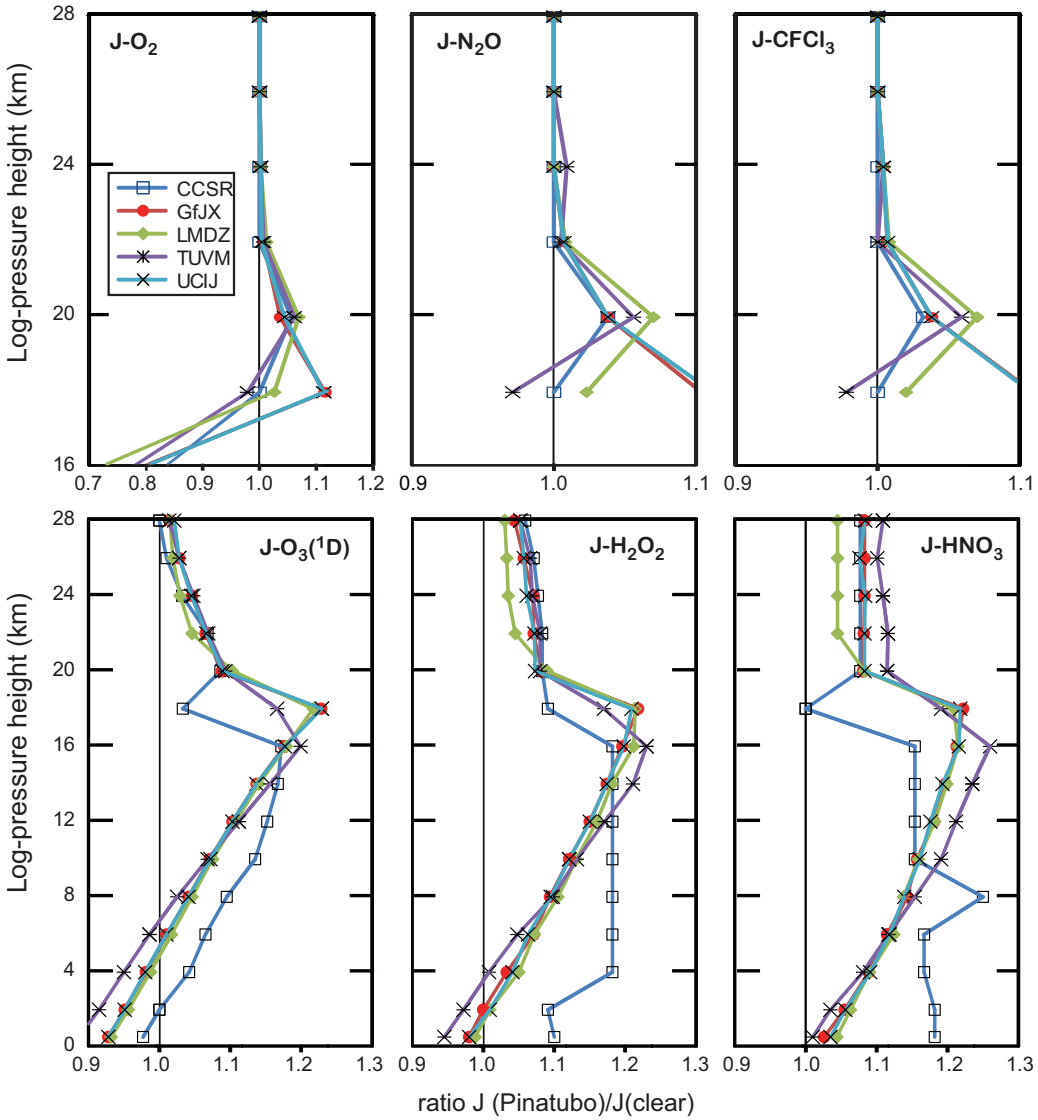


**Figure 6.2:** Ratio of J-values for a Pinatubo-like stratospheric aerosol layer (P1b: 17-19 km, optical depth 1.0 at 600 nm) to those for clear sky vs. pressure altitude (km). Five models contributed results and selected J-values are shown ($O_2$, $N_2O$, $CFCl_3$, $O_3(^1D)$, $H_2O_2$, $HNO_3$) for altitudes of relevance to atmospheric chemistry.

standard deviations) is really excellent for many J-values. Some models consistently fall outside this core and it appears to be due to the method of solving the radiative transfer equation (*e.g.*, look-up tables). The robust standard deviation in J-NO is less than 20% above 1 hPa, but for the region 1-10 hPa where most of the $NO_y$ is destroyed by J-NO, the models diverge with the fast-JX based models being almost a factor of 2 larger than the others. This discrepancy may reflect the failure of some models (*e.g.*, UCI) to account for NO self-absorption above 0.1 hPa, or else the very different treatments of the Schumann-Runge bands.

For $N_2O$ and $CFCl_3$, the robust standard deviation is very small. Surprisingly, it is much larger for $CF_2Cl_2$ which photolyses in the same wavelength region, and possibly the cross-sections for $CF_2Cl_2$ are effectively different in several models. Other oddities stand out, *e.g.*, the relatively large ±15% range in J-$H_2CO$a (a = radical-radical product channel, H + HCO). Another feature is the generally worse agreement between J-$O_3$ and J-$O_3(^1D)$ within the troposphere compared with the stratosphere, and is probably caused by inadequate treatment of Rayleigh scattering. In general, most J-values that fall outside the ±2 standard deviation test show unusual structures with altitude, implying errors in the radiative transfer solution rather than the cross-sections.

**Table 6.4** summarizes the RSD of the model J-values averaged over altitudes of interest for case studies P1a, P2n and P2a (see table text). For many J-values we find exceedingly good agreement (10% or less), but there are surpris-

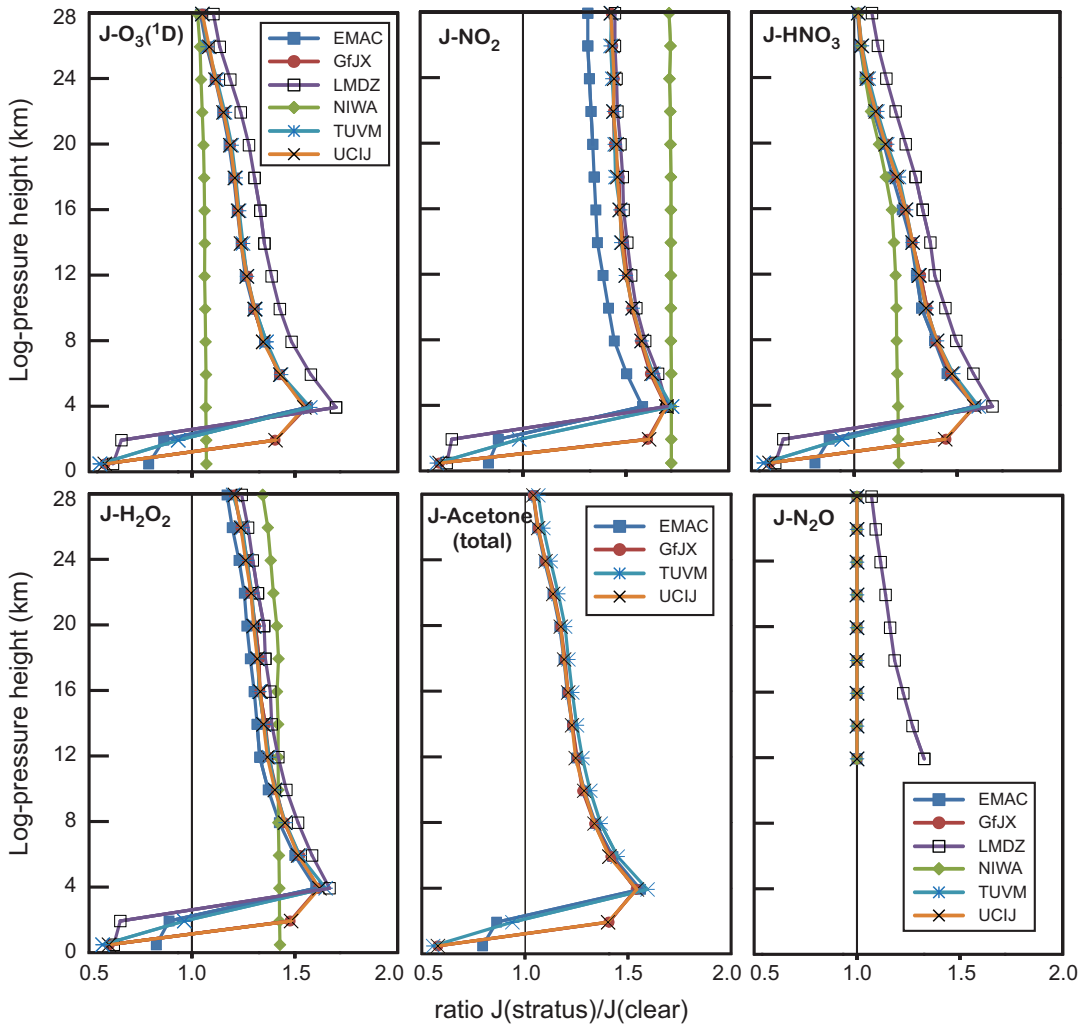


**Figure 6.3:** Ratio of J-values for a stratus cloud layer (P1c: 1-3 km, optical depth 20.0 at 600 nm) to those for clear sky vs. pressure altitude (km). Six models contributed results and selected J-values are shown ($O_3(^1D)$, $NO_2$, $HNO_3$, $H_2O_2$, acetone (total, only 4 models), $N_2O$).

ingly large RSDs for J-$O_3$ (t = sum of all product channels), J-$H_2CO$ (a and t), J-$HNO_4$, J-$Cl_2O_2$, a couple fluorocarbons, and many of the volatile organic compounds (VOCs) (few contributing models). For J-$HNO_4$ the near-IR photolysis may not be included (Evans *et al*., 2003). J-$O_3$ is a key heating rate term: Three models show aberrant profiles at high sun (see Figure 6.1), but six models are obviously outside the RSD for polar conditions (see **Figure 6.4).** These discrepancies are worrisome and may impact the model circulations. However, note that in most cases CCM photolysis schemes are not linked to heating rate calculations.

The RSD is a single iteration that identifies and removes models more the ±2 standard deviations from the mean of ln(J). This method was chosen to avoid having extreme outliers influence the mean. The process can be iterated again and again to remove those outside the new smaller standard deviation range. For example, if we focus on J-$O_2$, the initial RSD over the stratospheric range of interest (18-70 km) is 7.1% with AMTR and CCSR and Gtbl removed. A second iteration removes EMAC, NiwaSOCOL, UMSLIMCAT and SOCOL, and cuts the standard deviation to 3.2%. Thus, a core group (GfJX, LMDZrepro, TUVM, UCIr, UCIJ, WACCM) shows remarkable agreement in the calculation of J-$O_2$. Similarly for J-$O_3(^1D)$, if we focus on the stratosphere and mesosphere (12-74 km), then the first iteration drops CCSR and Gtbl, resulting in an RSD of 7.6%. The next iteration drops NiwaSOCOL and SOCOL, reducing the standard deviation to 4.0%; and a further iteration drops AMTRAC, leaving a core group (EMAC, Gfjx, LMDZrepro, TUVM, UCIJ, WACCM, UMSLIMCAT) with a standard deviation of only 2.8%.

**Figure 6.2** shows the change in J-values for a Pinatubo-like aerosol layer (P1b). The enhanced aerosol scattering of the Mt. Pinatubo layer was predicted to alter the photolysis rates in the stratosphere and troposphere

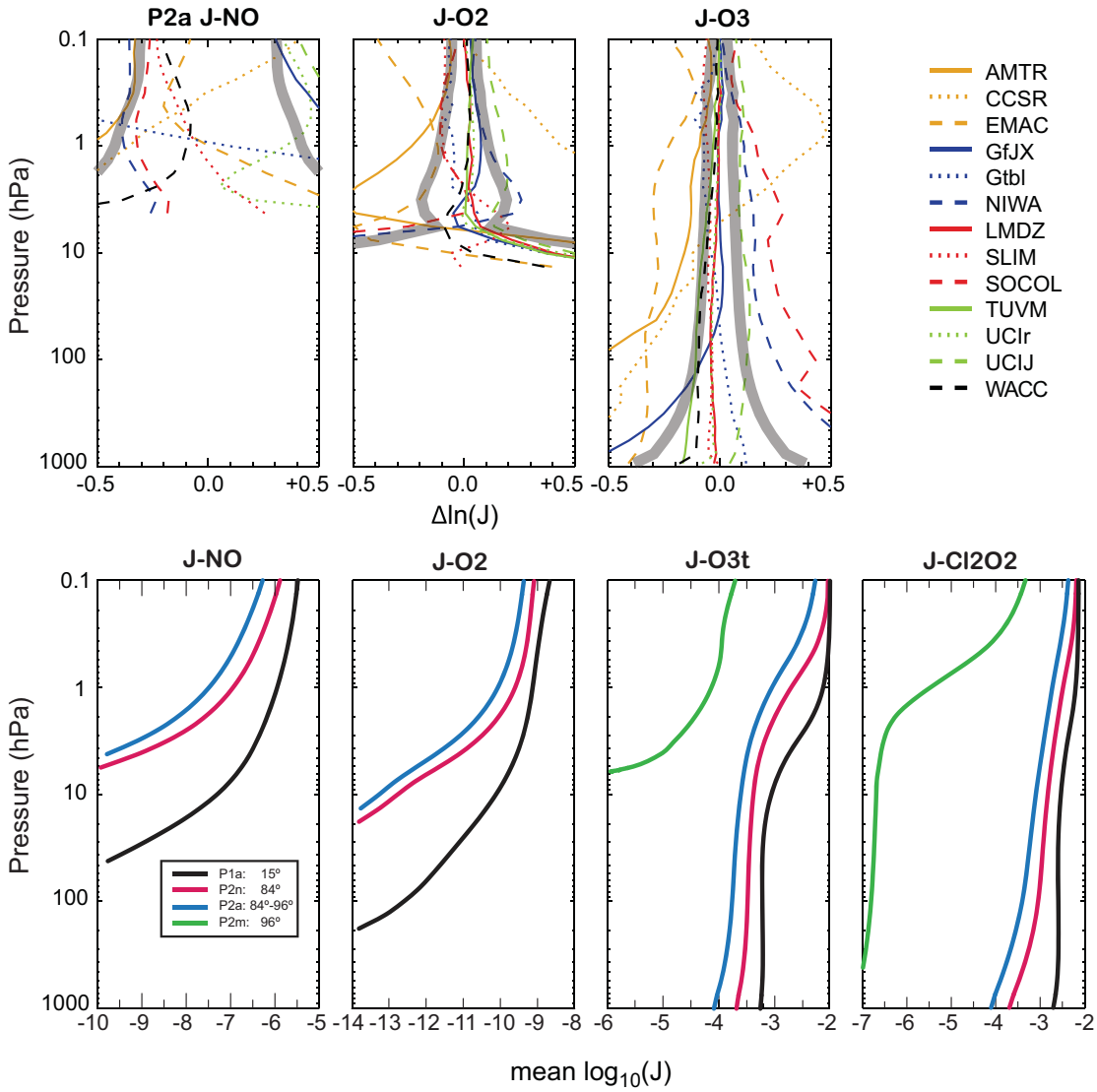


**Figure 6.4:** (top) Model deviations in ln(J) ($sec^{-1}$) from the robust mean for three selected J-values (NO, $O_2$, $O_3$(total) from PhotoComp experiment P2a (24-hour average, polar, SZA = 84°-96°). (bottom) The robust mean ln(J) ($sec^{-1}$) for J-NO, J-$O_2$ and J-$O_3$(total) and J-$Cl_2O_2$ for experiments P1a, P2n, P2a, and P2m.

(Michelangeli *et al.*, 1989). Five models (only two of which are CCMVal models) submitted results. All models agree on the 4-7% increase at short wavelengths (~205 nm, J-$O_2$, J-$N_2O$, J-$CFCl_3$) in the layer immediately above the aerosols (20 km), but there is a large disparity in the middle of the aerosol layer at 18 km. UCIJ and GfJX (both based on fast-JX codes) predict a further increase to 11% above clear sky, whereas CCSRNIES, LMDZrepro, and TUVM predict a decrease in the ratio. Given the optical depth of 0.5 at mid-layer, one would expect that the J-values relative to clear sky would continue to increase in the aerosol layer, but this discrepancy may reflect the different ways of implementing a scattering layer relative to the CTM layers. Some models may have reported mid-aerosol-layer J-values; and others, the bottom of aerosol-layer (similar analysis applies to the stratus cloud layer (Figure 6.3). For J-values of interest throughout the atmosphere (*e.g.*, J-$O_3$($^1$D), J-$H_2O_2$, J-$HNO_3$) the models are in reasonable agreement, showing up to 20% enhancements through most of the troposphere, except for CCSRNIES for which there may be a mistake in submission as the pattern of change in the troposphere is inexplicable. The offset of TUVM below the cloud from the GfJX-LMDZ-UCIJ curves is probably due to differences in aerosol layer placement, but needs to be clarified.

**Figure 6.3** is similar to Figure 6.2 but for a thick stratus cloud (P1c). The enhanced scattering above a thick stratus cloud layer increases photolysis rates above and reduces them at the surface. Six models submitted results, and five models have the correct pattern. Once again, as in

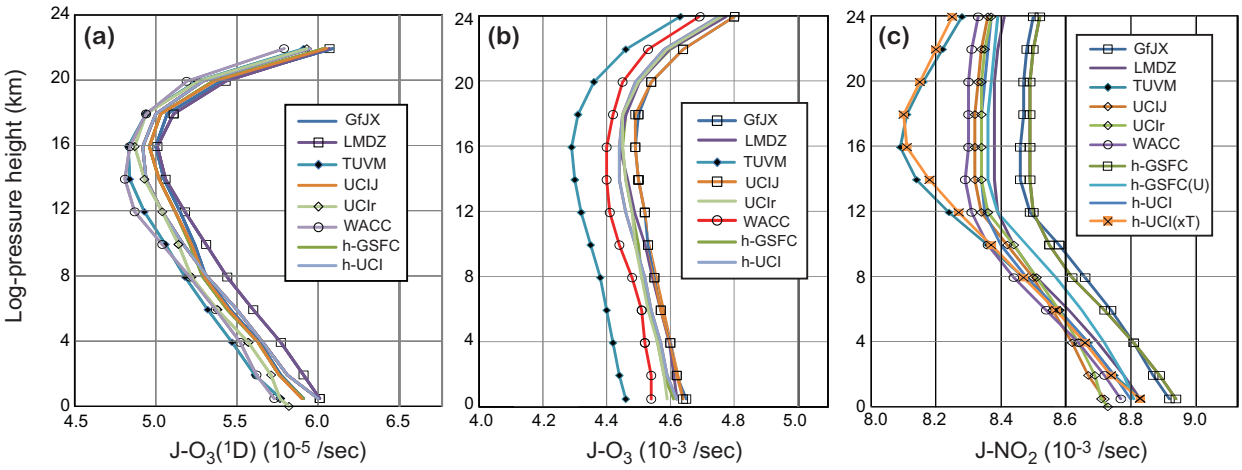


**Figure 6.5:** J-values (sec$^{-1}$) vs. pressure altitude (km) for (a) $O_3$ yielding $O(^1D)$, (b) $O_3$ total, and (c) $NO_2$ from the Photocomp P3 experiment (SZA = 15°, no Rayleigh scattering, no surface albedo, see text). In addition to the standard coarse wavelength resolution models already described, Bian (GfJX) and Prather (UCIr, UCIJ) contributed very-high wavelength resolution (~0.1 nm) calculations (h-GSFC and h-UCI) using the same cross-section, quantum yield and solar data as in their coarse models. For J-$NO_2$, the h-GSFC(U) also contributed a high-resolution J using the UCI tables for cross-section and quantum yield, and the h-UCI(xT) also included a log-extrapolation of both tables below their lower temperature limits.

P1b, the placement of cloud in the second layer appears to differ with UCIJ-GfJX having 50% enhancements in the middle of the CTM layer, but TUVM-LMDZrepro-EMAC having reductions, possibly representing the bottom of the cloud. All five of these models have large (20% to 40%) reductions in the lowest layer, below the cloud. NiwaSOCOL apparently has a very simple and inaccurate parameterisation of clouds. LMDZrepro reproduces the expected tropospheric patterns, but calculates large, incorrect enhancements in the 205 nm wavelength region, thus predicting enhanced photolysis of species such as $O_2$, $N_2O$, and $CFCl_3$ above clouds.

**Figure 6.4** shows (*bottom*) the robust mean ln(J) for J-NO, J-$O_2$, J-$O_3$(t) and J-$Cl_2O_2$ for experiments P1a and P2 (n, a, m), and (*top*) the deviations from the mean for the 24-hour polar average rates P2a for J-NO, J-$O_2$, J-$O_3$(t). As expected, averaging over polar twilight conditions increases the spread in the models as compared with high sun (P1a).

**Figure 6.5** shows results from the high-wavelength-resolution experiment P3 (SZA=15°, no Rayleigh scattering, no surface albedo, see figure caption). Six models contributed results from their standard models and two (h-GSFC, h-UCI) also contributed high-resolution wavelength integrations of the J-values. These two high-resolution models also included an additional high-resolution calculation for J-$NO_2$ that explored different approaches to using the $NO_2$ cross-sections and quantum yields (see figure caption). The calculation of J-$O_3$($^1$D) from the ten different submissions is in good agreement, with a min-max range of ±4%. An estimate of the error in adopting the coarser wavelength resolution of UCIJ's fast-JX (7 nm) instead of the UCIr's J-ref code (1 to 2 nm bins over 295-324 nm) is seen to be small (2%) and is consistent with the very high resolution of h-UCI (0.05 nm bins) using the same solar flux and physics. Thus we conclude that 5 groups agree on the calculation of J-$O_3$($^1$D) within 5% and that the various wavelength resolutions and quadratures have small errors

The J-$O_3$(t) values, with the exception of TUVM are much tighter, with a ±2.5% min-to-max range. The TUVM values are surprisingly about 3% below the mean of models and may reflect a difference in the Chappuis-band photolysis (> 400 nm).

The J-$NO_2$ values are in excellent agreement with a core group of models having a ±1% min-max range. The two Goddard models (GfJX and h-GSFC) are inexplicably, uniformly greater by almost 3%. In the upper troposphere and lower stratosphere at temperatures below 240 K there is ambiguity in how to calculate $NO_2$ photolysis given the recommended tables for cross-sections (220 K and 294 K) and quantum yields (248 K and 298 K). The UCI models (UCIJ, UCIr, h-UCI) interpolate linearly with temperature between the two tabulated values and do not extrapolate; whereas the h-UCI(xT) model (and apparently the TUVM model) extrapolates the log of both values to temperatures beyond the table range. This modest extrapolation is probably valid and thus there is a bias error in most standard models for J-$NO_2$ in the upper troposphere/lower stratosphere (UTLS) of about +3%.

Overall, the agreement among the participating models in experiment P3 (Figure 6.5) is excellent. Even the potential biases identified are below 3%. In terms of grading,

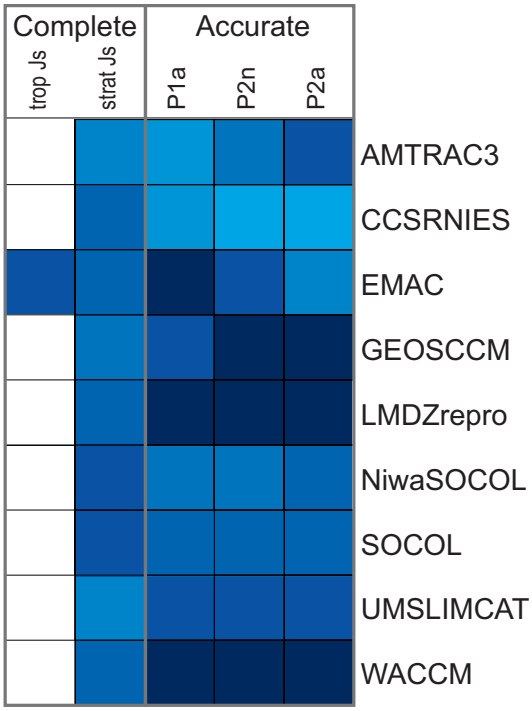


**Figure 6.6:** Matrices displaying PhotoComp grades for the nine participating CCMs. Two grades were given for the completeness of reported J-values relevant to the stratosphere (~45 out of 60) and the troposphere (~15, mostly VOCs). Accuracy for the J-values was based on the number of Js (out of the 45 stratospherically relevant ones) that were not eliminated by the initial ±2 standard deviation test for P1a, P2n, and P2a. The stand-alone photolysis codes (GfJX, TUVM, UCIJ, UCIr) all received grades of 0.9 to 1.0 in all tests.

we could give all the participating models a good score for this part, but more importantly, this experiment shows that calculation of J-values using coarse resolution - providing the wavelength averaging is done correctly (see Wild *et al*., 2000) - does not induce errors above 2%.

**Models and Measurements.** An earlier version of TUVM participated in the International Photolysis Frequency Measurement and Modeling Intercomparison (IPMMI; Cantrell *et al*., (2003); Hofzumahaus *et al*., (2004)) and performed excellently in calculating the clear-sky J-$NO_2$, J-$O_3$(total), and J-$O_3(^1D)$ at the ground over the full range of SZA during the day. Thus TUVM provides a transfer standard for the P3 experiments (at least near the surface) and indicates that those participating models do match measured tropospheric J-values. Several campaigns measured J-values in the lower stratosphere (*e.g*., POLARIS, and SOLVE) and it may be possible in the future to find a suitable transfer standard, such as the APL model, for these measurements.

### 6.3.1.4 PhotoComp 2008 grading

One major issue of model comparison is to grade models objectively. For photolysis we consider both the completeness of the reported J-values and the accuracy compared with the robust mean. While it is possible to calculate the abundance of stratospheric ozone *without* all the requested J-values, their inclusion in the CCM allows for that species to be simulated and evaluated against observations. Thus we include completeness of J-values relevant to stratosphere and troposphere separately. For accuracy, we consider only the 45 J-values with stratospheric relevance and the grades (in %) represent roughly the fraction of J-values that passed the RSD test. These grades are slightly generous for models that did not report all 45 J-values as only the reported outlying J-values were counted as inaccurate. Grades for the stand-alone (non-CCM) models were all in the 0.9 – 1.0 (90-100%) range.

The reporting CCMs showed a wide range of skill in calculating Js (**Figure 6.6**). EMAC, GESOCCM, LMDZRepro, UMSLIMCAT and WACCM were consistently in the 0.9 – 1.0 (90-100%) range. EMAC was unusual in having trouble with the 24-hour average polar Js, and given the rest of its performance, this looks like a mistake in averaging for the PhotoComp reporting. NiwaSOCOL and SOCOL have some occasional problems that could be either the radiative transfer solutions or cross-sections. AMTRAC and CCSRNIES appear to have serious flaws in the radiative transfer solution with large errors in key J-values. Unfortunately, we have no information on the other nine CCMs. If the lack of participation was due to the difficulty of running PhotoComp experiments with the CCM J-value code, then this is worrisome as it points to the lack of ability to test the components of the CCMs or have a traceability to independent codes. Overall, given the good comparison of many CCMs with the detailed benchmark codes, we can conclude that it is possible to incorporate an accurate but computationally efficient photolysis scheme in a global CCM.

## 6.3.2 Evaluation of Radical (Fast) Chemistry (Non Polar Region)

The fast photochemistry within the CCMs has been evaluated by comparison of radical species in the $O_x$, $HO_x$, $NO_x$, $ClO_x$, and $BrO_x$ families to results from a photochemical steady state (PSS) box model, constrained by values of radical precursors specific to each CCM. In the past the PSS box model has been compared exhaustively to observed abundances of radicals and radical precursors (*e.g*., Salawitch *et al*., 1994a,b, 2002; Wennberg *et al*., 1994, 1998; Osterman *et al*., 1997, 1999; Sen *et al*., 1998, 1999; Jucks *et al*., 1998, 1999, Christensen *et al*., 2002; Kovalenko *et al*., 2007). The approach described below has

been used previously in the evaluation of 2D and 3D models sponsored by the NASA Models and Measurements Intercomparison II (NASA/TM-1999-209554).

### 6.3.2.1 Background to photochemical steady state model comparisons

We computed zonal, monthly mean values of the radical precursors $O_3$, $H_2O$, $CH_4$, CO, $NO_y$, $Cl_y$, and $Br_y$ (hereafter precursors) as a function of pressure and radicals ($O(^3P)$, $O(^1D)$, OH, $HO_2$, $NO_x/NO_y$, $ClO/Cl_y$, and $BrO/Br_y$) from the REF-B1 T3I files. Zonal, monthly mean profiles of T, $N_2O$ and sulfate surface area density (SAD) were also found. The profiles of T, $O_3$, $H_2O$, $CH_4$, CO, $NO_y$, $Cl_y$, $Br_y$, and sulfate SAD were input to the PSS box model. The model is used to compute the diel variation of $O(^3P)$, $O(^1D)$, OH, $HO_2$, $NO_x$, ClO, and BrO on a 15 minute time grid using an implicit integration scheme that converges to steady state (production and loss of each chemical species = 0 when integrated over a 24 hr period) using a Newton-Raphson solver. If the CCM model has used the same chemical mechanism (reaction scheme, rate constants, and absorption cross-sections) as the PSS model, then 24-hour average profiles of radicals found from the PSS simulation should closely approximate the zonal monthly mean profiles of radicals from the CCM. A close level of agreement should occur because the T3I files upon which the zonal monthly mean CCM profiles are based provide an instantaneous snapshot for a specific value of GMT at all longitudes. There are possible non-linearities in the chemistry due to zonal asymmetry. We provide a quantitative evaluation of the impact of these non-linearities on the comparisons by calculating the standard deviation, about the zonal monthly mean, of temperature and radical precursor abundances. The PSS model is re-run, varying each of the quantities, with the results factoring into the uncertainty calculation. In this manner, we provide a first-order estimate of the impact of these non-linearities on the fast chemistry.

We have chosen to analyse time periods for which observations of precursors and radicals are available from balloon and aircraft campaigns. We compare zonal, monthly mean profiles of radical precursors from each CCM to measured values to assess how accurately these fields are simulated. Rather than compare CCM profiles of radicals to measured radicals, we instead compare to profiles of radicals from the PSS model, which are calculated in the same manner using precursor fields from each CCM. It has been established that the PSS box model provides a reasonably accurate description of measured OH, $HO_2$, NO, $NO_2$, and BrO (*e.g.*, Salawitch *et al.*, 1994a,b, 2002, 2005; Wennberg *et al.*, 1994, 1998; Osterman *et al.*, 1997, 1999; Sen *et al.*, 1998, 1999; Jucks *et al.*, 1998, 1999, Christensen *et al.*, 2002; Pundt *et al.*, 2002; Kovalenko *et al.*, 2007). Therefore, our presumption is that a CCM provides a reasonable representation of fast photochemical processes if:

- the CCM specifies the abundance of radical precursors reasonably well compared to observations and;
- the CCM calculates the abundance of radicals species in a manner that agrees reasonably well with the output of the PSS box model, when the PSS model is constrained to precursor profiles from the CCM.

Unfortunately, we lack observations of $O(^3P)$ and $O(^1D)$. For these species, the PSS box model is used to place the CCM output on a common scale; models that compare well to the PSS output can be inferred to have similar representations of the chemical processes that control these $O_x$ species, whereas models that differ significantly from the PSS output can be inferred to have a representation of $O_x$ chemistry that differs from the other CCMs. It would be difficult to reach such a meaningful conclusion based on comparisons of profiles of $O(^3P)$ and/or $O(^1D)$ from individual CCMs, due to the non-linear dependence of $O_x$ on local $O_3$ and density as well as overhead $O_3$ and pressure.

For the results shown in this chapter, we focus on comparisons for two time periods. The first is for volcanically perturbed conditions at northern hemisphere (NH) mid-latitudes; the second is for moderate aerosol loading conditions in the subtropical NH. Observations during the first time period in the analysis were obtained by the JPL Fourier Transform InfraRed (FTIR) Interferometer (***http://mark4sun.jpl.nasa.gov/***), which flew on the NASA Observations of the Middle Stratosphere (OMS) balloon payload launched from Ft. Sumner, New Mexico (35°N, 104°W) on September 25 and 26, 1993 (*e.g.*, Osterman *et al.* 1997; Sen *et al.*, 1998; Jucks *et al.*, 1998; Salawitch *et al.*, 2002). Observations during the second time period were obtained by instruments on board the NASA ER-2 aircraft, on a flight based out of Barbers Point, Hawaii (21°N, 158°W) during the STRAT campaign (***http://www.espo.nasa.gov/strat/status/summary_jan96.html***) on February 21, 1996 (*e.g.*, Lanzendorf *et al.*, 2001; Weinstock *et al.*, 2001; Dessler, 2002).

There are two other important details of the PSS comparisons that require explanation. One involves chemical kinetics; the other involves sulfate SAD. The PSS model is well suited to mimic the chemical kinetics used by each CCM group (Table 6S.2). For the 2 CCM groups (EMAC and GEOSCCM) that used kinetics parameters from JPL-2002 (Sander *et al.*, 2003) in the REF-B1 simulation, we conducted the PSS comparison using JPL-2002 kinetics. For the other 12 CCMs, JPL-2006 (Sander *et al.*, 2006) kinetics were used both in the REF-B1 simulation and the PSS evaluation. Of these 12 groups, only 3 CCMs (LMDZrepro, UMSLIMCAT, and WACCM) included the chemical reaction $BrONO_2$+O, new for JPL-2006, within

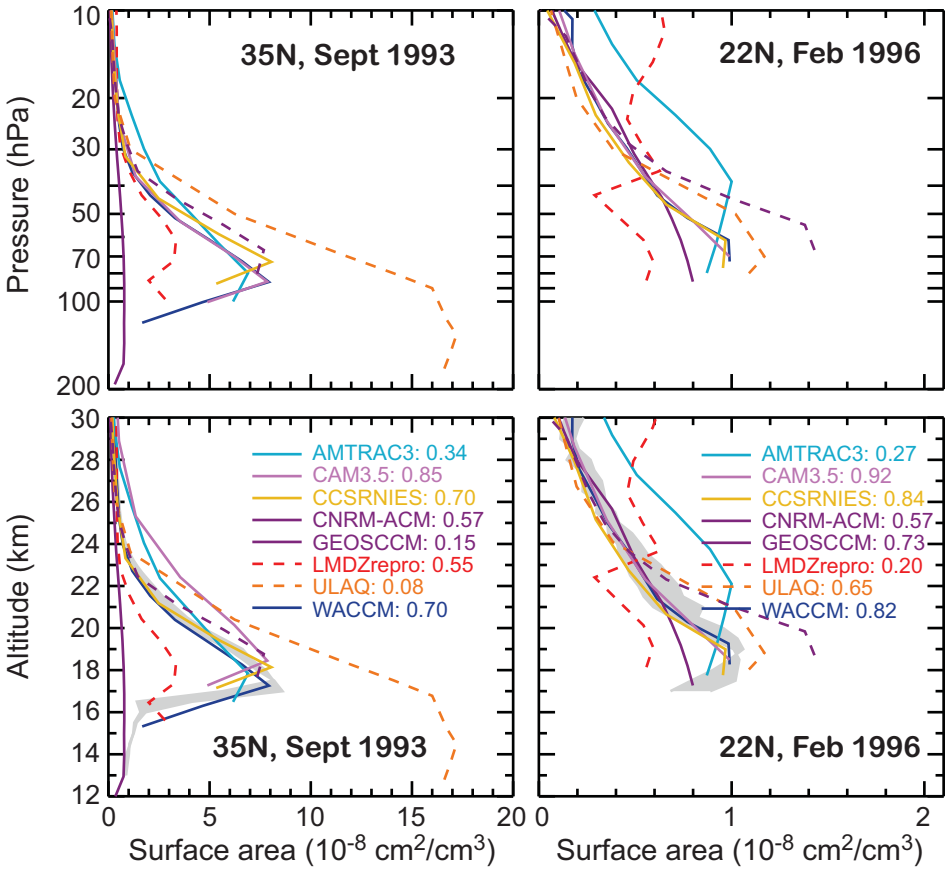


**Figure 6.7:** Sulfate surface area density versus pressure (top two panels) and versus geometric altitude (bottom two panels) for 35°N, September 1993 (left) and 22°N, February 1996 (right) from eight CCMs. The grey shaded region on the bottom two panels shows the climatology for sulfate surface area specified for the REF-B1 simulation (grey bounds values for 32.5° to 37.5°N for September 1993 and for 17.5° to 27.5°N for February 1996). The GEOSCCM REF-B1 calculation was carried out for background sulfate aerosol conditions. The variability among the other models reflects differences with respect to the prescribed climatology that occur for reasons either related to a difficulty in using a prescribed value of surface area given as a function of geometric altitude, or some other unknown cause.

their model. The other 9 CCM teams that used JPL-2006 kinetics neglected this reaction. Inclusion of this reaction increases the BrO/$Br_y$ ratio (Sinnhuber *et al.*, 2002) and has an important effect on the evaluation of CCM chemistry. Indeed, in preliminary versions of this exercise, we provided our own "assessment" of which CCM teams had overlooked this reaction in their implementation of JPL-2006 kinetics that proved to be remarkably accurate. Finally, one group, MRI, neglected the production of HCl by the reaction ClO+OH. Neglect of this product channel, which has been well quantified in the laboratory (Lipson *et al.*, 1999), results in an overestimate of model ClO (McElroy and Salawitch, 1989) and an overestimate of the impact of halogens on future levels of upper stratospheric ozone (Müller and Salawitch, 1999). For the ClO evaluation of the MRI model, the PSS model was run with and without this product channel.

The other detail requiring explanation is sulfate SAD. For the REF-B1 simulation, each CCM group was supposed to use specified values of sulfate SAD, as a function of altitude and latitude, based on the climatology reported by Thomason *et al.* (1997) (updated to near present times). Six CCM teams submitted T3I files for sulfate SAD to the archive. One model team, GEOSCCM, provided their value of sulfate SAD *via* private communication. Another team, AMTRAC, submitted time slices of sulfate SAD for the two evaluation periods. **Figure 6.7** shows profiles of sulphate SAD from these 8 CCMs, as a function of altitude and pressure, for the two fast chemistry evaluation periods. The profiles exhibit tremendous differences. The top panels of Figure 6.7 compare sulphate SAD versus pressure. The bottom panels compare sulfate SAD versus geometric altitude; on these plots, the climatological values of sulfate SAD are shown by the grey shaded region. For September 1993, the grey shaded region corresponds to the Thomason *et al.* (1997) climatology at 32.5°N and 37.5°N;

for February 1996, the grey region corresponds to the climatology at 17.5°N and 27.5°N. To show the results from the CCM models as a function of altitude, we integrated the hypsometric equation starting at the surface, using the zonal monthly mean CCM values of *T versus* pressure (none of the models archived altitude information). The bottom panel indicates values of *g* for each model, found using Equation 6.1 with $n = 3$, where $\sigma_{obs}$ was based on either the width of the grey shaded region at a particular altitude or 10% of the climatological value of sulfate SAD, whichever is largest. The vertical lines in all panels extend to the tropopause.

The values of sulfate SAD archived by the various CCMs exhibit tremendous variability, despite the aim that the REF-B1 be conducted using the same prescribed aerosol climatology in all models. The lowest value of sulfate SAD was used by GEOSCCM, which ran REF-B1 for background (non-volcanic) aerosol conditions. The other 7 CCMs display large differences in SAD for both altitude and pressure coordinates. With the exception of AMTRAC, which provided profiles of sulfate SAD for only a few specified time slices, we have examined time series of sulfate SAD at various altitudes to confirm that we properly interpreted the time coordinate of each model. Results are shown in Figure 6S.1 of the Supplementary Material. All of the models show a peak in sulfate SAD at about the time that aerosol from the eruption of Mt. Pinatubo reached the stratosphere. However, two of the models (LMDZrepro and ULAQ) have archived values of sulfate SAD that are quite different from the prescribed climatology. Furthermore, 6 CCM groups (CMAM, EMAC, MRI, SOCOL, UMSLIMCAT, and UMUKCA-METO) submitted enough T3I files from the REF-B1 for the fast chemistry to be evaluated, but neglected to archive sulfate SAD. The goal of the REF-B1 simulation was for each model to simulate, as closely as possible, the sensitivity of ozone to halogens and volcanic aerosol during the past half century. The large difference between the archived values of sulfate SAD and the climatology suggests this goal has not been achieved. One difficulty in achieving this goal may be that the aerosol climatology was specified as a function of geometric altitude, a coordinate not native to most CCMs.

The profile of sulfate SAD has a profound impact on the abundance of $NO_x$, $HO_x$, and $ClO/Cl_y$ in the lowermost stratosphere. We chose September 1993 as a first case for examination due to the perturbation to the chemical radicals by the Pinatubo aerosol. Provided each model archives the actual profiles of sulfate SAD used in their REF-B1 run, the fact that there is so much model to model variability is not central to our evaluation of the CCM fast chemistry. For the 6 CCM groups that did not archive sulfate SAD, we have estimated this quantity by calculating a value of geometric altitude at each CCM pressure level and interpolating the sulfate SAD climatology for the precise CCM latitude. We associated the uncertainty in these values of sulfate SAD based on a ±0.2 km uncertainty in the altitude and a 5° uncertainty in the latitude used in the interpolation. In the grading table that summarizes the results of the fast chemistry evaluation, we include an asterisk within the "total grade" cell for the 6 CCMs that did not archive sulfate SAD, reflecting the importance of this parameter to the fast chemistry evaluation.

### 6.3.2.2 Photochemical steady state model results

**Figure 6.8** compares the zonal monthly mean profile of radical precursor from 14 CCMs, for September 1993 and the closest model latitude to 35°N, to the profile of $N_2O$ measured by the balloon-borne MkIV instrument on 25 Sept 1993 at 35°N. Comparisons are also conducted for correlations of $O_3$ *vs.* $N_2O$, $H_2O + 2CH_4$ ($H_{tot}$) *vs.* $N_2O$, $NO_y$ *vs.* $N_2O$, where all observed values of all quantities are based on MkIV measurements. Comparisons are made for $Cl_y$ *vs.* $N_2O$ and $Br_y$ *vs.* $N_2O$ as well. Here, the estimates of $Cl_y$ and $Br_y$ are based on the Woodbridge *et al.* (1995) and Wamsley *et al.* (1998) relations, respectively. These relations were derived from aircraft observations that sampled stratospheric air masses, and have been scaled to mid-latitude conditions appropriate for September 1993 using well known time variations of organic halocarbons (*e.g.*, Table 8-5, WMO 2007). The $Br_y$ relation was scaled to remove the influence of $CH_2Br_2$, a species known to provide ~2.2 ppt to the stratosphere (Wamsley *et al.*, 1998) that was not prescribed in the REF-B1 simulation.

For a quantitative evaluation of the radical precursor fields within the CCMs, we used Equation 6.1 with $n$=3 to find $g_{precursor}$ for each model (numerical values given on Figure 6.8). Here, $\mu_{CCM}$ is the zonal-mean value from each CCM, $\mu_{obs}$ is the precursor value from either MkIV or the $Cl_y$ (Woodbridge) or $Br_y$ (Wamsley) relation, and $\sigma=\sqrt{(\sigma_{CCM}^2 + \sigma_{obs}^2)}$, where $\sigma_{CCM}$ is the average value of the standard deviation about the zonal-mean for all of the CCM days that were used to describe the zonal, monthly mean (the number of days used varies from model to model, but is typically between 3 and 5), $\sigma_{obs}$ is the uncertainty of the observation, and the summation is carried out over the *N* CCM model levels between the tropopause and 1 hPa. Negative values of *g* were set to zero. For the $N_2O$ comparison, the MkIV profile was interpolated *versus* log-pressure to the pressure of each model. For the other comparisons, the "observed relation" of each species *versus* $N_2O$ is interpolated to the CCM value of $N_2O$ at each model level. The tropopause for each model was determined from the zonal monthly mean temperature *versus* pressure profile, using the WMO definition of the thermal tropopause. We averaged between the tropopause and 1 hPa to focus on the part of the stratosphere relevant for ozone loss and

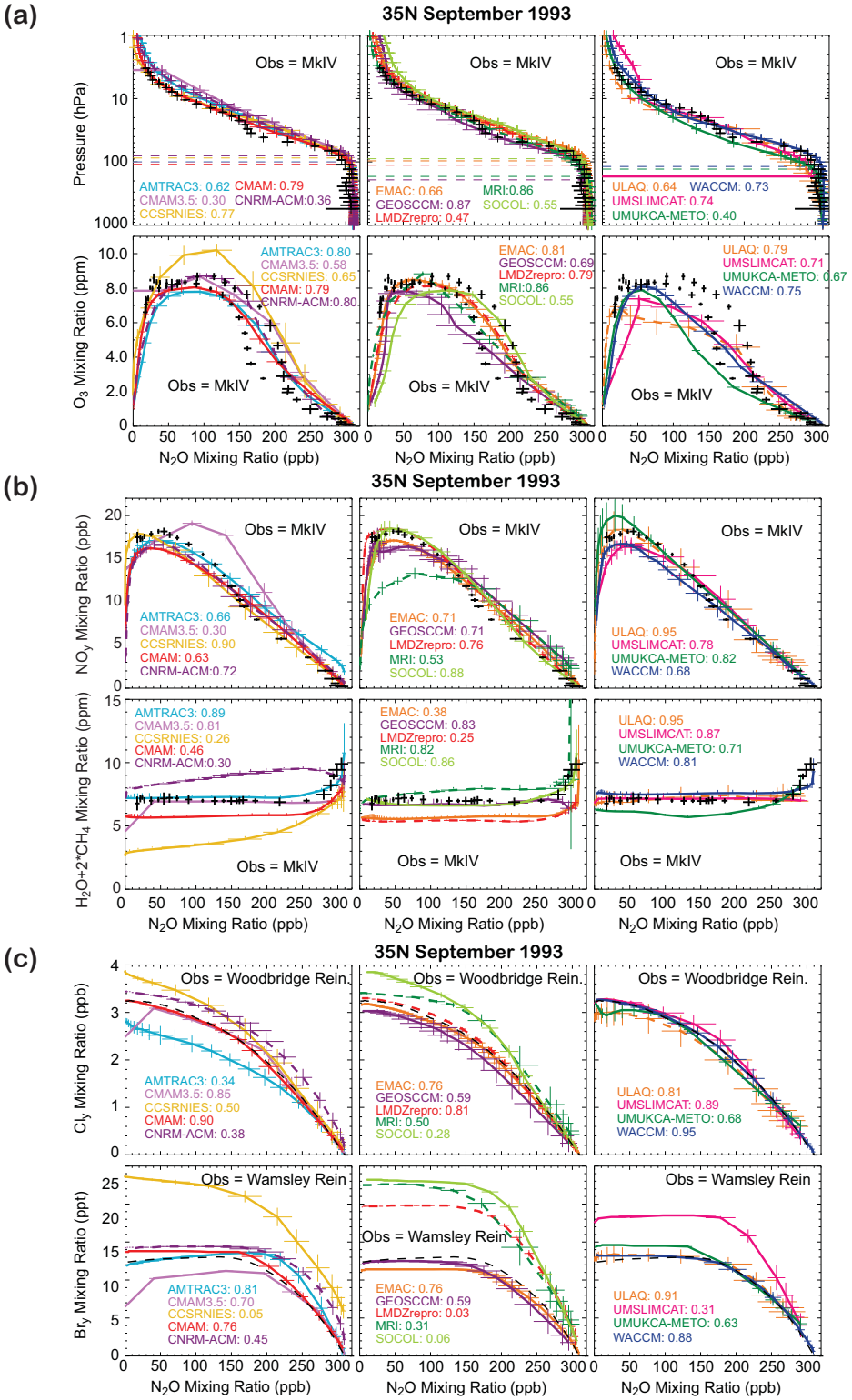


**Figure 6.8:** Comparison of $N_2O$ profiles and the relation of radical precursors versus $N_2O$ (black) to zonal monthly mean values from various CCM models (coloured lines and symbols, as indicated) for 35°N in September 1993. CCM output is for the closest model latitude to 35°N, as indicated. Numerical values of g (see text) are also noted. Comparisons of $N_2O$ vs. pressure and $O_3$ vs. $N_2O$ are shown in panel (a); comparisons of $NO_y$ vs. $N_2O$ and $H_2O+2CH_4$ vs. $N_2O$ are shown in panel (b); comparisons of $Cl_y$ vs. $N_2O$ and $Br_y$ vs. $N_2O$ are shown in panel (c).

recovery calculations.

For the calculation of $g_{precursor}$ we have added an additional constraint on $\sigma_{obs}$: it can never fall below 5%, 10%, 5%, 10%, 2.5%, or 10% of $\mu_{obs}$ for $N_2O$, $O_3$, $NO_y$, $H_{tot}$, $Cl_y$, or $Br_y$, respectively. A "floor" on $\sigma_{obs}$ is essential, because otherwise the quantitative evaluation of $g_{precursor}$ is biased by altitudes where a measurement team might claim to have extraordinarily high accuracy, causing small differences between $\mu_{obs}$ and $\mu_{CCM}$ to be magnified by the low value of the denominator of Equation 6.1. The numerical values given above are based our assessment, based on many years of working with atmospheric chemistry measurements, of how well each parameter is really known. The "floor" on $\sigma_{obs}$ is analogous to "error inflation", a process whereby the uncertainty of meteorological observations is increased prior to assimilation within Numerical Weather Prediction models (*e.g.*, Whitaker *et al.*, 2008; Hamill and Whitaker, 2005). It is reassuring that after application of this additional constrain on $\sigma_{obs}$, the resulting values of $g_{precursor}$ represent the visual impression gleaned from examination of many model/data comparison plots. The high value of 10% for $O_3$ reflects the difficulty inherent in the comparison of the $O_3$ *vs.* $N_2O$ relation measured at a single location, which is sensitive to the dynamical histories of the sampled air parcels, to a relation based on zonal monthly mean profiles from the CCMs. Also, for 35°N, Sept 1993, the MkIV instrument obtained observations on a successive sunset and sunrise (Sen *et al.*, 1998). The observations were similar, except for $O_3$ *vs.* $N_2O$ (Figure 6.8a). Atmospheric observations have revealed that the other tracer relations are much less sensitive to recent air mass history, owing to the longer photochemical lifetimes for $NO_y$, $H_{tot}$, $Cl_y$, and $Br_y$ compared to that for $O_3$. The uncertainty in the observed value of $O_3$ at a particular value of $N_2O$, used to compute $g_{precursor}$, is based on whichever is larger: 10% of the mean value of $O_3$ or the range of $O_3$, defined as one-half of the measurement difference.

As noted above, Figure 6.8 shows the evaluation of the radical precursor fields at ~35°N for September 1993. The models have a range of skill for representation of radical precursors, with some models (*i.e.*, WACCM and ULAQ) providing extremely realistic overall specifications. The measured profile of $N_2O$ is represented reasonably well by all models, with some indicating somewhat more (or less) descent than implied by the observation. The GEOSCCM and MRI models exhibit best agreement with this metric. The models exhibit a range of values for $O_3$ *vs* $N_2O$, reflecting the sensitivity of this metric to recent airmass history. Nonetheless, ten of the models demonstrate very good agreement (*i.e.*, $g_{precursor} > 0.70$) with the observed range of $O_3$ *vs.* $N_2O$ relation. The $NO_y$ *vs.* $N_2O$ relation is represented quite well by most of the models, with the exception of CAM3.5 ($NO_y$ much larger than observation) and MRI ($NO_y$ much less observation).

The models exhibit a range of values for $H_{tot}$, with some models (especially CCSRNIES) exhibiting a too dry stratosphere and other models (especially CNRM-ACM) exhibiting excess moistness. Best simulations of $H_{tot}$ are achieved by AMTRAC, CAM3.5, GEOSCCM, MRI, SOCOL, ULAQ, UMSLIMCAT, and WACCM. The range of values for $H_{tot}$ may reflect the sensitivity of stratospheric $H_2O$ to small differences in tropopause temperature (see Section 6.3.3).

The CCMs exhibit a substantial range in the $Cl_y$ *vs.* $N_2O$ relation, which is surprising because the loss processes of the source gases are well known and the surface abundances have been specified for the REF-B1 simulation. Best agreement is achieved by CAM3.5, CMAM, EMAC, LMDZrepro, ULAQ, UMSLIMCAT, and WACCM. Simulated values of $Cl_y$ at the top of the stratosphere for September 1993 range from a low of ~2.8 ppb (AMTRAC) to a high of ~3.8 ppb (CCSRNIES and SOCOL); observations suggest an actual value of ~3.25 ppb, as indicated. The chlorine loading of the CCM runs is discussed in more detail in Section 6.3.3.

Inorganic bromine ($Br_y$) is the radical precursor field that varies the most among the CCMs. The $Br_y$ *vs.* $N_2O$ relation exhibits a large amount of model to model variability. The REF-B1 calculation was supposed to be carried out with stratospheric bromine supplied only by $CH_3Br$ and halons. Some models (*i.e.*, CCSRNIES, LMDZrepro, MRI, SOCOL, and UMSLIMCAT) also apparently allow for the influence of very short-lived bromocarbons on stratospheric $Br_y$ (see Section 6.3.3 for a full discussion). Other models (*i.e.*, CAM3.5 and EMAC) archived lower values of $Br_y$ than should be present in the mid-latitude stratosphere during September 1993.

**Figure 6.9** shows a comparison of zonal monthly mean values of radicals ($HO_x$, $NO_x/NO_y$, $ClO/Cl_y$, and $BrO/Br_y$) from each CCM to the 24-hour average value of the radicals found using the PSS box model, constrained by profiles of T, $O_3$, $H_2O$, $CH_4$, CO, $NO_y$, $Cl_y$, $Br_y$, and sulfate SAD from the various CCMs. (Similar plots for $O(^3P)$ and $O(^1D)$ are provided in Figure 6S.2 of the Supplementary Material). Metrics, in this case $g_{RADICAL}$ (numerical values given on each panel) are again found using Equation 6.1, with $n = 3$, $\sigma = \sqrt{(\sigma_{CCM}^2 + \sigma_{PSS}^2)}$, and the other CCM terms described as above. Here, $\mu_{obs} = \mu_{PSS}$ and represents 24-hour abundance of radicals found using the latitude, solar declination angle for each CCM from a full diel simulation, and the summation is carried out for the *N* CCM model levels between the tropopause and 1 hPa (between the tropopause and 5 hPa for $BrO/Br_y$). Again, negative values of *g* are set to zero. The quantity $\sigma_{PSS}$ represents the variability of the PSS output found by perturbing, relative to the baseline run, values of nine input parameters given above by the standard deviation, about the zonal mean, of these quantities from each CCM. This variability is represented by the

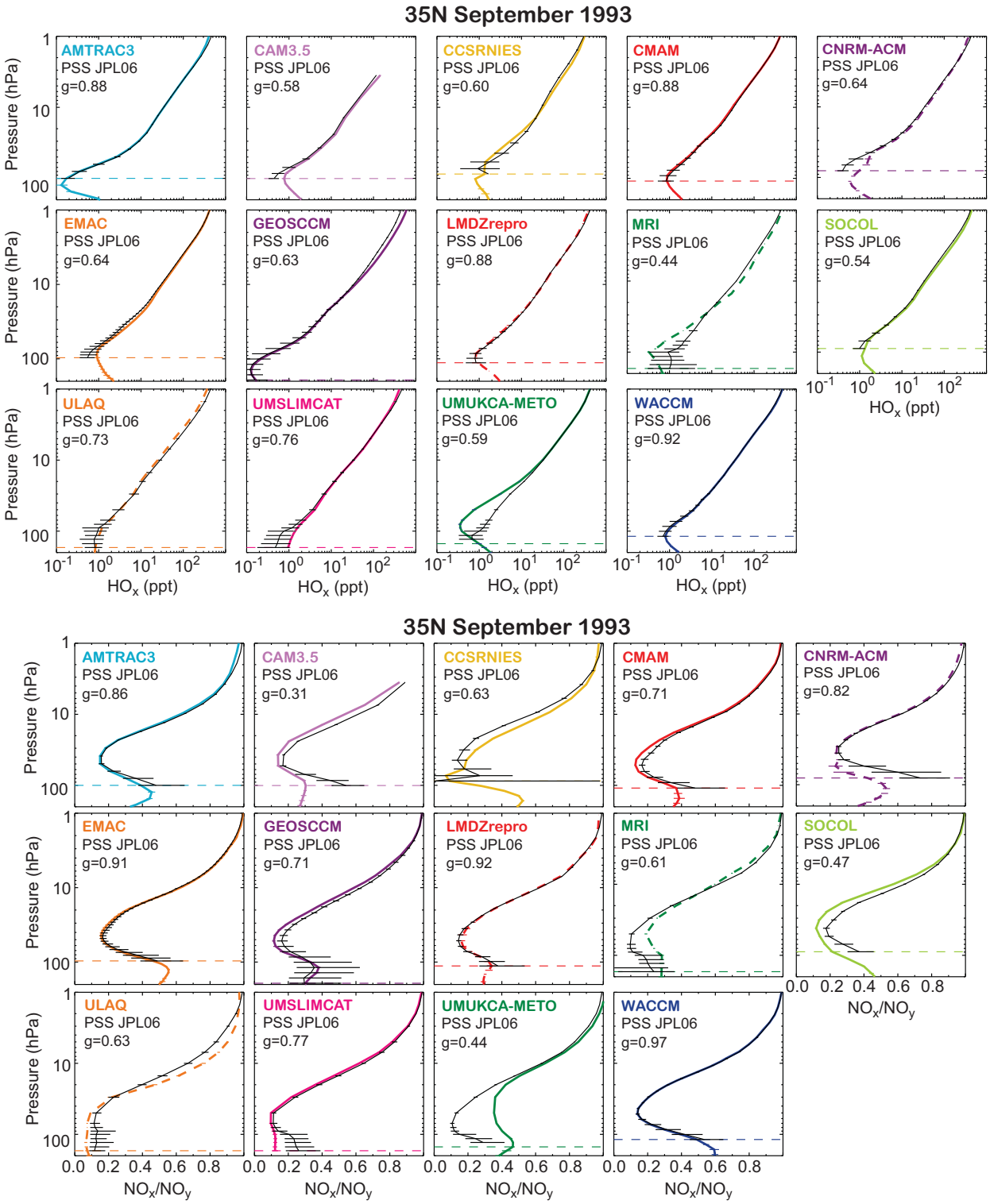


**Figure 6.9:** Comparison of zonal monthly mean profiles of radicals from CCM models (coloured lines and symbols) versus 24-hour average radical profiles found using a PSS box model constrained by profiles of T, $O_3$, $H_2O$, $CH_4$, CO, $NO_y$, $Cl_y$, $Br_y$, and sulfate SAD from the various CCMs for 35°N in September 1993. The PSS model was run for CCM model levels from the tropopause (dashed lines) to 1 hPa. The PSS model uses the latitude of the CCM output that is closest to 35°N and solar declination corresponding the the mid point of the monthly mean. Numerical values of g and the chemical kinetics in the simulation are given (see text). The

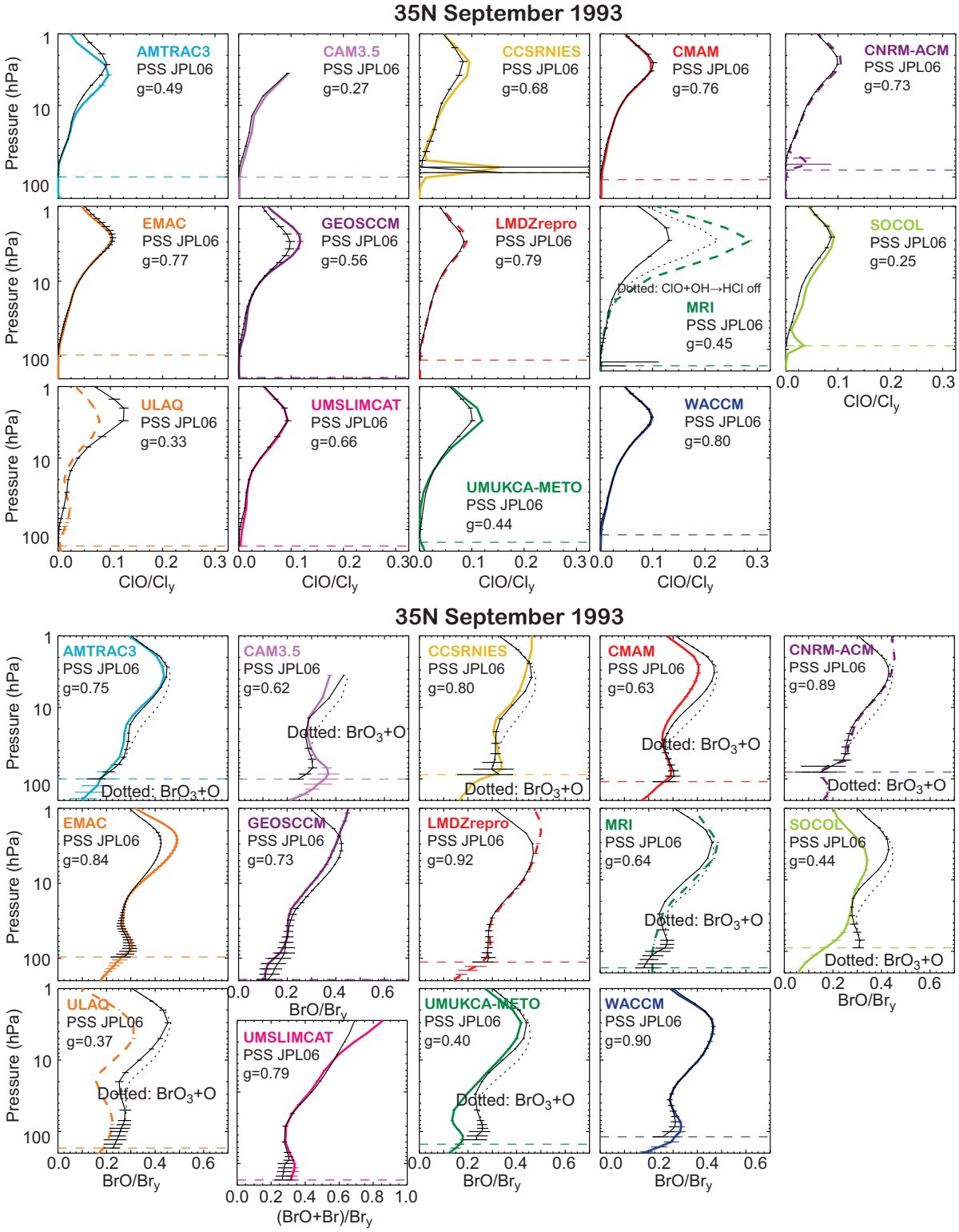


coloured error bars represent the standard deviation about the zonal monthly mean for various days used to compute the mean. The black error bars represent the sensitivity of PSS output to variability in the CCM profiles of radical precursors. Results for $HO_x$, $NO_x/NO_y$, $ClO/Cl_y$, and $BrO/Br_y$ are shown, respectively, in panels (a), (b), (c), and (d). For the MRI model, results are shown with and without production of HCl by the chemical reaction ClO+OH (see text). For AMTRAC, CAM3.5, CCSRNIES, CMAM, CNRM-ACM, MRI, SOCOL, ULAQ, and UMUKCA-METO, results are shown with and without consideration of the reaction $BrONO_2$+O (see text).

black error bars in Figures 6.9. Typically, $\sigma_{PSS}$ peaks in the lowermost stratosphere, reflecting the sensitivity of radicals to zonal asymmetry in this region of the atmosphere. For the calculation of $g_{RADICAL}$, the value of $\sigma_{PSS}$ is floored at 5% of the value of $\mu_{PSS}$ (the figures show $\sigma_{PSS}$ before this floor is imposed). Flooring $\sigma_{PSS}$ at a modest, non-zero value is crucial to the proper use of the PSS model to assess the chemical mechanism within CCMs, because often the radical profiles found from a CCM model will follow the general shape of the PSS profile, but be 3 to 5% systematically high (or low) at many levels. If we allowed $\sigma_{PSS}$ to reflect only the propagation of variability in the precursors through the PSS model, the calculation of $g_{RADICAL}$ would be biased whenever the variance about the zonal-mean of the radical precursors (from the CCM) leads to very small perturbations in radical fields (*i.e.*, whenever an unduly small value for the denominator of Equation 6.1 is found).

We chose $O(^3P)$, $O(^1D)$, $HO_x$, $NO_x/NO_y$, $ClO/Cl_y$, and $BrO/Br_y$ as our basis for comparison because these species participate in the crucial rate limiting steps for loss of ozone and/or other long-lived stratospheric gases. The ratios $NO_x/NO_y$, $ClO/Cl_y$, and $BrO/Br_y$ are used because these quantities are less sensitive to dynamical variability than values of $NO_y$, ClO, and BrO. Presumably, if the PSS model, using precursor fields from the CCM, accurately simulates the values of $O(^3P)$, $O(^1D)$, $HO_x$, $NO_x/NO_y$, $ClO/Cl_y$, and $BrO/Br_y$ found by the CCM, then both models represent a "chemical mechanism" in a similar manner.

Figure 6S.2a shows comparisons for $O(^3P)$. With the exception of the MRI model, the comparisons are uniformly very good to excellent (note: three of the CCM groups failed to archive fields of $O(^3P)$). Larger differences are found for $O(^1D)$ (Figure 6S.2b). The values of $g_{RADICAL}$ range from a high of 0.83 (CAM3.5) to a low of 0.23 (MRI), with four CCM groups failing to archive fields of $O(^1D)$.

The shape and magnitude of the $HO_x$ profile found by the PSS simulation agrees well with the profile found by most CCMs (Figure 6.9a). Differences are typically largest in the lower stratosphere, where the influence of zonal asymmetry is largest (highest values of $\sigma_{PSS}$). Profiles of $HO_x$ reported by AMTRAC, CMAM, LMDZrepro, ULAQ, UMSLIMCAT, and WACCM are simulated in a very good to excellent manner. The shape and magnitude of the $NO_x/NO_y$ ratio from the various CCMs, as for $HO_x$, is generally simulated quite well by the PSS model (Figure 6.9b). Excellent agreement is achieved for EMAC, LMDZrepro, and WACCM. The large differences between the PSS simulation and the value of $NO_x/NO_y$ archived in the lower stratosphere by a few of the CCMs suggests either misrepresentation of sulfate SAD within the PSS model (fields of sulfate SAD were not archived by CCM groups with some of the largest differences) or else the effect of volcanic aerosols on chemical composition is represented in a different manner by the respective models compared to the representation in the PSS model. In general, when the value of $NO_x/NO_y$ in the lower stratosphere from the PSS model exceeds the value from a CCM (*i.e.*, UMSLIMCAT), then the value of $HO_x$ from the PSS model falls below the value from the CCM (UMSLIMCAT). When $NO_x/NO_y$ from PSS falls below that from a CCM (*i.e.*, UMUKCA-METO and MRI), then generally $HO_x$ from PSS exceeds that of the CCM. This interplay between the two radical families is "as expected" (*e.g.*, Wennberg *et al.*, 1994); it is reassuring to see this characteristic of the comparisons shown in Figures 6.9a and 6.9b.

Figure 6.9c shows the comparison for $ClO/Cl_y$. In nearly all cases, the PSS and CCM profiles follow a similar shape. However, for some CCMs, the magnitudes are quite different. Best agreement is achieved for CMAM, CNRM-ACM, EMAC, LMDZrepro, UMSLIMCAT, and WACCM. The peak value of $ClO/Cl_y$ is highly overestimated, with respect to the PSS simulation, by the MRI model. This overestimate is due in part to the neglect of the $ClO + OH \rightarrow HCl$ product channel in the MRI model (Table 6S.1). We have conducted another PSS simulation neglecting this product channel, to better approximate the chemical mechanism used by MRI. Neglecting this product channel results in a profile for $ClO/Cl_y$ that lies closer to the MRI profile (dotted line, MRI panel, Figure 6.9c), but the MRI value of $ClO/ClO_y$ still exceeds the PSS value. For the computation of the $g_{RADICAL}$, we have used the PSS simulation that includes the HCl product channel, because production of HCl by ClO+OH is a key component of the "standard" stratospheric photochemical mechanism in use for the past decade. The profile of $ClO/Cl_y$ is somewhat overestimated by GEOSCCM, near the peak, for reasons that are unclear. For ULAQ, values of $ClO/Cl_y$ are strongly under-estimated in the upper stratosphere and strongly overestimated in the lower stratosphere. Use of a linear coordinate for the horizontal axis obscures some important differences in the lower stratosphere, such as the presence of quite large values of $ClO/Cl_y$ by the CNRM-ACM and SOCOL models.

Figure 6.9d shows the comparison for $BrO/Br_y$. For the 2 CCMs that use JPL-2002 kinetics (EMAC and GEOSCCM) as well as the 3 CCMs that use JPL-2006 kinetics and include the $BrONO_2$+O reaction (LMDZrepro, UMSLIMCAT, and WACCM), one PSS curve is shown. For the other 7 CCMs, the results of PSS simulations both including and neglecting this reaction are shown. The numerical value of $g_{RADICAL}$, in all cases, represents the best PSS representation of the CCM chemistry, as given in Table 6S.3. Since the PSS simulation diverges from many (but not all) of the CCMs at low pressure, where bromine chemistry is not important, we use 5 hPa as the maximum altitude for the calculation of $g_{RADICAL}$ for this ratio. Finally, the UMSLIMCAT group has archived BrO + Br, rather

than BrO, resulting in the display of a different quantity for this CCM.

The CCMs exhibit a wide range of variability for the representation of $BrO/Br_y$ (Figure 6.9d). Best agreement with the PSS model is achieved for CCSRNIES, CNRM-ACM, EMAC, LMDZrepro, MRI, UMSLIMCAT, and WACCM. Some of the other models (*i.e.*, SOCOL, ULAQ, and UMUKCA-METO) exhibit considerable differences with respect to the PSS simulation.

**Figure 6.10** represents grades for $g_{PRECURSOR}$ and $g_{RADICAL}$ for the 35°N, Sept 1993 simulation from all of the models. The values of these metrics shown in Figures 6.7, 6.8 and 6.9 are represented by the shaded squares, as indicated. Two new pieces of information are represented in Figure 6.10:

1. An additional metric, a measure of the tropospheric abundance of $Cl_y$ in each CCM (termed $Cl_y$ Tropos), has been added;
2. the cell for $BrO/Br_y$ has been split, with the left side representing the metric when the $BrONO_2$+O reaction is included (if JPL-2006 kinetics are used in the CCM) and the right side representing the metric when this reaction is excluded (if JPL-2006 kinetics are used in the CCM and this reaction was not included in the chemical mechanism, as shown in Table 6S.2).

The additional metric for $Cl_y$ Tropos was assessed by examination of the value of $Cl_y$ at 500 hPa archived by each CCM for 35°N, Sept 1993. Some of the CCM models have high (*i.e.*, >> 50 ppt) levels of $Cl_y$ extending from the surface to the tropopause that impacts the model value of $Cl_y$ throughout the lowermost stratosphere (LMS); these models will undoubtedly have a different sensitivity of $O_3$ to changes in temperature in the LMS compared to models with near zero (<< 50 ppt) of $Cl_y$ from the surface to the tropopause. Models with high values of $Cl_y$ Tropos have the potential for chlorine activation in the extra-polar LMS as temperature approaches 198 K that will affect ozone much more strongly than for the models with $Cl_y$ Tropos ≈ 0. The metric for $Cl_y$ Tropos assumed $\mu_{obs} = 0$ and $\sigma_{obs} = 50$ ppt, which proved to be an excellent discriminate between models with $Cl_y$ Tropos ≈ 0 and models with excessive $Cl_y$ Tropos (which is clearly associated with elevated levels of $Cl_y$ in the LMS within these models). The CCSRNIES, CNRM-ACM, MRI, SOCOL, ULAQ, and UMUKCA-METO models have $Cl_y$ >> 50 ppt at the tropopause and throughout the troposphere, whereas the AMTRAC, CAM, EMAC, GEOSCCM, LMDZrepro, and WACCM models have $Cl_y$ << 50 ppt for these regions of the atmosphere. In general, models with high values of $Cl_y$ in the troposphere also archived high values of $Br_y$ (>> 2 ppt) in the troposphere (we did not develop a metric for $Br_y$ Tropos).

The metric for $BrO/Br_y$ in Figure 6.10 was split to indicate the sensitivity of the fast chemistry evaluation to a single chemical reaction and to incorporate, into the overall total fast chemistry metric, a quantification of the failure of some CCM groups to properly represent the JPL-2006 chemical mechanism. It is important to note that the same numerical value is given on both sides of the $BrO/Br_y$ grading cell for CCMs that either used JPL-2002 kinetics (the $BrONO_2$+O reaction was not included in JPL-2002) or else used JPL-2006 kinetics and represented this reaction. The values on the left and right side of the $BrO/Br_y$ grading cell thus differ only for CCMs that used JPL-2006 kinetics and neglected this new reaction. For 7 of the 8 models that neglected the $BrONO_2$+O reaction, the metric on the right hand side of the $BrO/Br_y$ cell improves when this reaction is neglected within the PSS simulation (the exception is MRI, a model for which the simulation of $NO_x$ is not matched by PSS). This behaviour suggests that the fast chemistry evaluation has the fidelity to assess the inclusion (or neglect) of a single chemical reaction within a complex CCM.

The last column of Figure 6.10 represents the total fast chemistry metric for the 35°N, Sept 1993 simulation. The numerical value is the mean of all available metrics (precursors, radicals, and sulfate SAD). The mean of the two $BrO/Br_y$ values is used, representing a compromise to take into consideration the neglect of an important new chemical reaction by the CCM groups that used JPL-2006 kinetics but omitted this $BrONO_2$+O reaction, while at the same time factoring into the grade how well the CCM fares when this reaction is also neglected within the PSS simulation. The total metric includes a demarcation if sulfate SAD was not reported (*), if the CCM did not use JPL-2006 kinetics (◊), and if the CCM group failed to provide adequate information to participate in the fast chemistry evaluation (×). Overall, the CMAM, EMAC, UMSLIMCAT, and WACCM models fared best in the fast chemistry metric for Sept 1993, with the AMTRAC, GEOSCCM and LMDZrepro models not far behind.

We conclude this section with a brief, *albeit* very important summary of the fast chemistry evaluation for 22°N, February 1996. Data used for this evaluation were obtained by instruments aboard the NASA ER-2 aircraft during the STRAT campaign (*e.g.*, Lanzendorf *et al.*, 2001; Weinstock *et al.*, 2001; Dessler, 2002). Figure 6.7 shows profiles of sulfate SAD for this period. As is well known, the highly perturbed volcanic aerosol characteristic of September 1993 had fallen considerably by February 1996 (note the different scales used for the horizontal axes in Figure 6.7).

We have repeated the entire analysis (precursors and radicals) for February 1996. Figures analogous to those shown for the September 1993 time period can be found in the Supplementary Material (Figures 6S.3, 6S.4, and 6S.5). Here, in **Figure 6.11,** we show only scatter diagrams of the values of: $g_{PRECURSOR}$ ($N_2O$ profiles; $O_3$, $NO_y$, $H_{tot}$, $Cl_y$,

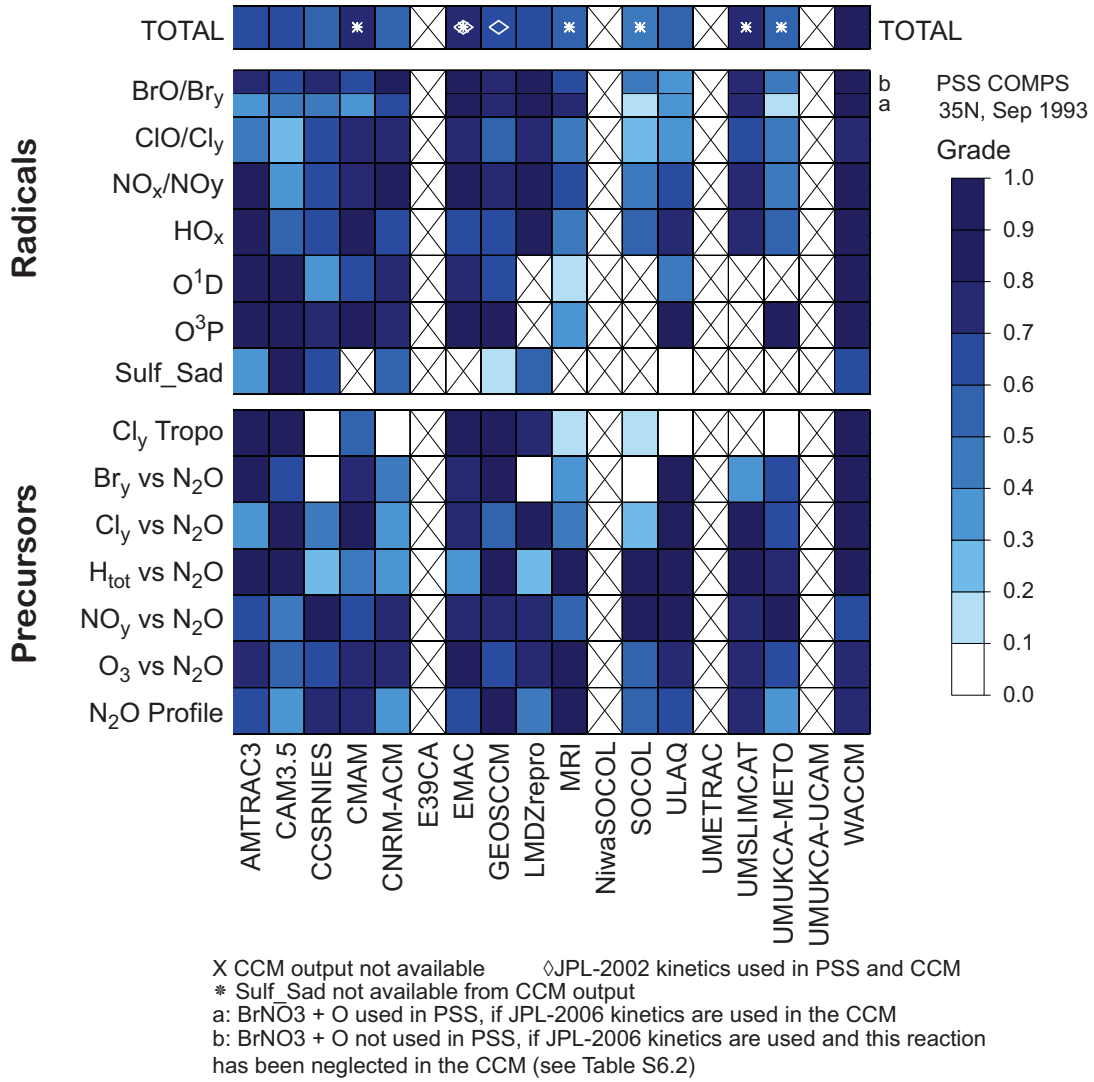


**Figure 6.10:** Metrics for (a, left) radical precursors and (b, right) sulfate surface area and radicals for a simulation carried out at 35°N, September 1993. The same dark shade of blue is used for 0.8 < g < 1.0, reflecting that there is little significance in differences that fall within this range of values. The symbol X denotes CCM output not archived; ◊ denotes use of JPL-2002 kinetics, and * denotes sulfate SAD not archived (see text). For model that used JPL-2006 kinetics and neglected the $BrONO_2$+O reaction, two grades are given for the evaluation of $BrO/Br_y$ (see text).

and $Br_y$ all *vs*. $N_2O$; $Cl_y$ Tropos) for the Feb 1996 *vs*. Sept 1993 evaluations (top panel); $g_{RADICAL}$ (sulfate SAD, $O(^3P)$, $O(^1D)$, $HO_x$, $NO_x/NO_y$, $ClO/Cl_y$, and $BrO/Br_y$) for the Feb 1996 *vs*. Sept 1993 evaluations (middle panel); and total fast chemistry metric for the Feb 1996 *vs*. Sept 1993 evaluations (bottom panel). Numerical values of the respective metrics (mean of the Feb 1996 and Sept 1993 evaluations) are given in the list to the right of each figure, placed in order of the total overall fast chemistry metric (bottom panel). In all cases, the metrics scatter about the 1:1 line. For the precursors, the notable outliers are the $N_2O$ profile and the $O_3$ *vs*. $N_2O$ relation for MRI (this model exhibits much better agreement with Sept 1993 observations than with Feb 1996 data). Removing these two outliers results in a value for $r^2$ of 0.67 and a slope of 1.01, for the rest of the evaluation points. Therefore, the metric for a particular precursor from a specific CCM for the first time period is generally a good predictor of the metric for the second time period. For the radicals, the notable outliers are sulfate SAD for GEOSCCM and ULAQ as well as $O(^1D)$, $HO_x$, and $O(^3P)$ from ULAQ. The outlier for sulfate SAD from GEOSCCM is due to use of background aerosol loading at all times. The sulfate SAD used by ULAQ bears a closer relation to the climatology for Feb 1996 than for Sept 1993, for reasons that are unclear. It is also not clear why the good to very good ability of the PSS model to simulate

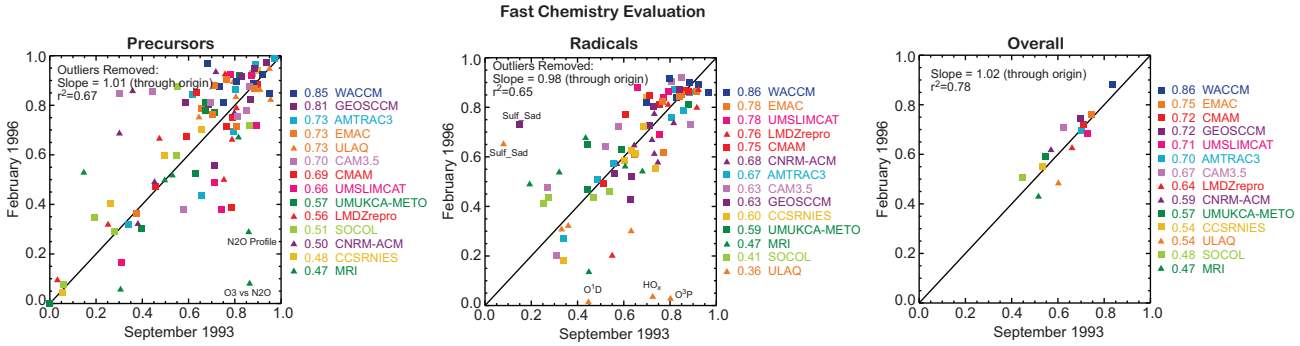


**Figure 6.11:** (Top panel): Scatter plot of metrics for the radical precursors for the simulation carried out at 35°N, September 1993 (horizontal axis) vs. metrics for the same quantities from the 22°N, February 1996 simulation (vertical axis). (Middle panel): Scatter plot of metrics for sulfate surface area and radicals for the simulation carried out at 35°N, September 1993 vs. metrics for the same quantities from the 22°N, February 1996 simulation. For models that archived all quantities, points represent the metrics for sulfate SAD, $O(^3P)$, $O(^1D)$, $HO_x$, $NO_x/NO_y$, $ClO/Cl_y$, and $BrO/Br_y$ from both time periods. The geophysical quantity associated with the various outliers is denoted (see text). (Bottom panel): Scatter plot of the total fast chemistry metric (last column of Figure 6.10 and Figure 6S.5) for the simuation carried out at 35°N, September 1993 vs. metrics for the same quantities from the 22°N, February 1996 simulation. The metric points, excluding the outliers, have a variance ($r^2$) of 0.67, 0.65, and 0.78 for the three panels, respectively, indicating that about two-thirds of the variance in the precursor and radical metrics, and almost 80% of the variance of the overall fast chemistry metrics is common between both time periods. Slopes of a linear least squares fit are also indicated; for the precursor and radical evaluations, these slopes have been forced to pass through the origin.

$O(^3P)$, $O(^1D)$, and $HO_x$ within ULAQ for Sept 1993 is not reflected in the Feb 1996 comparisons (see Figure 6S.4). Removal of these five outliers results in a value of $r^2$ of 0.65 and a slope of 0.98.

The total fast chemistry metrics (cells titled "Total" in Figure 6.10 and Figure 6S.5) exhibit a strong correlation ($r^2$ = 0.78; slope = 1.02) considering all of the evaluation points (bottom panel, Figure 6.11). This scatter diagram demonstrates the robustness of the conclusions of the fast chemistry evaluation. Some of the models (WACCM, EMAC, GEOSCCM, CMAM, UMSLIMCAT, AMTRAC) have implemented a more realistic representation of fast chemistry than the models that rank on the low end of this metric. In all cases, performance in the Sept 1993 evaluation is an excellent predictor (78% of the variance) of the performance in the Feb 1996 evaluation.

## 6.3.3 Evaluation of Reservoir and Long-Lived Chemistry

### 6.3.3.1 Tracer-tracer correlations

A concise way of inter-comparing important aspects of CCM results, and identifying model-model differences, is by plotting correlations of long-lived tracer fields. These correlations can be used to investigate transport properties (see Chapter 5), but also reveal some chemical information. Section 6.3.2 used correlations to analyse radical precursors near the locations of balloon flights, but in this section we use them to condense multi-annual global data sets. Figures 6.12 to 6.14 show the $CH_4$:$N_2O$, $CH_4$:$H_2O$ and $NO_y$:$N_2O$ correlations from the last 10 years of the REF-B1 runs of 17 CCMs (no data was provided from UMETRAC). Figures 6.12 to 6.14 also show corresponding ENVISAT Michelson Interferometer for Passive Atmospheric Sounding (MIPAS) data. This data was produced using the University of Oxford Retrieval (A. Dudhia, personal communication, 2009). Other MIPAS retrievals exist but the choice of data set should not be critical for the comparisons (species and spatial averaging) performed here.

For $CH_4$:$N_2O$ (**Figure 6.12**) most CCMs produce a compact correlation in good agreement with the straight-line fit inferred from ER-2 and MIPAS data down to 50 ppbv $N_2O$. The ER-2 data corresponds to the lower stratosphere and so represents a sub-sample of the global MIPAS data. The altitude variation of the correlation (indicated by the colours) is also quite similar between many models. The lower resolution ULAQ model gives a larger spread in the correlation than other models, but then so does the MIPAS data. The low-lid E39CA model diverges from the straight line correlation at the lowest values of $CH_4$ and $N_2O$, although the other model with a relatively low lid, CAM3.5, performs well.

**Figure 6.13** is a similar plot for $CH_4$ and $H_2O$. In the stratosphere, the oxidation of $CH_4$ will lead to the production of up to 2 molecules of $H_2O$ (the alternative minor

ultimate product is $H_2$). In contrast to $N_2O$, there is therefore a direct chemical link between these two tracers. As expected the CCMs generally show large mixing ratios of water vapour in the troposphere (*i.e.*, for large $CH_4$), a minimum in the lower stratosphere followed by an increase in the stratosphere as $CH_4$ decreases. The variation in stratospheric maximum $H_2O$ as a function of $CH_4$ in most models tends to follow the line $H_{tot}$ = 7 ppmv (although the MIPAS data indicates $H_{tot}$ may be 0.5-1.0 ppmv larger than this). Notable exceptions to this behaviour are: CCSRNIES which shows small lower stratosphere $H_2O$ mixing ratios and only a small stratospheric increase (*i.e.*, less than 2 molecules $H_2O$ per $CH_4$ oxidised); UMUKCA-METO, which shows similar smaller stratospheric $H_2O$ and a smaller stratospheric production, and also LMDZrepro. A failure of a model to reproduce this slope of 2 indicates a failing

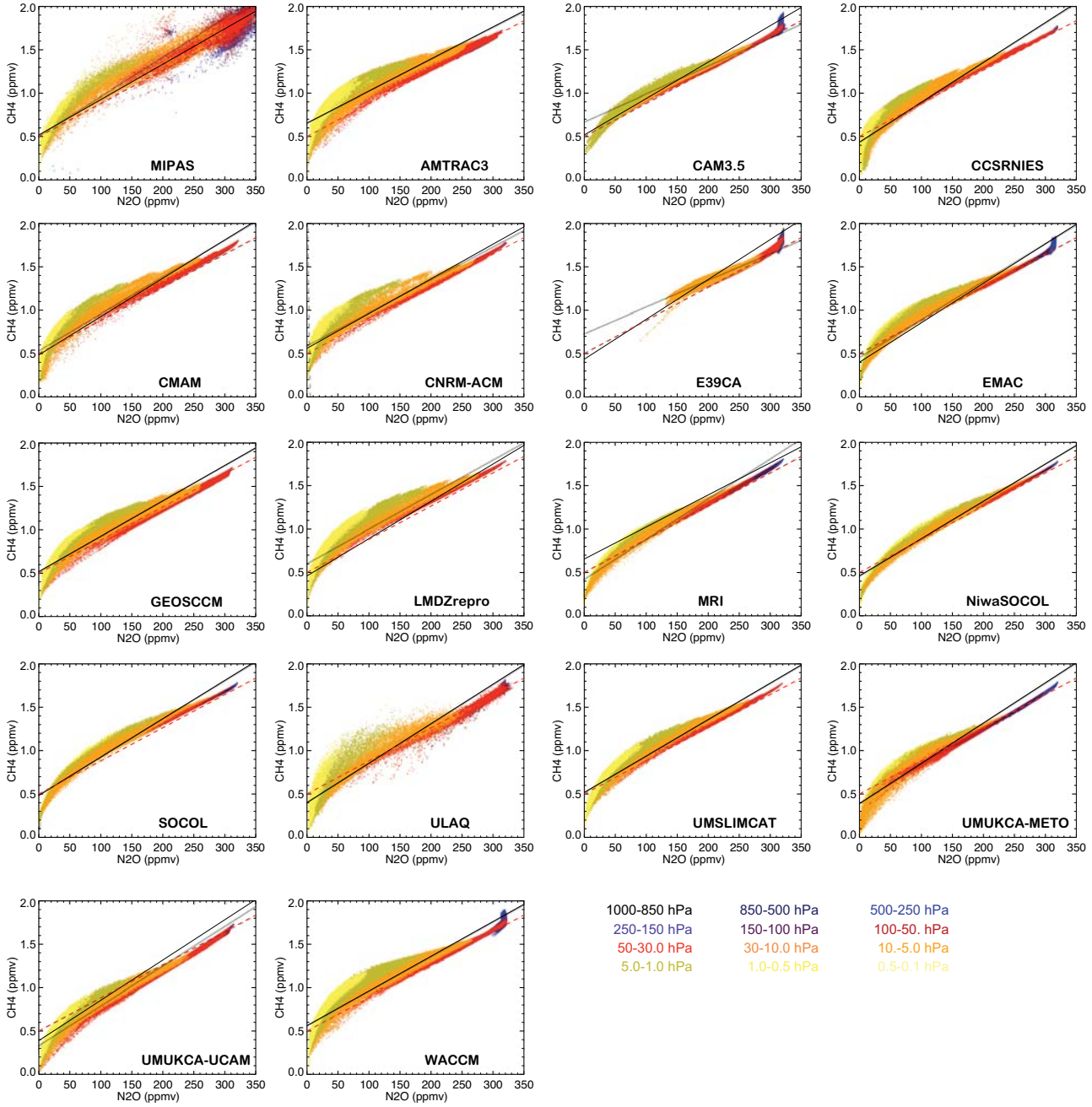


**Figure 6.12:** Correlation of $CH_4$ (ppmv) vs. $N_2O$ (ppbv) for zonal-mean monthly-mean output from the final 10 years of REF-B1 runs from 17 CCM runs and MIPAS data. The solid line is the best fit to the model/satellite data sampled between 60°N-60°S, 70-0.5 hPa. The dashed line shows the equation $N_2O$ (ppbv) = 261.8$CH_4$ (ppmv) – 131, which is a fit from lower stratospheric ER-2 data (see Kawa et al., 1993).

of the chemistry. The CNRM-ACM model appears to have a slope slightly larger than 2 and a stratosphere that is too moist. Other models reproduce the stratospheric slope of 2 but have lower stratospheric $H_2O$ overall due presumably to different input at the tropical tropopause. This is not a failing of the chemistry scheme, which is being evaluated here, but these low $H_2O$ mixing ratios will have an impact on calculated model $HO_x$ for example.

$N_2O$ is the main source of stratospheric $NO_y$ and in the CCMVal runs the only source considered. Overall, stratospheric $N_2O$ has 3 destruction channels:

$$N_2O + h\nu \rightarrow N_2 + O \qquad (6.2a)$$

$$N_2O + O(^1D) \rightarrow 2NO \qquad (6.2b)$$

$$N_2O + O(^1D) \rightarrow N_2 + O_2 \qquad (6.3c)$$

Section 6.3.2 examined the $NO_y$:$N_2O$ correlation for a specific location in September 1993. **Figure 6.14** shows

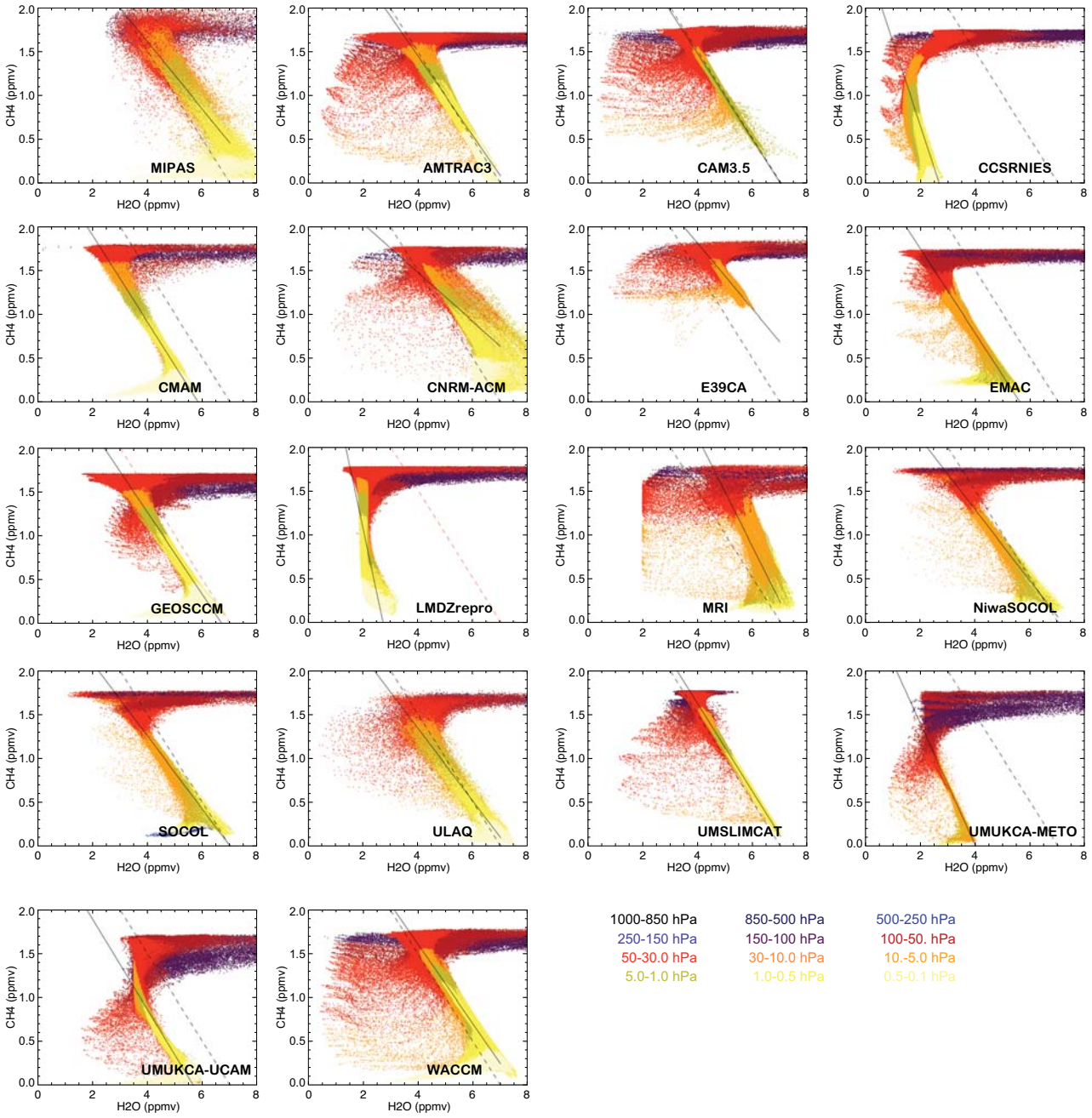


**Figure 6.13:** Correlation of $CH_4$ (ppmv) vs. $H_2O$ (ppmv) for zonal-mean monthly-mean output from the final 10 years of REF-B1 runs from 17 CCMs and MIPAS data. The solid line is the best fit to the model/satellite data sampled between 60°N-60°S, 70-0.5 hPa. The dashed line shows the equation $H_2O + 2CH_4 = 7$ ppmv.

the global correlation of these two species. MIPAS $NO_y$ has been calculated using observed night-time $NO_2$, $HNO_3$, $N_2O_5$ and $ClONO_2$. At lower altitudes (high $N_2O$) there is generally a straight line correlation. The slope of this depends on the modelled yield of $NO_y$ from $N_2O$ (6.2b, around 6%), compared to the loss by the other channels (mainly 6.2a, but also 6.2c). For some models there is a variation of this slope at high $N_2O$ with, for example, SOCOL, UMUKCA-UCAM, UMUKCA-METO and CAM3.5 giving a higher yield. Consequently the range of peak $NO_y$ in the mid-stratosphere in these models varies from 17 to 25 ppbv. The turn-over of the correlation and low $N_2O$ is caused by loss of $NO_y$ through:

$$NO + h\nu \rightarrow N + O \qquad (6.3)$$

$$NO + N \rightarrow N_2 + O \qquad (6.4)$$

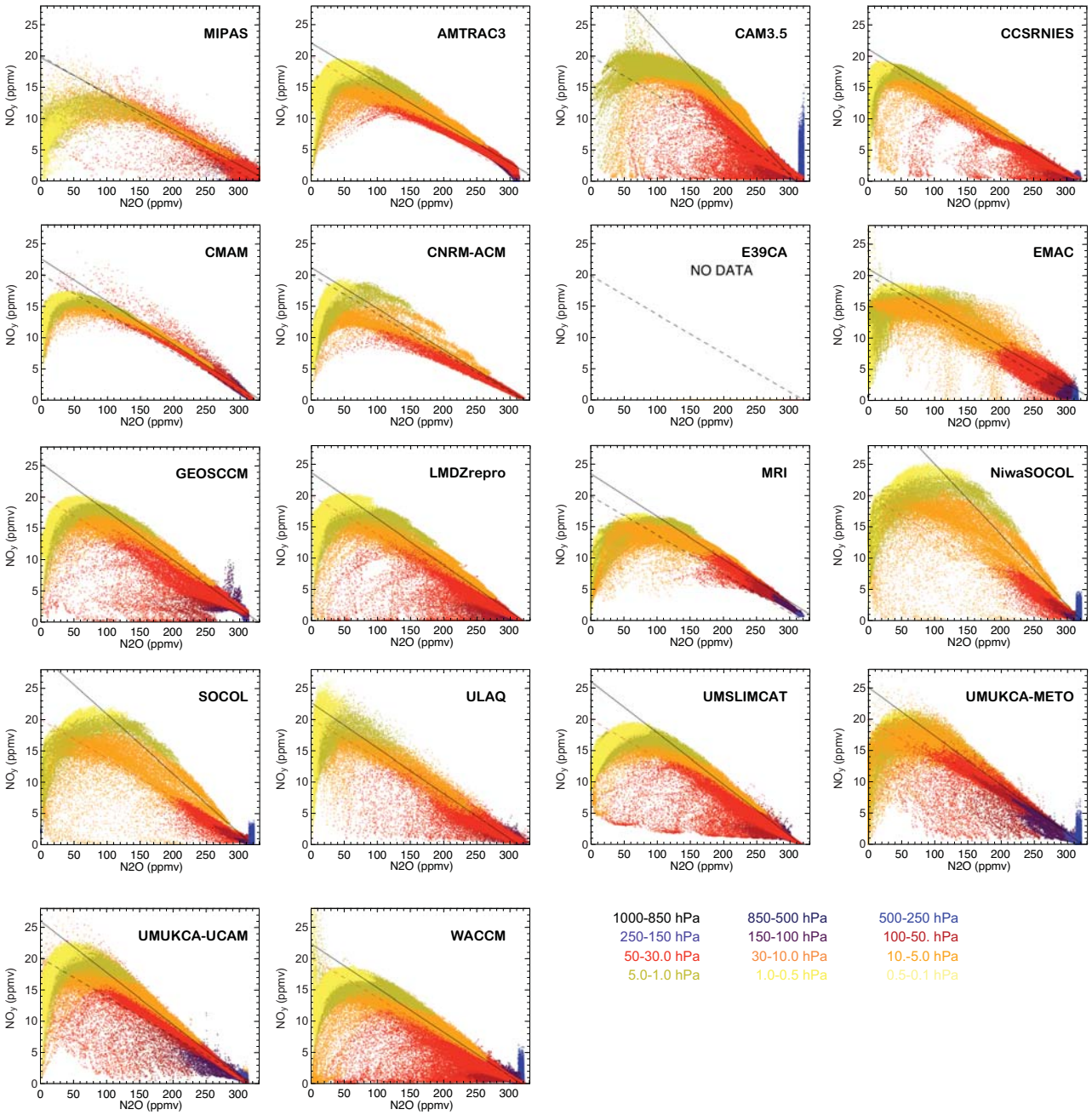


**Figure 6.14:** Correlation of $NO_y$ (ppbv) vs. $N_2O$ (ppbv) for zonal mean monthly mean output from the final 10 years of REF-B1 runs from 16 CCMs (no E39CA results). The solid line is the best fit to the model/satellite data sampled between 30°N-30°S, 70-10 hPa. The dashed line shows the equation $NO_y$ (ppbv) = 20.0 – 0.0625$N_2O$ (ppbv), based on mid-latitude balloon profiles and ER-2 data (see Kondo et al., 1996).

There is a large variation in the shape of this turn-over. This will be partly related to large differences in J-NO (see Section 6.3.1). Figure 6.14 also reveals the impact of Antarctic denitrification. All models show this, but the denitrification appears larger in some models, *e.g.*, WACCM appears to have the most extensive denitrification, while some models have little or none. This is discussed in more detail in Section 6.3.4.

The agreement of these tracer-tracer correlations with observations in the stratosphere has been quantified in the following way:

1. The difference between the fitted stratospheric slopes between a model and observations (see figures) is calculated.
2. If this difference is larger than 3x the observed slope then the score = 0.1.
3. If this difference is greater than 2x the observed slope, but less than 3x, then the score = 0.2.
4. Otherwise the score is calculated using Equation (6.1) with n = 2 and error (s) in the estimated slope = 1%.

The multi-model mean is calculated by summing the slopes from all the models and following the same procedure as steps (2)-(4). **Figure 6.15** shows the results of this grading for the 3 tracer-tracer correlations. The grades for $CH_4$:$N_2O$ are uniformly high showing that this is well modelled. For most models, the score for $CH_4$:$H_2O$ is also high, but lower scores apply to the models which do a poor job of stratospheric $H_2O$. For $NO_y$:$N_2O$ the scores are again generally good with lower scores for CAM3.5, NiwaSOCOL and SOCOL.

### 6.3.3.2 Comparison with satellite climatologies

This section compares climatologies of long-lived and reservoir species from the CCMs with satellite data. We compare the mean annual cycle at two altitudes (1 hPa and 50 hPa) and 3 latitude bands (30°S-60°S, 15°N-15°S, 60°N-30°N) and mean annual profiles in the same regions. Satellite climatologies of relevant species have been provided from MIPAS (Oxford retrieval, A. Dudhia, personal communication, 2009), the Atmospheric Chemistry Experiment FTS instrument (ACE-FTS) (A. Jones and K. Walker, personal communication 2009; Bernath *et a*l., 2005), ODIN (J. Urban, personal communication 2009, Murtagh *et al*., 2002) and SCIAMACHY (A. Rozanov and B. M. Sinnhuber, personal communication, 2009; Rozanov *et al*., 2005; Sinnhuber *et al*., 2005). We do not have space here to show all comparisons; the Supplementary Material contains further plots (Figures 6S.6 to 6S.9).

**Figures 6.16** and **6.17** compare the mean annual cycles at 50hPa, 30°N-60°N, and annual mean profiles at 30°S-60°S, respectively for a range of species. For $CH_4$ UMUKCA-METO and UMUKCA-UCAM give values which are only around 1.0 ppmv at 50 hPa compared to the observed 1.4 ppmv, presumably as a consequence of their slow stratospheric circulation (Chapter 5). The two models with relatively low lids, E39CA, and to a lesser extent CAM3.5, overestimate lower stratosphere $CH_4$, probably as they do not treat loss at higher levels. The $H_2O$ comparisons again show the large variation seen in CCMs discussed earlier. For CO the majority of models overestimate the observations in the mid-lower stratosphere with CCSRNIES being particularly large, followed by MRI, SOCOL, CNRM-ACM, NiwaSOCOL, UMUKCA-METO, LMDZrepro, and CMAM. For HCl there is, overall, a larger than expected spread in the model results, bearing in mind that this is the largest contributor to inorganic chlorine, which in itself should be well constrained in the REF-B1 experiment. At 50 hPa the UMUKCA-METO model has very large values (over 2 ppbv), although the agreement with the profile is reasonable at higher altitudes. The CCSRNIES, NiwaSOCOL, and SOCOL models also have larger mixing ratios than observed. These upper stratospheric mixing ratios exceed that possible based on the REF-B1 halocarbon scenarios (see discussion of total chlorine below). For $ClONO_2$ models tend to capture the mid-latitude seasonal cycle *albeit* with a spread of values. The MRI model gives significantly larger values than the other models. The picture is similar for $HNO_3$, although in this case the UMUKCA-UCAM model has anomalously large values, *e.g.*, ~10 ppbv at 50 hPa in the mid-latitudes. For $N_2O_5$ UMUKCA-METO this time has large values in the lower stratosphere and upper troposphere. A detailed comparison for this species would have to allow for its diurnal cycle, but this discrepancy, which is not shown by other models, is much larger than any issue to do with that. While the differences in HCl between the two versions of UMUKCA can be explained by different assumptions of tropospheric HCl loss (see Chapter 2), it is not clear why these two models should differ for other chemical species and their relative partitioning. Figures 6.16 and 6.17 also show comparisons of CCM climatologies of $NO_2$ and BrO, averaged over 24-hours in the TM2z output, with satellite observations made at a fixed local time but converted to a 24-hour mean using a photochemical model (B. M. Sinnhuber, personal communication, 2009). Despite this approximation the comparisons indicate whether the models capture the observed seasonal cycles in these species. (A detailed evaluation of the radicals is provided in Section 6.3.2). For $NO_2$ models do capture the shape of the seasonal cycle, with ULAQ spanning the models and observations at the high end and SOCOL at the low end. For BrO the comparison is complicated by the fact that the REF-B1 scenario is defined without bromine from very short-lived species. Therefore, the models should under-estimate stratospheric $Br_y$ by around 5 pptv (WMO, 2007), although

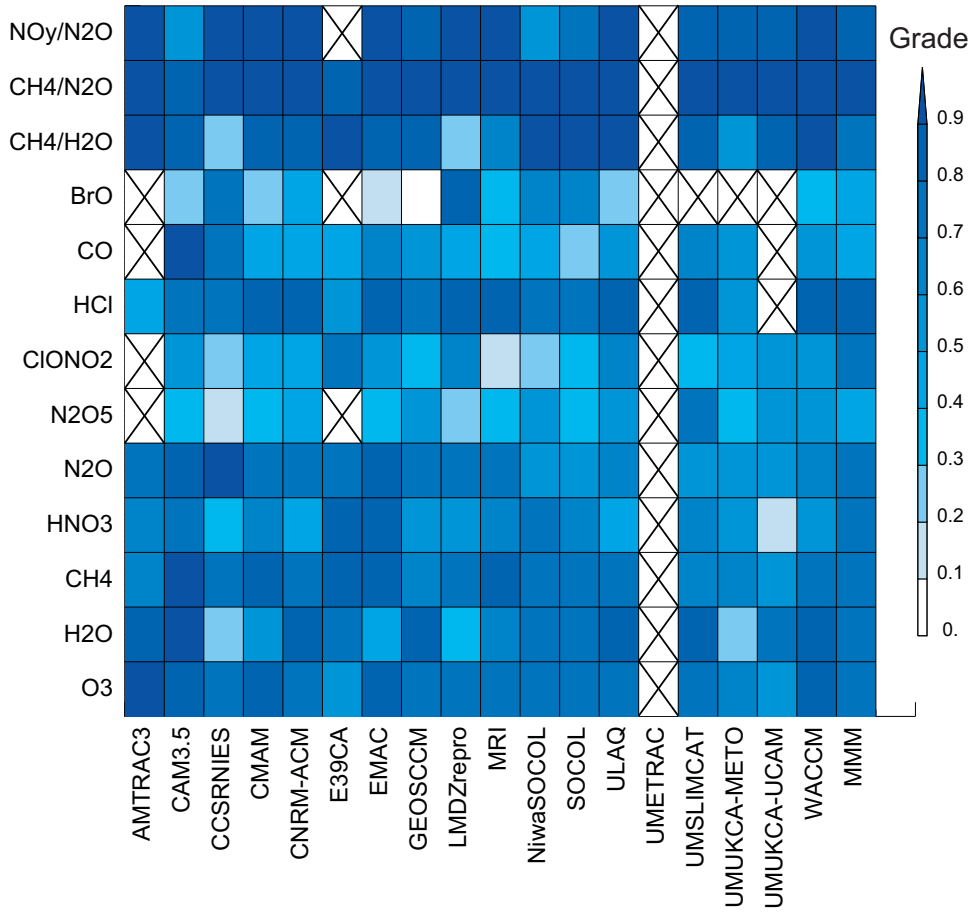


**Figure 6.15:** Grading plot for 18 CCMs (although no grades for UMETRAC) for tracer-tracer correlations, comparisons with the mean annual cycle (at 1 hPa and 50 hPa) and mean vertical profiles of a range of tracers in 3 latitude bands. Also shown is the score of the multi-model mean (MMM).

many CCMs included extra bromine (see below). The figure shows that the CCMs have a wide range in average BrO. Many models under-estimate the observed 24-hour mean values.

The comparison between the CCMs and satellite data for the selected altitudes and latitude regions was quantified as follows:

1. For every month, we calculated absolute differences (model-observation) on two levels, 1 hPa and 50 hPa.
2. If this difference is more than 3x the observational mean we assign a score = 0.1.
3. If this difference is more than 2x the observational mean, but less than 3x, we assign a score = 0.2.
4. If this difference is less than the observational mean we calculate the score using Equation (6.1) assuming all the observational data have 10% error ($\sigma$) and $n$ = 3 (scaling factor).

We then average all the scores for all the months and latitude bands for 50 hPa and 1 hPa. Multi-model means are calculated by summing monthly mean values from all the CCMs and then calculating the differences between multi-model mean - observational mean and then following steps (2) – (4).

Figure 6.15 shows the results of the grading for the comparison with the satellite climatologies. There are some tests for which all of the models tend to score lower, *e.g.*, $ClONO_2$ and $N_2O_5$, which may indicate some bias in the observations.

### 6.3.3.3 Long-term variations

Long-term observations provide data to test another component of the chemical models. Multi-annual satellite missions provide global altitude-resolved observations of trace gases from the early 1990s. In addition, observations from the Network for the Detection of Atmospheric Composition Change (NDACC) provide long-term data sets at certain ground-based sites which extend from the 1980s or 1990s to the present day. These data can be used to check the modelled variability (*e.g.*, annual cycle, volcanic influence) of key species which control stratospheric ozone.

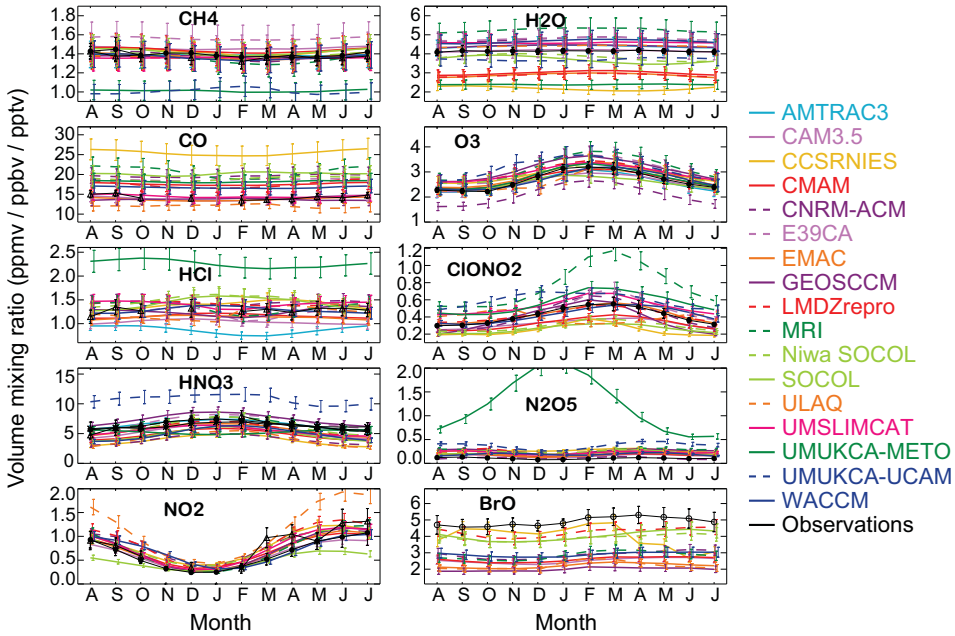


**Figure 6.16:** Mean annual cycle for 30°N-60°N at 50 hPa for modelled $CH_4$ (ppmv), $H_2O$ (ppmv), CO (ppbv), $O_3$ (ppmv), HCl (ppbv), $ClONO_2$ (ppbv), $HNO_3$ (ppbv), $N_2O_5$ (ppbv), $NO_2$ (ppbv) and BrO (pptv). The CCM data is taken from the T2Mz files (2000-2004, except for the E39CA model 1996-2000). Also shown are corresponding satellite observations from MIPAS ($CH_4$, $H_2O$, $O_3$, $ClONO_2$, $HNO_3$, $N_2O_5$, $NO_2$; filled circles), ACE ($NO_2$, $HNO_3$, CO, HCl; triangles), ODIN ($HNO_3$, crosses) and SCIAMACHY (BrO; open circles). The error bars are the standard deviations in the monthly-mean values (except for ACE data).

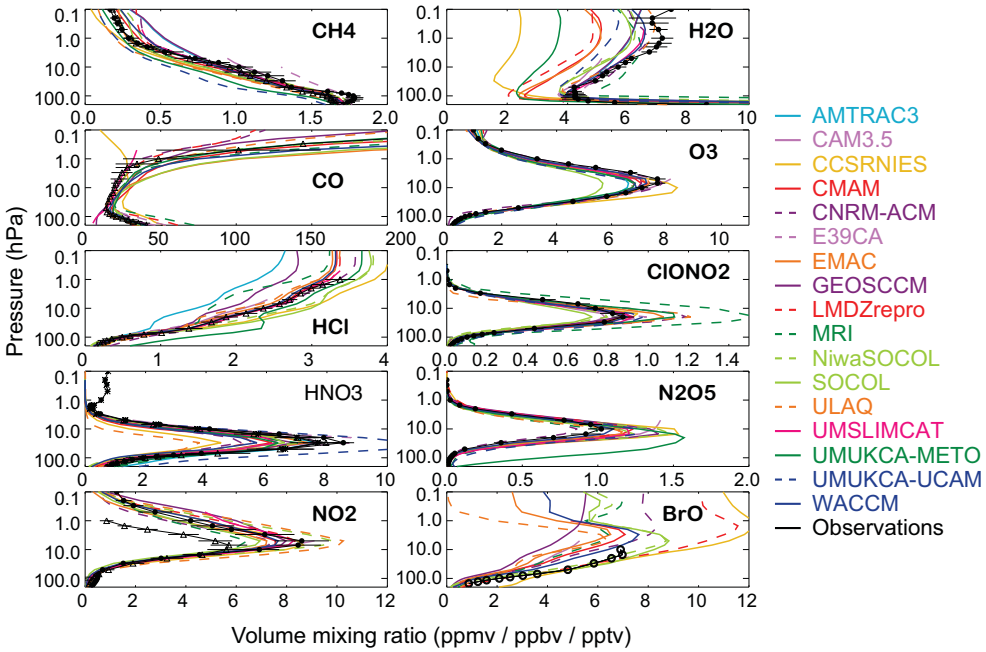


**Figure 6.17:** Mean profiles for 30°S-60°S for modelled $CH_4$ (ppmv), $H_2O$ (ppmv), CO (ppbv), $O_3$ (ppmv), HCl (ppbv), $ClONO_2$ (ppbv), $HNO_3$ (ppbv), $N_2O_5$ (ppbv), $NO_2$ (ppbv) and BrO (pptv). The CCM data is taken from the T2Mz files (2000-2004, except for the E39CA model 1996-2000). Also shown are corresponding satellite observations from MIPAS ($CH_4$, $H_2O$, $O_3$, $ClONO_2$, $HNO_3$, $N_2O_5$, $NO_2$; filled circles), ACE ($NO_2$, $HNO_3$, CO, HCl; triangles), ODIN ($HNO_3$, crosses) and SCIAMACHY (BrO; open circles). The error bars are the standard deviations in the annual mean values (except for ACE data).

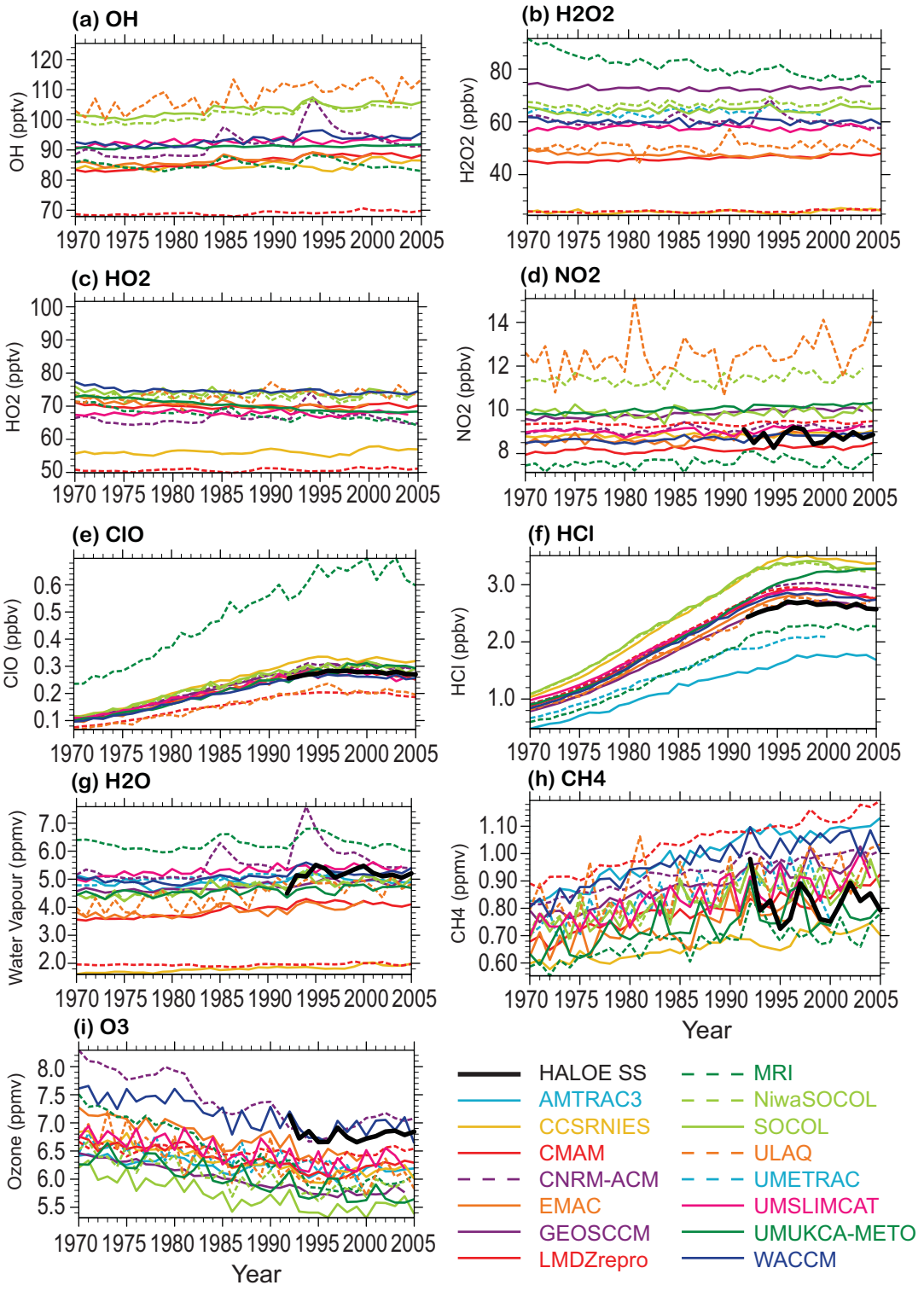


**Figure 6.18:** Time series of modelled zonal-mean (24-hour mean) trace gas abundance in the tropical upper stratosphere (3 hPa, 5°S-5°N) for (a) OH (pptv), (b) $H_2O_2$ (pptv), (c) $HO_2$ (pptv), (d) $NO_2$ (ppbv), (e) ClO (ppbv), (f) HCl (ppbv), (g) $H_2O$ (ppmv), (h) $CH_4$ (ppmv) and (i) $O_3$ (ppmv). Also shown (1991 onwards) are HALOE satellite observations for $NO_2$, HCl, $H_2O$, $CH_4$ and $O_3$. In panel (d) the twilight HALOE observations are converted to a 24-hour mean by using the ratio $NO_2/NO_x$ from the EMAC model. Panel (e) also shows ClO derived from HALOE HCl by using the ratio of HCl/ClO from the EMAC model.

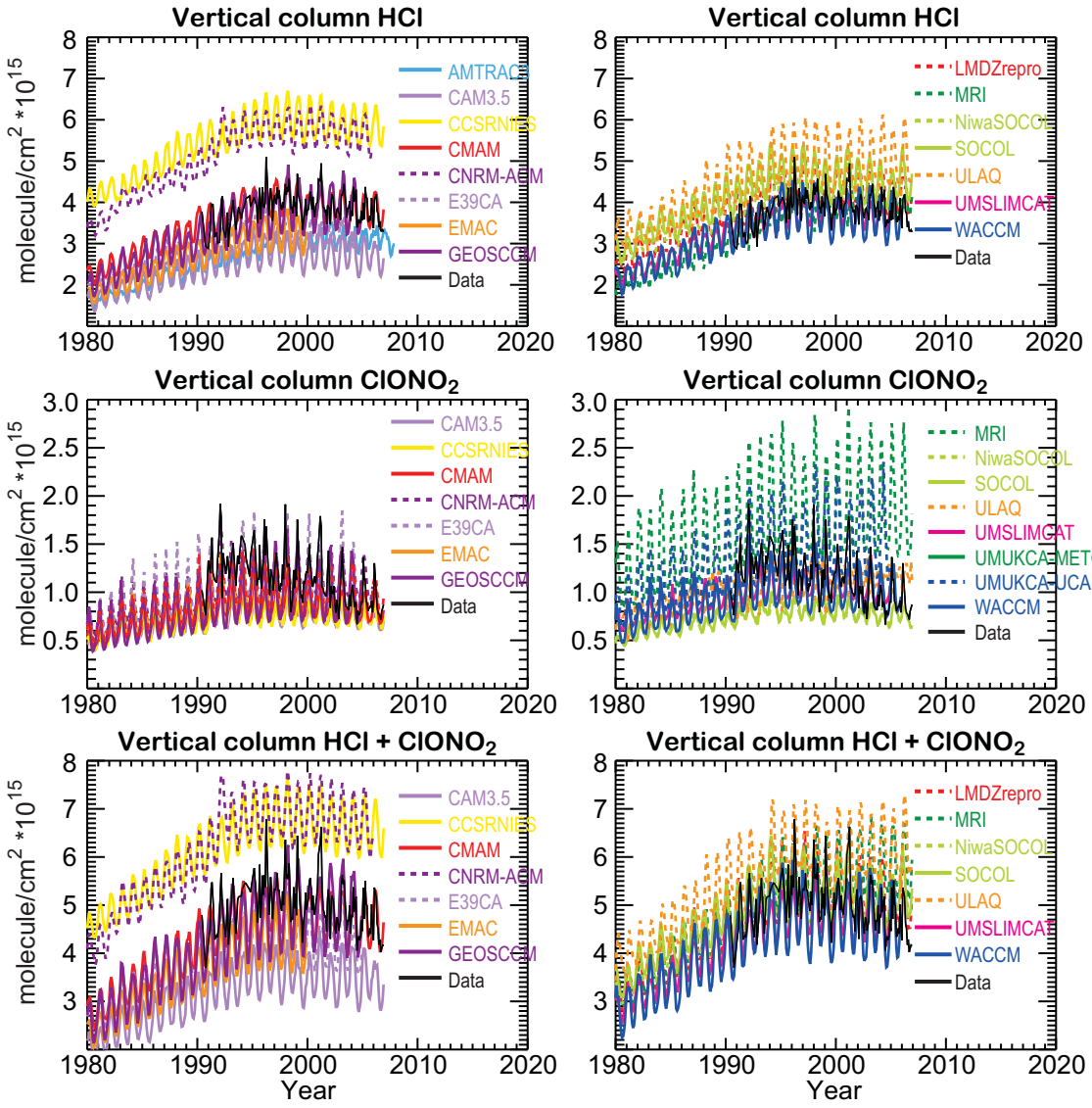


**Figure 6.19:** Comparison of observed column abundances (molecules $cm^{-2}$) of HCl, $ClONO_2$, and HCl + $ClONO_2$ at Jungfraujoch (45°N) with output from REF-B1 simulations.

**Figure 6.18** shows modelled mean tracer variations in the tropical upper stratosphere (3 hPa) for selected species. The model zonal mean output was averaged between 5°S and 5°N. Also shown are observations from the HALOE instrument starting in 1991. For $H_2O$ this figure again shows the variation between the CCMs. The majority of models do agree fairly well with the observed 5 ppmv at this altitude. The CCSRNIES and LMDZrepro models, however, are very dry (only 2 ppmv $H_2O$ at this altitude), while EMAC and CMAM are slightly dry. In contrast, the MRI model is too moist (over 6 ppmv). CNRM-ACM is exceptional among the models for showing significant enhancements in $H_2O$ around 1985 and 1994, following the volcanic eruptions. For OH and $HO_2$ the models tend to show similar values with little interannual variability, though the spread in OH is larger. The very dry models (CCSRNIES and LMDZrepro) show the smallest values of $HO_2$, but only LMDZrepro has correspondingly low OH. ULAQ, SOCOL and NiwaSOCOL have the largest values of OH. For $CH_4$ the models show a lot of model-model differences (*e.g.*, due to different circulation rates) and there is a large degree of interannual variability, presumably due to the equatorial QBO. For $NO_2$, ULAQ (which also has large interannual variability) and NiwaSOCOL show relatively large values. For HCl the CCMs reproduce the increasing trend through to 1997, followed by the turn-over and decrease. However, the AMTRAC3 model, for which we cannot assess the source gas loading and distribution, has significantly lower HCl than HALOE. The models with the highest HCl (*i.e.*, over 3 ppmv at this altitude in the early 2000s – UMUKCA-METO, CCSRNIES, SOCOL, NiwaSOCOL) are those that have spurious excess chlorine

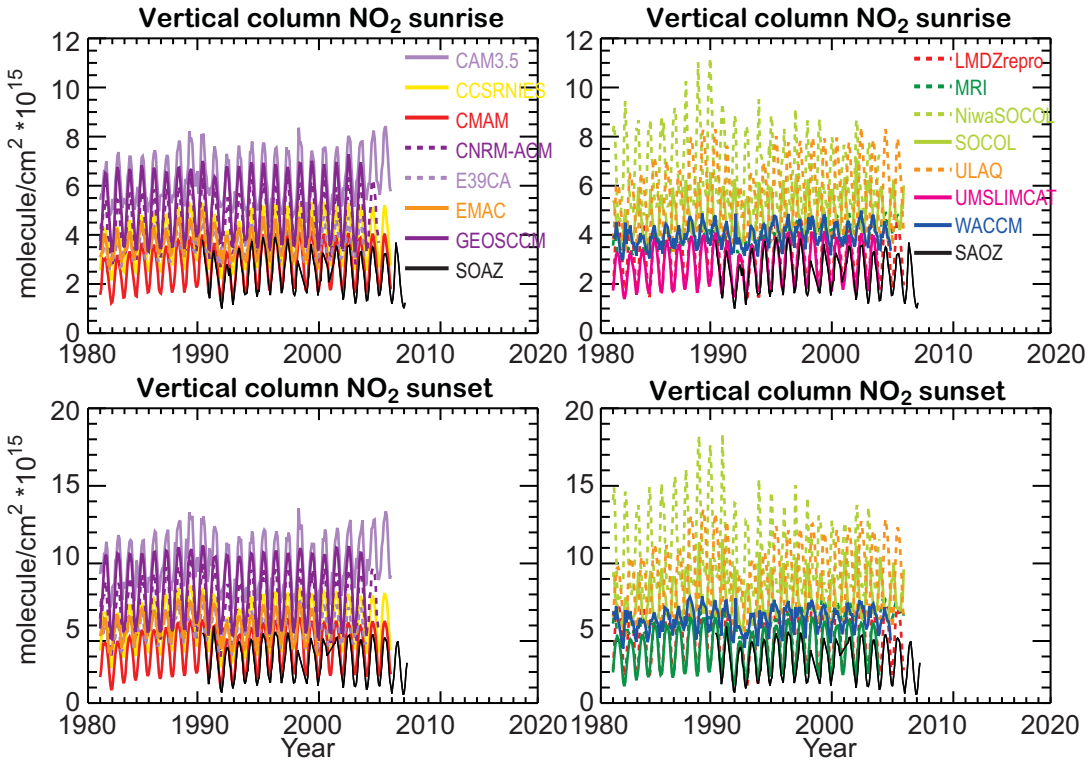


**Figure 6.20:** Comparison of observed column abundances (molecules $cm^{-2}$) of $NO_2$ at Jungfraujoch (45°N) for (a) sunrise and (b) sunset observations with output from REF-B1 simulations. The modelled 24-hour mean output (from zonal-mean files) have been converted to sunrise and sunset values using ratios of sunrise and sunset columns to 24-hour mean columns from the SLIMCAT 3D chemical transport model.

(see discussion of Figure 6.21 below). For ClO a notable outlier is the MRI model, which has significantly too much ClO. This will be due to the omission in this model of the $ClO + OH \rightarrow HCl + O_2$ reaction (see Table 6S.2) which is important for the partitioning of inorganic chlorine ($Cl_y$) at this altitude. This means that the MRI model will have a much larger sensitivity of ozone to $Cl_y$ increases in the upper stratosphere. For $O_3$ itself, all of the models tend to produce a decrease through the 1970s and 1980s, although there is a spread of values in the models. This spread, in the region where ozone is photochemically controlled, will be due to differences in the abundance of radicals which destroy ozone at this altitude, differences in the production rate from $O_2$ photolysis, and differences in model temperatures. Further comparisons of $HO_2$, $NO_2$ and ClO at lower altitudes are provided in the supplementary material in Figure 6S.10.

**Figure 6.19** shows observations of column HCl, $ClONO_2$, and their sum, at the Jungfraujoch station (45°N) along with CCM results for 45°N (from zonally averaged output). These two species are the main reservoirs for stratospheric inorganic chlorine. The observations show an increase in column $HCl + ClONO_2$ until about 1998 followed by a decrease. The stratospheric trend in inorganic chlorine is expected to follow the tropospheric loading of organic chlorine (see Chapter 2) with a lag due to stratospheric transport time scales. Interestingly, at this station $ClONO_2$ appears to be decreasing relatively faster than HCl over the past decade in the observations, whereas the models do not show such a marked difference. Further analysis of this apparent discrepancy is not possible here. There is a large variation in the magnitude of the column $HCl + ClONO_2$ predicted by the models. The CCSRNIES and CNRM-ACM models predict much larger columns (by about 40%) than the observations. This will be due, at least in part, to the larger chlorine loading in these models although column comparisons also depend sensitively on the shape of the model profiles in the lower stratosphere (where higher pressures mean a potentially large contribution to the column). In contrast, the CAM3.5 model under-estimates column $HCl + ClONO_2$. Despite these differences in magnitude, most models predict a similar long-term behaviour with a peak in inorganic chlorine in the late 1990s. The ULAQ and MRI models, however, maintain high chlorine until the end of the REF-B1 run. There are further differences between the models in terms of the partitioning of HCl and $ClONO_2$. The MRI and UMUKCA-UCAM models compare well for HCl but overestimate $ClONO_2$ while SOCOL and NiwaSOCOL under-estimate this species.

**Figure 6.20** compares column $NO_2$ observed at

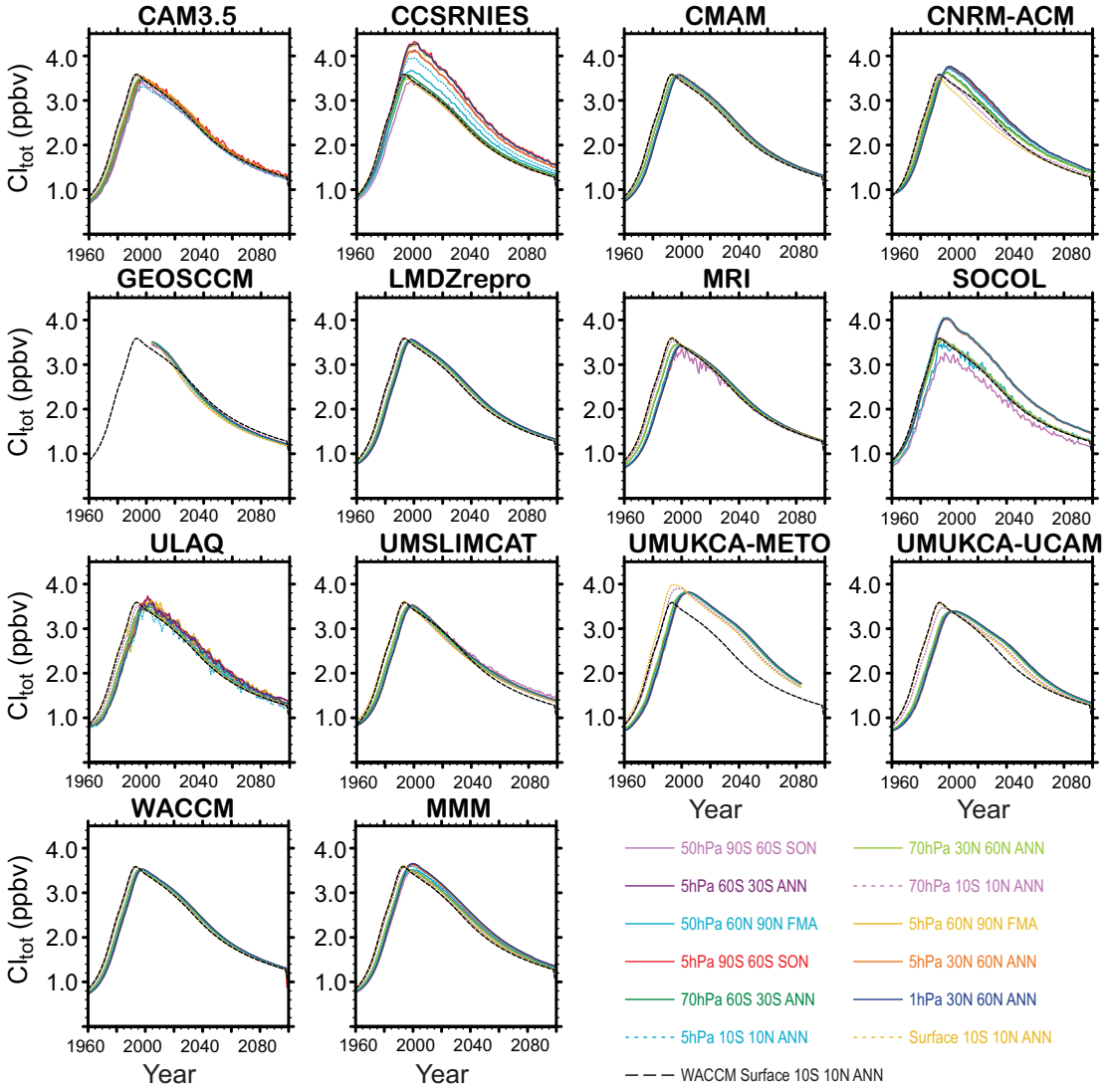


**Figure 6.21:** Time series of total chlorine volume mixing ratio (sum of all inorganic and organic chlorine tracers) (ppbv) from 1960 to 2100 from 13 REF-B2 CCM simulations and the multi-model mean. A selection of averages within different latitude bands and at different altitudes are plotted. For reference, each panel also includes the total chlorine curve from the WACCM model at the surface (black dashed line).

Jungfraujoch with the available CCM output. As $NO_2$, which is a key ozone-destroying radical, has a strong diurnal cycle the CCM zonal mean (*i.e.*, 24-hour mean over different local times and different longitudes) output had to be converted to the time of the observations (sunrise and sunset) using output from the SLIMCAT chemical transport model. Note that this conversion is not necessarily self-consistent because a different model is used in the conversion of daily means into sunset/sunrise values. Again, there is a large variation in the magnitude of the column predicted by the models. While some models agree quite well, many other models overestimate the observations. In particular, column $NO_2$ derived from CAM3.5. GEOSCCM, CNRM-ACM, NiwaSOCOL, ULAQ and SOCOL are up to a factor 2 larger than observations. WACCM appears to severely under-estimate the magnitude of the $NO_2$ annual cycle. The eruption of Mt Pinatubo in 1991 led to a decrease in column $NO_2$ followed by an increase through the mid-1990s. Since almost all the models use prescribed sulphate surface area density, they are able to capture this long-term variation. This is not the case for GEOSCCM which was run with constant aerosol. The long-term trend in $NO_y$ and hence in $NO_2$ (expected from the trend in its source gas, $N_2O$) is too small to be visible in the time series of observations and model calculations.

We now analyse results from the REF-B2 simulations from 1960 to 2100. The aim here is not to evaluate against observations but to check the CCMs for internal consistency in their chemical schemes and to verify that the models have used the recommended source gas bound-

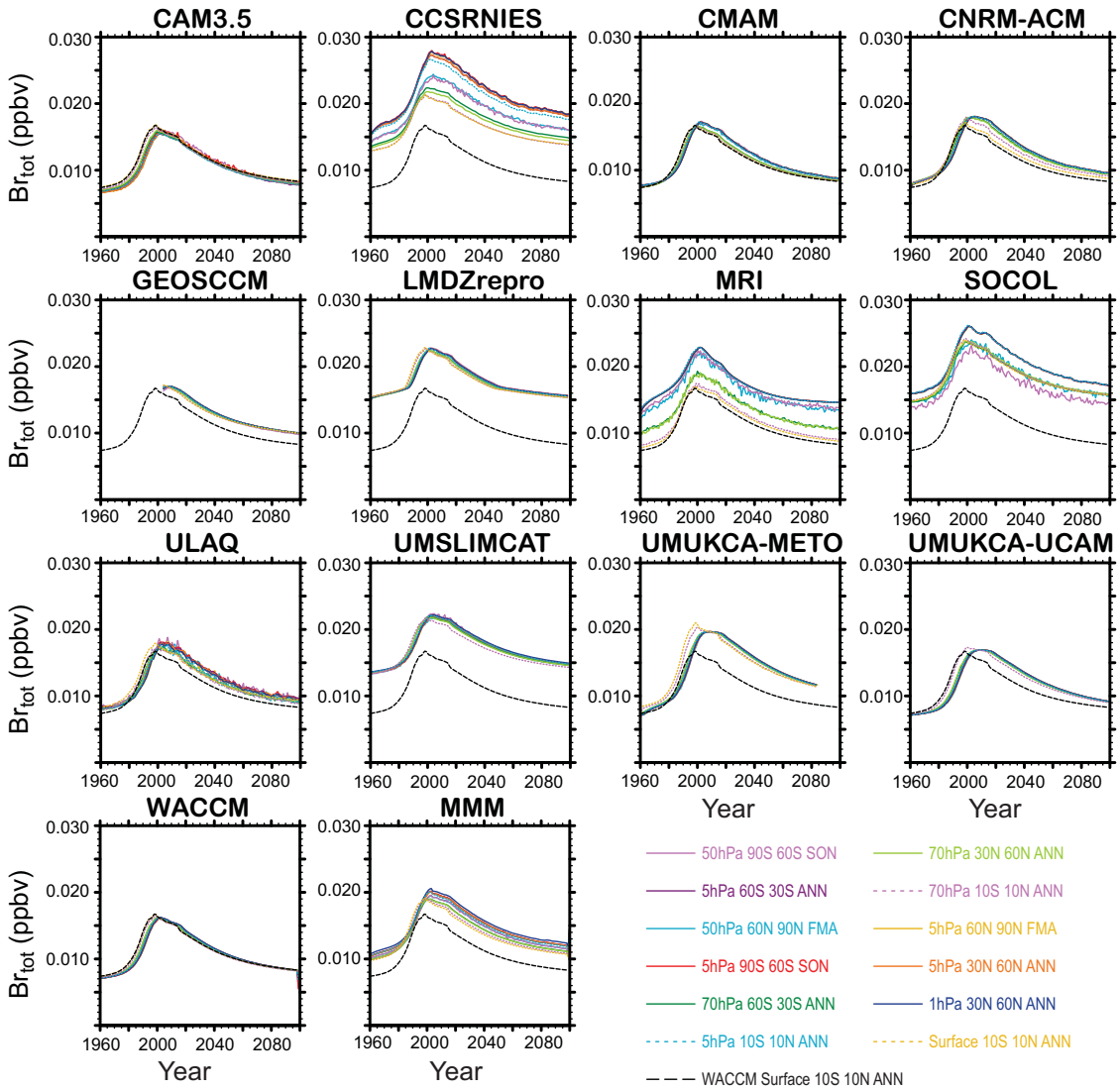


**Figure 6.22:** As Figure 6.21 but for total bromine mixing ratio (ppbv).

ary conditions. **Figures 6.21** and **6.22** plot the time series of total chlorine ($Cl_{tot}$) and total bromine ($Br_{tot}$), respectively, from the available models in selected latitude bins and at selected altitudes. These model curves have been constructed by summing all of the organic and inorganic chlorine or bromine species in the model. Many models employ a lumping scheme for minor halocarbons (see Chapter 2), but in these cases the contribution of chlorine and bromine is added to the tracers that are carried, and so this will not affect the total abundance. Therefore, ideally the total chlorine and bromine curves for all models at the surface should be consistent with the specified scenario. For any model, the total chlorine and bromine curves at high altitudes in the stratosphere should mimic the surface (tropospheric) variation with a delay and smoothing reflecting the model mean age-of-air (see Chapter 5) and atmospheric mixing. Similar plots for just organic chlorine and bromine are provided in the Supplementary Material, Figures 6S.11 and 6S.12.

For total chlorine (Figure 6.21) many models show the expected behaviour but there are some notable deviations. The models which perform well are CAM3.5, CMAM, LMDZrepro, UMSLIMCAT, and WACCM. These models show a compact set of curves which are very similar at all locations with a slight delay between the tropospheric values and higher altitudes. The GEOSCCM and UMUKCA-UCAM models also appear intrinsically well behaved but the models' total chlorine scenarios appear to differ from that specified in the forcing data. MRI, and to a greater extent ULAQ, show fairly good consistency between different model levels except that in some locations total chlorine variations appear to be more noisy. Figure 6.21 also reveals that some models have stratospheric $Cl_{tot}$ variations which are inconsistent with the specified tropospheric forcing. In the CCSRNIES, model the tropospheric $Cl_{tot}$ follows the specified scenario. However, on going to higher

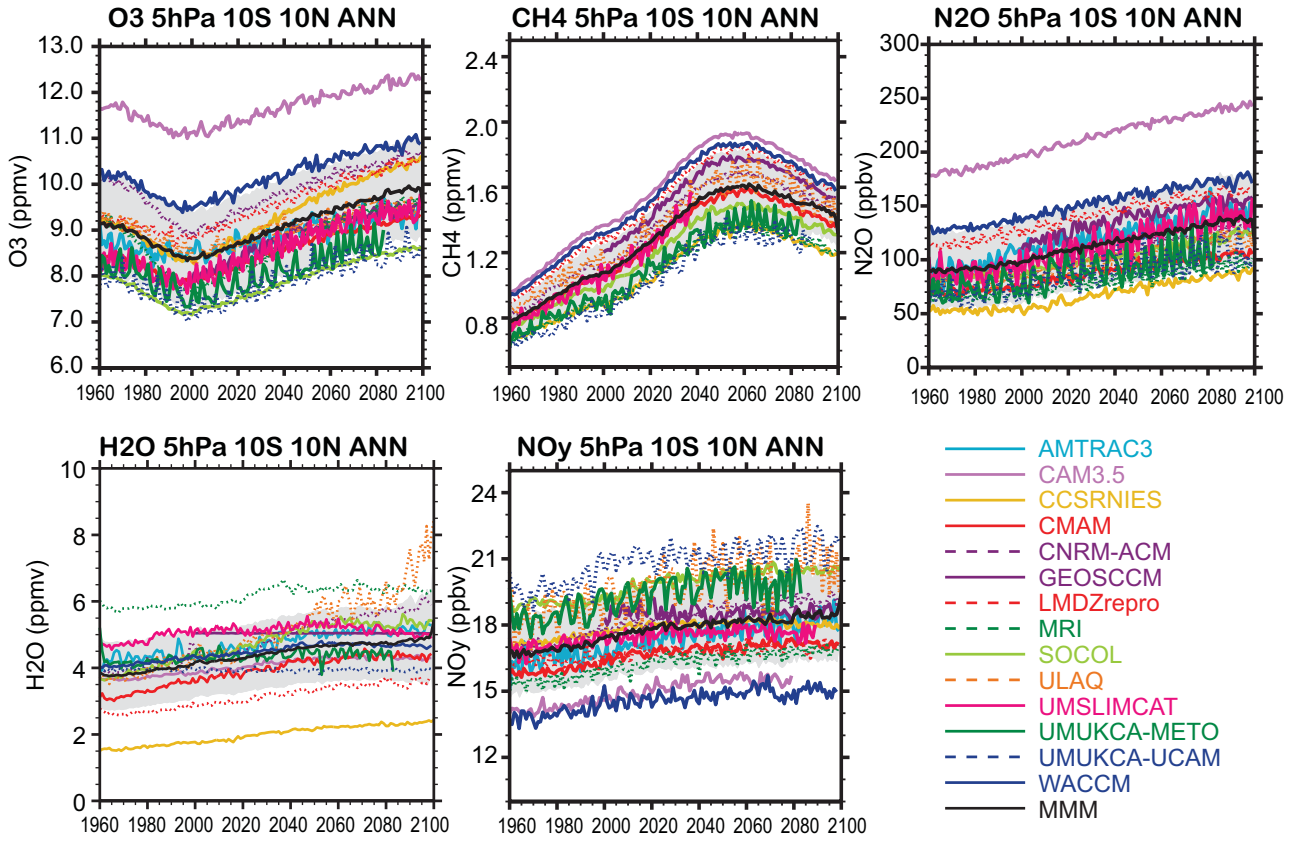


**Figure 6.23:** Time series of $O_3$ (ppmv), $CH_4$ (ppmv), $N_2O$ (ppbv), $H_2O$ (ppmv) and $NO_y$ (ppbv) annually averaged between 10°S and 10°N at 5 hPa from REF-B2 runs of 14 CCMs and the multi-model mean.

altitudes $Cl_{tot}$ increases until it peaks at over 4 ppbv at 5 hPa around 2000. Evidently this model does not conserve the total chlorine mixing ratio. This effect is also seen, but to a much smaller extent, in CNRM-ACM. SOCOL shows a similar behaviour to CCSRNIES but in this case there is an apparent separation between the lower curves (50 hPa, 70 hPa) which follow the specified $Cl_{tot}$ scenario and the higher curves (1hpa, 5 hPa) which have unrealistically high $Cl_{tot}$. The UMUKCA-METO model has $Cl_{tot}$ that is too high because of the reported mistreatment of tropospheric removal of species, in this case HCl (see Chapter 2). Otherwise UMUKCA-METO behaves similarly to UMUKCA-UCAM. Finally, we could not plot $Cl_{tot}$ from AMTRAC because it does not carry organic halocarbons. We analysed total inorganic chlorine ($Cl_y$) from AMTRAC and noted that even in the upper stratosphere $Cl_y$ was significantly less than $Cl_{tot}$ from other realistic models (see also comparison with HALOE HCl in Figure 6.18). Therefore, it seems likely that the AMTRAC treatment of chlorine causes an under-estimate in total chlorine.

Figure 6.22 shows the evolution of model $Br_{tot}$. In general for bromine the CCMs show more differences compared to the planned scenario than for chlorine. The specifications for the CCMVal runs only considered long-lived bromine source gases. Therefore, model tropospheric $Br_{tot}$ should have peak at around 16 pptv just before the year 2000. The models CAM3.5, CMAM and WACCM follow this scenario with consistent variations in the stratosphere. Other models appear to conserve bromine but have been run with different scenarios: UMSLIMCAT and LMDZrepro assumed an extra ~6 pptv bromine from short-lived sources; UMUKCA-UCAM has larger $Br_{tot}$ after 2000, as does ULAQ and GEOSCCM. CCSRNIES includes a short-lived source of bromine (bromoform) hence its tropospheric $Br_{tot}$ variation peaks around 21 pptv. However, bromine increases at higher levels in a similar way to the model's $Cl_{tot}$ indicating conservation problems. SOCOL also appears to include additional bromine sources but also has mid-stratospheric $Br_{tot}$ larger than expected, again similar to $Cl_{tot}$. UMUKCA-METO has larger bromine than UMUKCA-UCAM, suggesting that the tropospheric washout problem (Chapter 2) is also affecting the abundance of total bromine. The MRI model generally performed well for $Cl_{tot}$ but show an increase in $Br_{tot}$ with altitude.

**Figure 6.23** shows the evolution of $O_3$, $CH_4$, $N_2O$, $H_2O$ and $NO_y$ at 5 hPa in the tropics from the REF-B2 runs. **Figures 6.24** and **6.25** are similar plots for 70 hPa

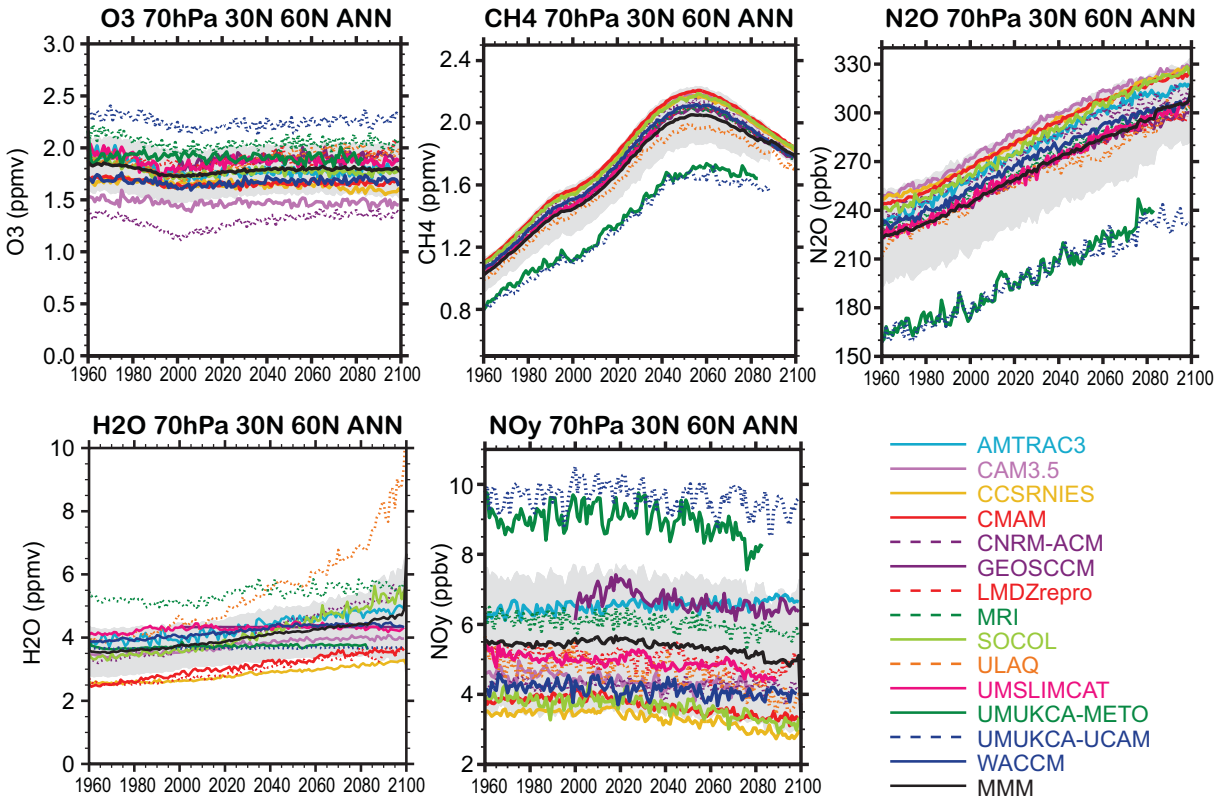


**Figure 6.24:** As Figure 6.23 but for an annual average between 30°N and 60°N at 70 hPa.

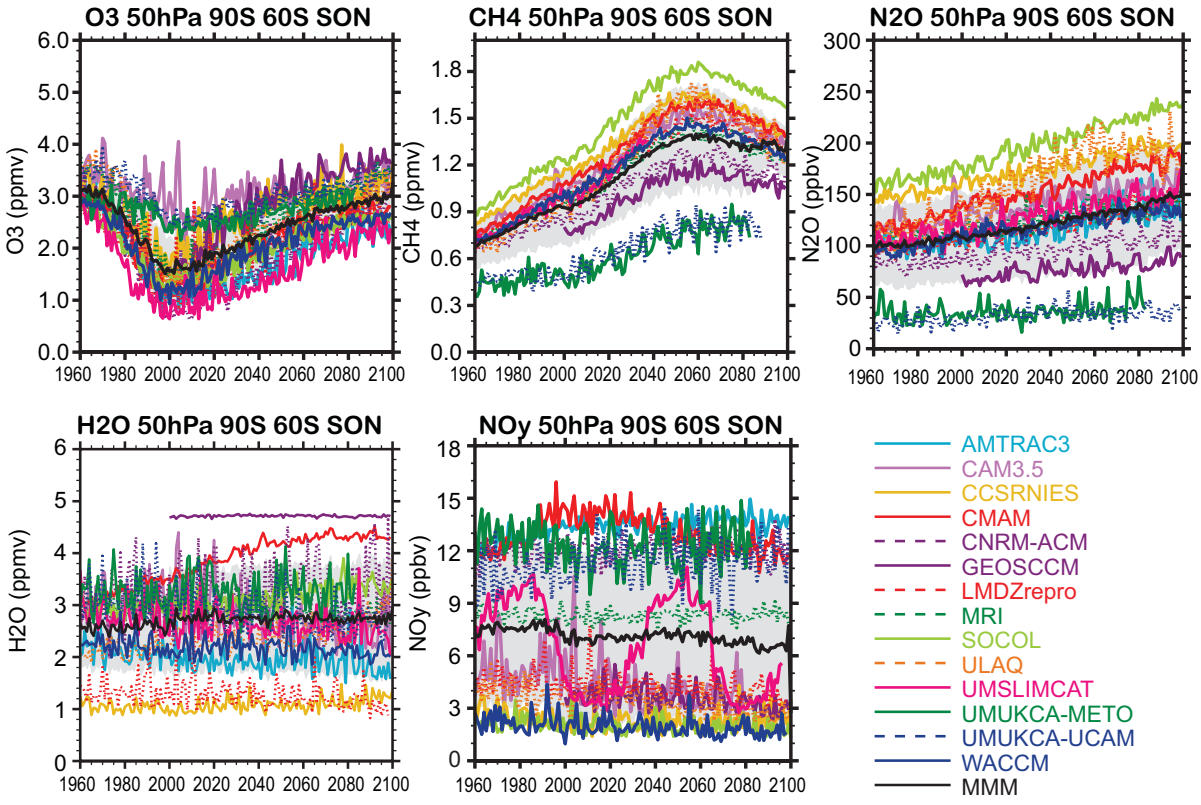


**Figure 6.25:** As Figure 6.23 but for a September–November average between 90°S and 60°S at 50 hPa.

in the mid-latitudes and 50 hPa in the polar region, respectively. The modelled distribution of long-lived tracers will be affected by both transport and chemistry. Chapter 5 contains a detailed evaluation of transport in the models and will not be repeated here. Clearly a lot of the variations in, for example, tropical mid-stratosphere $N_2O$ will be due to differences in the strength of the model circulation. Other differences will be due to chemistry, *e.g.*, photolysis loss rates (see Section 6.3.1). In this section we show these long-term variations to provide an overview of the long-term variations in the sources of $NO_x$ and $HO_x$ radicals, which, in conjunction with halogens, will be driving ozone changes (see Chapters 8 and 9). Overall, the models show similar variations in $CH_4$ and $N_2O$, both of which are specified as tropospheric surface boundary conditions. At 5 hPa CAM3.5 is an outlier but this is near the model's top boundary. At mid- to high latitudes, the two UMUKCA models are significantly lower but this will be a consequence of the slow stratospheric circulation in this model (Chapter 5). The model spread in $NO_y$, which is derived from $N_2O$, is at least as large as the source gas. High $N_2O$ will correlate with low $NO_y$ and *vice versa*. In the polar region in winter/spring (*e.g.*, Figure 6.25) there is also the additional variability caused by denitrification. Compared to other source gases, there are larger variations (and differences in sign) in the modelled trends in $H_2O$, which depends both on the input to the stratosphere and production from methane oxidation. The CCSRNIES and LMDZrepro models are relatively dry, while the MRI model is moist. GEOSCCM uses constant water vapour in the stratosphere (note: this was a run time error and the simulation is being repeated). A number of models produce an increasing trend in $H_2O$ towards the later decades on this century, notably ULAQ at low and mid-latitudes and CMAM in the polar region.

## 6.3.4 Evaluation of Polar Chemistry

### 6.3.4.1 Evolution of gas-phase $HNO_3$, $H_2O$, and HCl

In this section we evaluate aspects of polar winter/spring chemical processing in the southern hemisphere (SH), by comparing the time evolution of CCM lower stratospheric abundances to global observations (from mid-2004 through mid-2009) by the Microwave Limb Sounder aboard the Aura satellite. The processes involved include denitrification (or at least a decrease in gaseous $HNO_3$) as a result of heterogeneous reactions that occur on PSCs when temperatures in the lower stratosphere polar vortex dip below about 195 K, as well as dehydration (or at least a decrease in gaseous $H_2O$) and chlorine activation (the sunlight-driven release of active chlorine, following a decrease in the HCl and $ClONO_2$ reservoir abundances *via* heterogeneous reactions). We investigate polar changes in $HNO_3$, $H_2O$, and HCl, in order to assess how models compare to each other and to observations. We use a decrease in HCl as an indication of chlorine activation, rather than an increase in ClO, because of the added complications that ClO poses in terms of time of day sampling and comparisons to model values that are more representative of 24-hr averages (and therefore significantly lower than midday values). Model grades are provided as a quantitative guide to the MLS comparison, and to illustrate the range of variations between the models. We also comment briefly on the extent of model variations in space and time, for "outliers" in particular, in comparison to the "typical" behaviour from observations (and models).

In order to investigate such complex processes in free-running models, which are likely to vary significantly in their representation and parameterisation of heterogeneous chemistry and related polar processing and dynamics, and without unduly focusing on a specific year, we have compared climatologies of volume mixing ratio (VMR) *versus* potential temperature ($\theta$) as a function of equivalent latitude (EqL). The model values were obtained from REF-B1 simulations, typically from 1950 to 2006 (although the exact start and end dates vary between models, with some models ending in 2004 and some in 2006). The models were all converted from gridded 10-day instantaneous results to mean profiles on a vertical $\theta$-grid, in EqL bins spaced every 2.5°; 15 of 18 total CCMs provided the necessary results for analysis. The Aura MLS data were also transferred to this coordinate system (more appropriate for analyses of polar winter processes) by using UKMO analysis files and related "Derived Meteorological Products" from the work of Manney *et al*. (2007). Five years of MLS data (from August, 2004 through July, 2009) were used to construct the climatological averages. These files were all produced in the same format (netCDF), for ease of use. The last 5 years of each model run were used to compare to the MLS 5-year climatological profiles. Based on our analysis of model variability (from year to year), using 10-15 years rather than 5 years for the model climatologies is not expected to generally change the main results, as model variability is typically fairly small compared to average model values (or model changes during polar winter/spring). Relevant references for the Aura MLS data include Waters *et al*. (2006) for a description of the limb emission microwave measurement technique, as well as detailed validation papers for the species mentioned here (and for MLS version 2.2 retrievals), namely Santee *et al*. (2007) for $HNO_3$, Froidevaux *et al*. (2008) for HCl, and Lambert *et al*. (2007) for stratospheric $H_2O$.

**Figure 6.26** shows the climatological average evolution of Aura MLS $HNO_3$ profiles (on a $\theta$-grid) between mid-May and mid-October, for 4 EqL ranges centred at

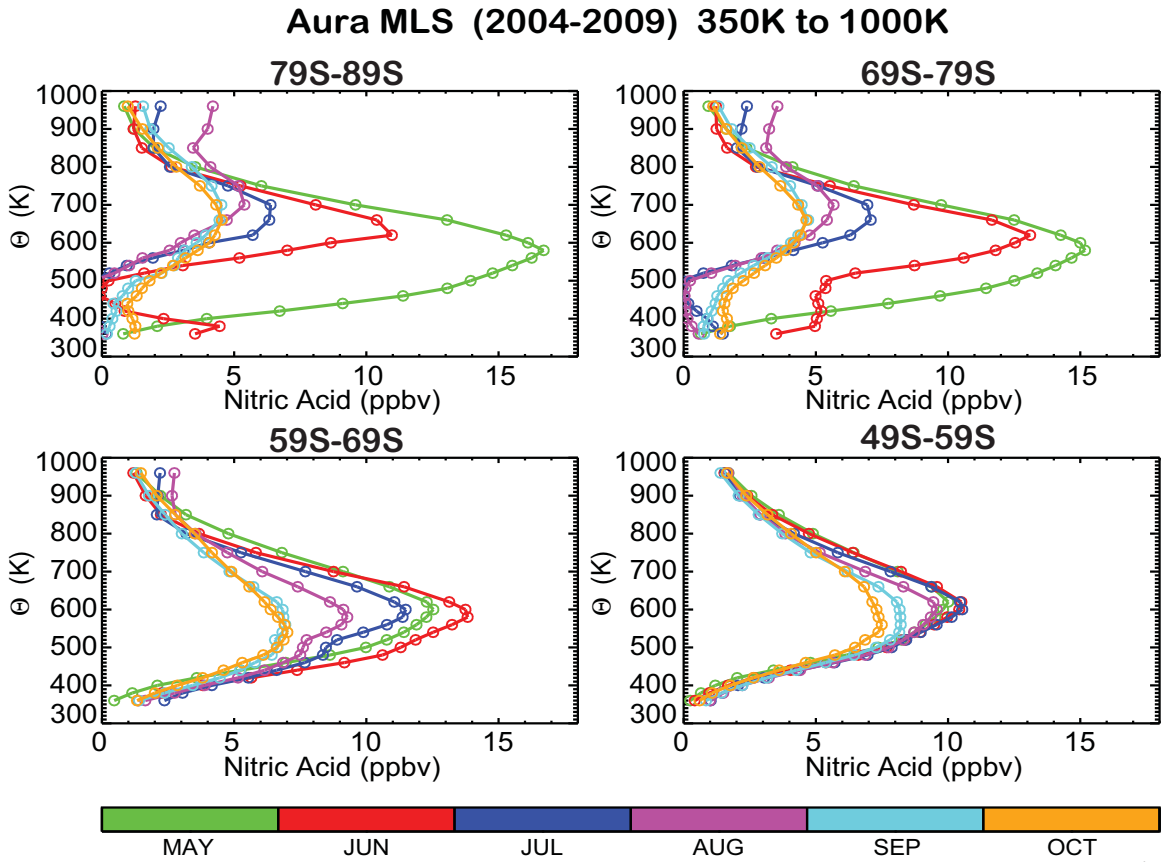


**Figure 6.26:** Southern hemisphere profiles of $HNO_3$ versus θ from Aura MLS at mid-month (on the 15th day of each month shown in colour bar), from May through October, based on a 5-year MLS climatology (mid-2004 to mid-2009). Profiles are averaged over the EqL ranges shown above each panel.

about 85°S, 75°S, 65°S, and 55°S. **Figure 6.27** shows similar profile distributions, but only for the southernmost EqL bin, and includes all the available CCM climatological monthly changes, as well as a multi-model mean result (labelled "MMM"). The mid-month values are obtained by using the day closest to the 15th of each month; while this falls on the 15th day for MLS (daily) data, this will not be exactly the case for the model climatologies (models usually provided output every ten days). Most of the decreases in MLS $HNO_3$ are seen to occur for θ < 800 K, with the lowest $HNO_3$ values occurring between July and September for θ < 550 K in the two southernmost EqL bins. A more rapid/extensive lower stratospheric nitric acid decrease is observed by Aura MLS than in most of the models, although some models show decreases in $HNO_3$ at higher altitudes (θ) than observed. To summarize the evolution of lower stratospheric CCM $HNO_3$ distributions over the high SH latitudes, **Figure 6.28** shows a comparison of the various model (5-year) climatological monthly changes in $HNO_3$ (relative to mid-May) over the 350 K-600 K θ range *versus* the MLS climatology in four EqL bins.

Grades indicating the quality of the model fits to the data over this time period are obtained by using Equation (6.1), evaluating the average absolute separation (over $N$ months, with $N = 5$ here) between model ($\mu^i_{model}$) and observed ($\mu^i_{obs}$) climatological values, divided by a measure of uncertainty (or variability) in the data, so that the grade is

$$g = 1 - \frac{1}{N}\sum_i \frac{\mu^i_{model} - \mu^i_{obs}}{n\sigma} . \qquad (6.5)$$

In order to check such fits, a value for $n\sigma$ in the above equation needs to be provided, with $n = 3$ used in previous recommendations (Waugh and Eyring, 2008). Given the fairly large spread of models about the data in Figure 6.28 for $HNO_3$ (and to some extent for other species discussed below), we would obtain low-grade values (or negative grades) for many of the models if $\sigma$ values corresponding only to data variability or (especially) knowledge were used. Instead, we have arrived at grades that provide a range of values between 0 and 1, so that model differences can be fairly well discerned. Therefore, this is more a *relative* indication of model fits to the data than a rigorous statistical test. Some changes to the values of $n\sigma$ have been explored (*e.g.*, variations by a factor of 2 or more). While the absolute grades can certainly be affected (by several tenths), the main results regarding the best or poorest fit-

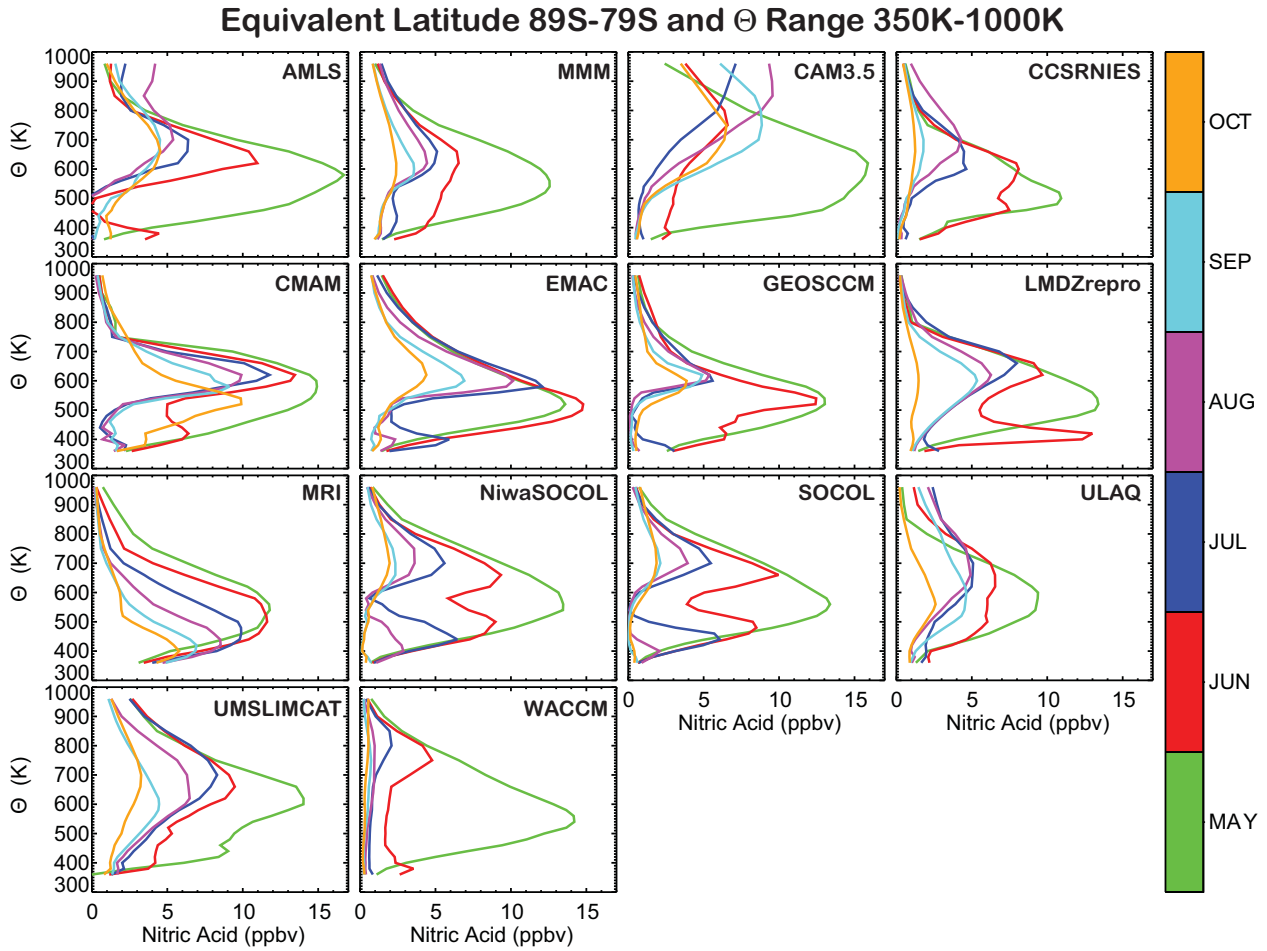


**Figure 6.27:** CCM climatological profiles of $HNO_3$ from mid-May through mid-October (same colour bar as in Figure 6.26) for 12 CCMs and multi-model mean (MMM). Only the southernmost EqL bin from Figure 6.26 is displayed here.

ting models do not change much, and this will be the main focus of our discussion. For reference, values of nσ used in this study are 5 ppbv, 1.5 ppmv, 1 ppbv, and 1.5 ppmv for $HNO_3$, $H_2O$, HCl, and $O_3$, respectively. **Figure 6.29** displays the resulting model grades for $HNO_3$ versus EqL for each of the three θ bins. This methodology is then repeated for changes in $H_2O$, HCl, and $O_3$, discussed below in more detail.

We see from Figure 6.27 that the various CCMs develop significantly different average profiles for $HNO_3$ as a function of month, despite the evidence for fairly similar distributions during May (prior to the vortex formation and the presence of low enough temperatures for significant polar processing). Aura MLS $HNO_3$ data at 350 K to 600 K show (Figure 6.28) significant decreases (by 8 to 10 ppbv) at 69°S to 89°S from May to October. The steepness and magnitude of these (climatological) changes are best reproduced by CAM3.5 and WACCM, leading to high scores (Figure 6.29) for these models in this respect. These models' performances drop somewhat at 65°S, where the model decreases are larger than observed. Also, both of these models exhibit (Figure 6.27) a large vertical extent of low $HNO_3$ values (probably accompanied by low *T*), and thus get lower grades in the 600 K-800 K range, where the MLS data do not indicate such a rapid drop from May to July. In contrast, many models under-estimate the $HNO_3$ decrease in the 350 K - 600 K range especially in early winter, resulting in poor grades; these models perform better in the 600 K - 800 K range. More detailed views of the $HNO_3$ evolution can be studied from plots at each θ level, as shown in **Figures 6.30a** and 6.30b for the 500 K level; each of these figures displays only half of the available models, for clarity. However, assigning model grades from such plots (for each θ level) would create a difficult task to summarize. Averaging over a range of θ is thus chosen as the preferred approach. Similar figures at 500 K, but for $H_2O$ and HCl, are provided in the Supplementary Material for reference (Figures 6S.13 and 6S.14).

Considering now the evolution of the SH polar $H_2O$ in a similar manner, we refer to **Figure 6.31** and Figures 6S.15 and 6S.17 in the Supplementary Material. For EqL values larger (more poleward) than 69°S, the Aura MLS

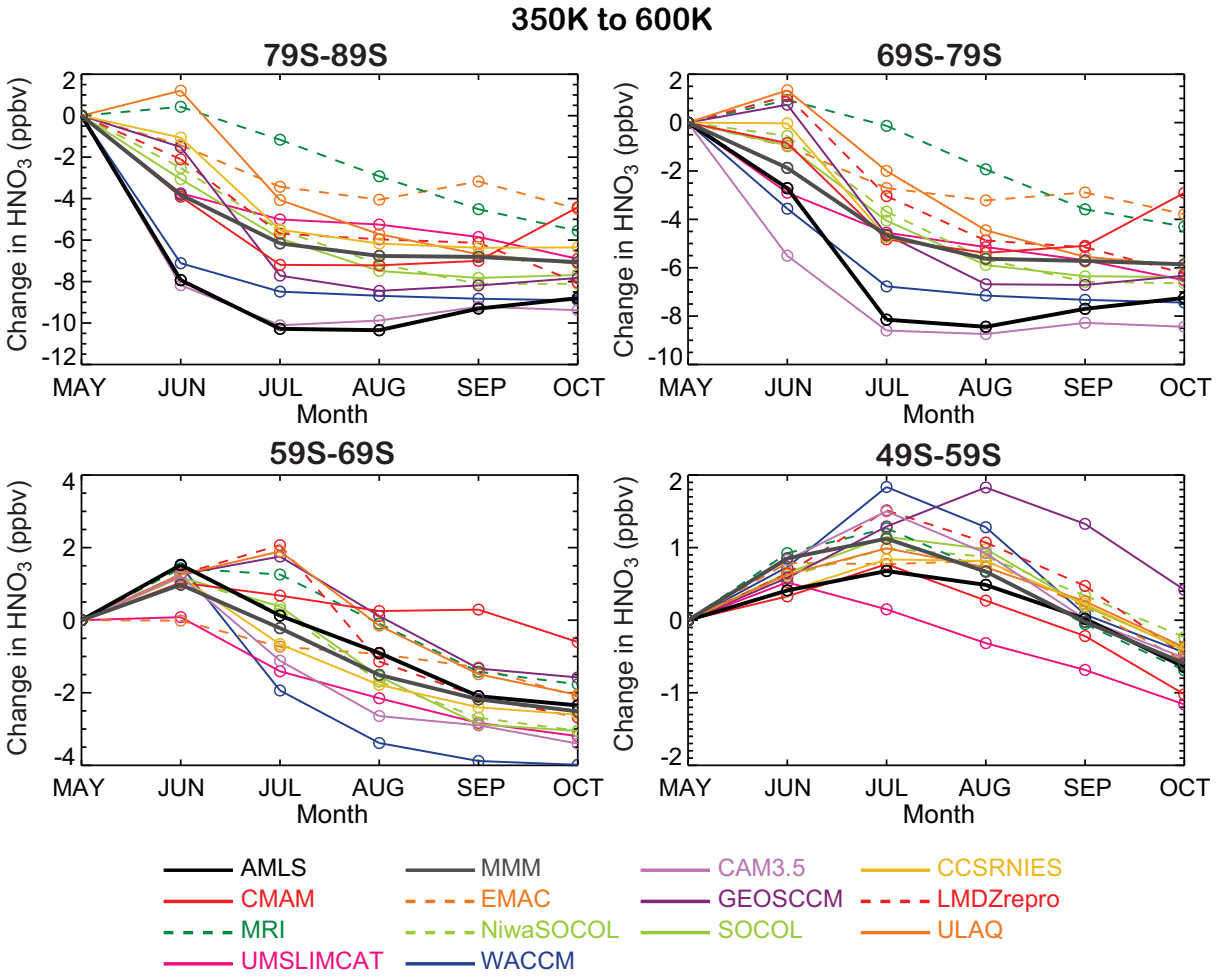


**Figure 6.28:** Change in $HNO_3$ from 350 K to 600 K, relative to May, for Aura MLS (abbreviated as AMLS in legend) and 12 CCM climatologies (legend uses first 4 letters of each model) and their multi-model mean (MMM).

climatology indicates that $H_2O$ decreases by 1 to 2 ppmv from May to August, with a mild increase from August to October. Models tend to follow this behaviour very well in the mean, and the multi-model mean (MMM) performs quite well. There are a few models that depart more from the average behaviour: AMTRAC, MRI, and WACCM exhibit significantly larger decreases in $H_2O$ (about 3 ppmv or more), leading to poorer grades for this process, whereas at the other extreme, GEOSCCM shows very little change in $H_2O$ during May to October. Other plots (not shown here) indicate that for some models (*e.g.*, WACCM), the low $H_2O$ values cover a wide vertical range and that this "dehydration" also happens for a significantly more extended time period than observed in the MLS data. As in the case of $HNO_3$, the spread in model distributions and model grades (see Figure 6S.17) decreases at the lower (equivalent) latitudes as well as at the higher altitudes (larger θ values); these regions are less influenced by winter polar chemical processes.

Similar observations hold for the chlorine activation fits, exemplified by the decrease and recovery in HCl, shown in **Figure 6.32** and in the Supplementary Material in Figures 6S.16 and 6S.20, with related model grades given in Figure 6S.18. Models tend to represent fairly well, on average, the observed climatological decreases in HCl (associated with chlorine activation on PSCs) in the Antarctic winter lower stratosphere. The observed HCl changes between May and August are slightly larger than 1.5 ppbv, for the EqL bins used here. On average, the models show smaller decreases (by about 0.5 ppbv) than observed, and only one model (UMUKCA-METO) produces a larger decrease than the observed climatological HCl decrease. The observed average HCl recovery from September to October is not followed quite as steeply in the models, although in some cases (*e.g.*, UMSLIMCAT), this recovery tends to happen faster and earlier than the MLS data suggest. Based on these average results, we might expect that chemical ozone loss arising from chlorine activation in the Antarctic would be fairly well modelled, although the somewhat smaller model activation could lead to an under-

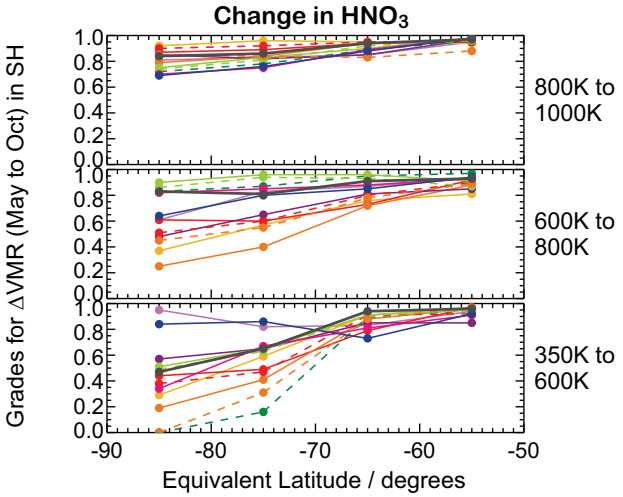


**Figure 6.29:** Grades obtained for 12 CCMs and their multi-model mean (MMM) from a comparison of model versus MLS-derived climatological changes in $HNO_3$ (see text and Figure 6.28). Grades are calculated for 4 EqL bins and 3 ranges of θ values. Colours and linestyles correspond to those shown in Figure 6.28.

estimation of the net chemical ozone loss (all other factors, *e.g.*, bromine, transport effects, being equal). However, the slightly longer time period for activation (in the CCMs) could, to some extent, counteract the magnitude of the activation itself (in a month when there are more day-time hours for ozone loss as well).

All the model grades discussed in this section are summarized in **Figure 6.33**, as a function of θ range and EqL. While the range of model results may be somewhat disconcerting (even with no observations), there are several instances of good to excellent fits *versus* the Aura MLS climatology. However, there is no model that fits the MLS VMR changes best all the time (May to October) and for all EqL bins, or for all species studied here. Also, a well-known factor relating to heterogeneous polar chemistry is the vertical/temporal extent of low temperature regions. We have seen in past work (*e.g.*, comparisons between MLS data and WACCM model values) that significant differences between model and data temperature values can lead to overestimates (or under-estimates) of "denitrification", "dehydration", and chlorine activation. However, more detailed studies of such differences for each CCM are beyond the scope of this report. It is hoped that the comparisons and grades given here can lead to some re-examination of the representation of dynamical and chemical processes in many, if not all, the CCMs used in this study, so that improvements in model performances can be obtained in the future.

### 6.3.4.2 Surface area density of PSCs

In this section we show nitric acid trihydrate (NAT) and water-ice (ICE) SAD results from 8 CCMs that submitted T3I output (instantaneous output; 10-day frequency). The aim of this section is to show the magnitude and variability between a small set of CCMs, not to grade their SAD distributions. In fact, currently there are limited observations available to grade the CCM SADs; however, we show these results with the hope of encouraging the observational community to assemble data sets for such comparisons and eventual diagnostic grading.

As in the previous section, the model results were translated from a latitude-pressure grid to a potential temperature (θ) - equivalent latitude (EqL) grid. **Figure 6.34** is one example of the model-derived distribution of SAD NAT and ICE at 480 K and 77.5° EqL. The SADs shown in this figure are the maximum abundance (binned per month) over a 15-year period (1990-2004). In addition, when the SADs were binned to the EqL-θ grid, only values of NAT and ICE SADs that were ~$1.0 \times 10^{-10}$ $cm^2$ $cm^{-3}$ ($cm^{-1}$) were used in the transformation from pressure-latitude to θ-EqL. The goal here was to examine SAD magnitudes where PSCs were present for a given EqL-θ condition. If there were no PSC particles present in the given EqL-θ bin, the SADs were set to zero. In Figure 6.34, the model results were divided into two groups: 1) with a maximum NAT SAD <10 x$10^{-9}$ $cm^{-1}$ (panel a); 2) with NAT SAD between ~10-50 x $10^{-9}$ $cm^{-1}$ (panel b). Out of the eight CCMs, three of the models have maximum NAT SAD distributions that strongly peak in June (CAM3.5, LMDZrepro, and WACCM); with three models showing a broad peak that is nearly constant in June, July, and August (ULAQ, NiwaSOCOL, SOCOL); and one model shows a broad peak between June and July (CCSRNIES). The NAT SAD from CNRM-ACM is similar in magnitude between June and September. In the previous section, the CAM3.5 and WACCM models do a nice job of representing the evolution of gas-phase $HNO_3$ poleward of 70°S for June through August relative to observations of $HNO_3$ from Aura MLS (Figure 6.28). Because these models show substantial denitrification from June through August, the subsequent NAT SAD also decreases rapidly over this period. CCSRNIES, ULAQ, NiwaSOCOL, SOCOL, and LMDZrepro all tend to overestimate the $HNO_3$ abundance in June relative to Aura MLS; again consistent with NAT SAD peaking in July and August for these models. The CNRM-ACM did not submit gas-phase $HNO_3$ to CCMVal and therefore was not evaluated in the previous section. However, examination of the total $HNO_3$ (gas-phase plus condensed phase) for this model showed little irreversible denitrification. This result is consistent with this model having the largest SAD. A large SAD implies smaller particles and therefore less sedimentation (see discussion below).

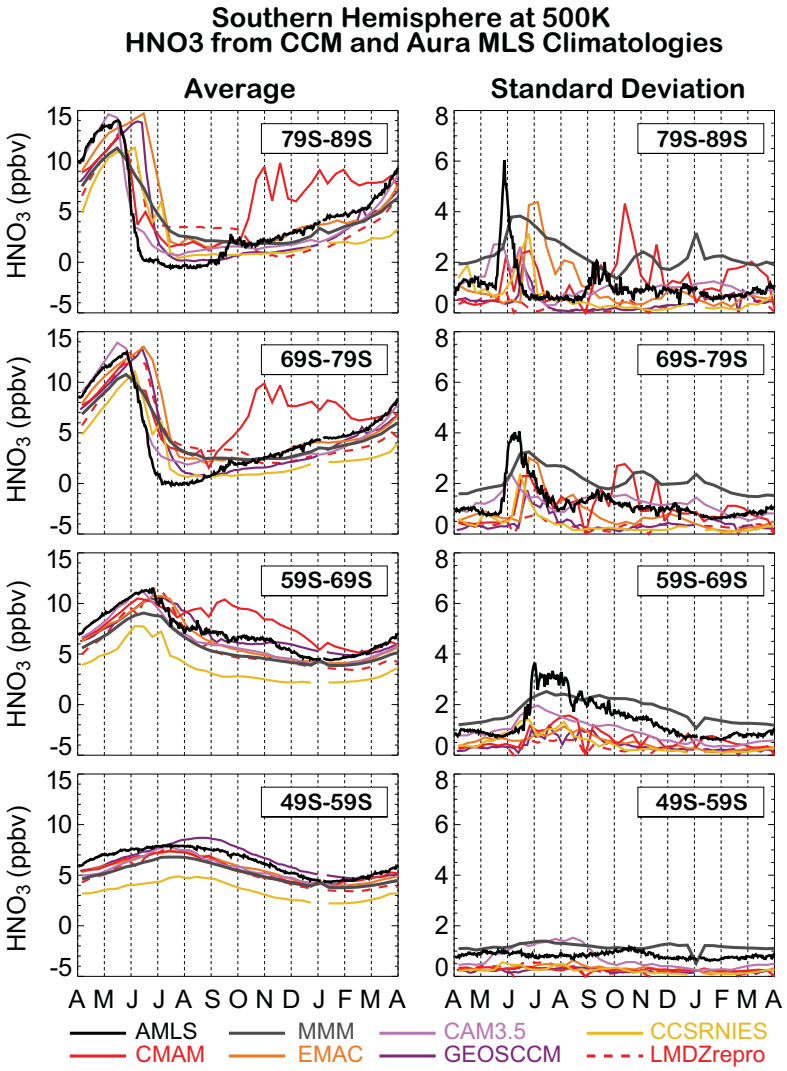


**Figure 6.30a:** Left panels display variations in average $HNO_3$ at 500 K during the course of a year in 4 EqL bins, based on climatologies from Aura MLS (black, solid lines) and 6 CCMs and their multi-model mean (with model sources shown in bottom legend). Right panels show the corresponding rms variability over the 5-year climatology, for each sampled day of year.

The large variability in the magnitude of SAD NAT between the CCMs is most likely due to assumptions made on the number of particles per $cm^{-3}$. For example, the WACCM model assumes 0.01 particles per $cm^{-3}$ and the maximum NAT SAD is shown to be ~$3x10^{-9}$ $cm^{-1}$ (not shown) - with a maximum over this period of approximately ~$8\text{-}10x^{-9}$ $cm^{-1}$. In **Table 6.5**, examples are shown of what the idealized NAT SAD (and radius) would be under different assumptions of $HNO_3$ abundance and NAT number density. As expected, the WACCM NAT SAD is consistent with those shown in Table 6.5 for particle densities between 0.01-0.001 particles $cm^{-3}$. In Figure 6.34, the SOCOL and NiwaSOCOL models derive one of the smallest mean NAT SAD abundances. These two models use an equilibrium NAT approach that does not fix the number of particles per $cm^{-3}$, instead, the mean radius is fixed (at 5 m). Therefore, according to Table 6.5, the NAT SAD should be ~1-2 x $10^{-9}$ $cm^{-1}$. This is again consistent with the magnitude of NAT SAD that is derived by the SOCOL and NiwaSOCOL models. For the models shown in panel b), *i.e.*, the CNRM-ACM and LMDZrepro models, the maximum NAT SADs is in the range 10-40 x $10^{-9}$ $cm^{-1}$, which would imply a much larger particle number density (~1 $cm^{-3}$) and smaller particle radius. A smaller NAT radius would therefore give less irreversible denitrification.

The ICE SAD is shown in the bottom row of **Figure 6.34**. Here, as in the NAT SAD comparisons, the models are grouped into two ranges: 1) where the maximum ICE SAD is < 50 x $10^{-9}$ $cm^{-1}$ (panel c); 2) with ICE SAD between ~50 - 250 x $10^{-9}$ $cm^{-1}$ (panel d). For this PSC type, one model has a maximum ICE SAD distribution that peaks in June (WACCM); six models peak in July (CAM3.5, CNRM-

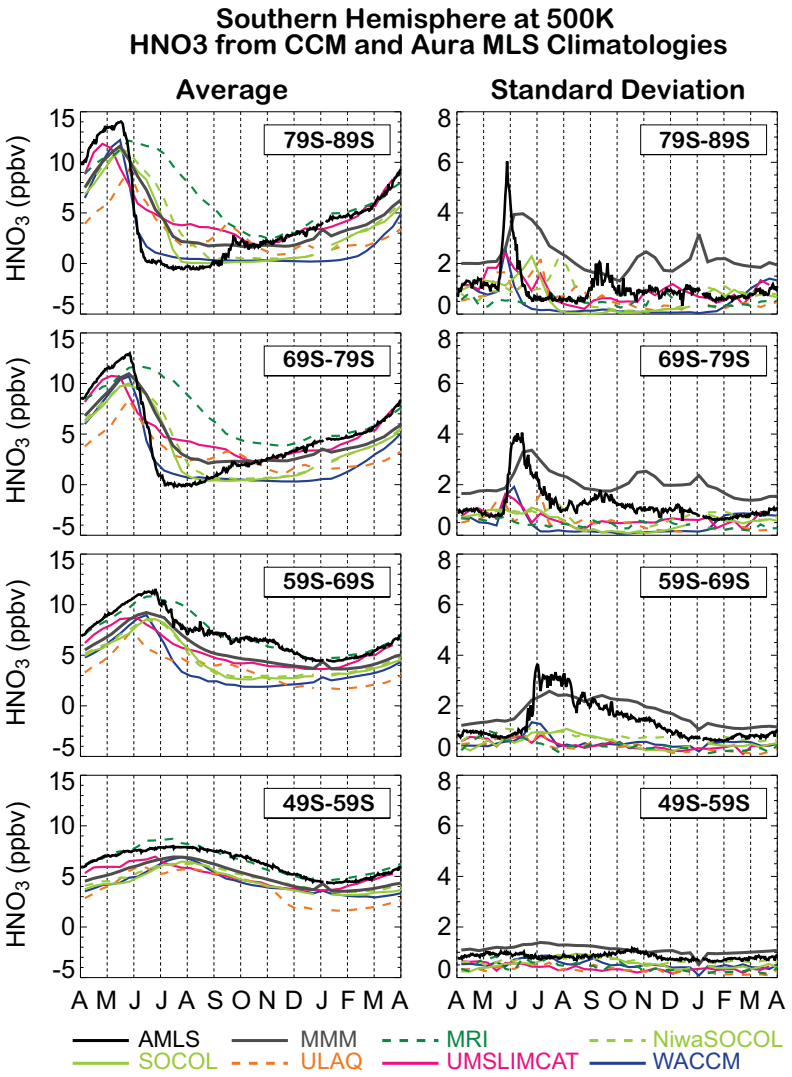


**Figure 6.30b:** Same as Figure 6.30a, but for Aura MLS $HNO_3$ (and its rms variability) compared to the 6 other available CCM distributions of $HNO_3$ versus time of year.

ACM, LMDZrepro, NiwaSOCOL, SOCOL, ULAQ), and one model peaks in August (CCSRNIES). Similar to the NAT discussion above, the range in ICE SAD magnitude can be attributed to assumptions regarding particle density. For example, it is known that the particle density is 0.001 and 0.1 $cm^{-3}$ for the WACCM and SOCOL models, respectively. Therefore, it is not surprising that there is over a factor of six difference in the derived ICE SAD between these models. These derived SADs are also consistent with the idealized ICE SAD as listed in Table 6.5.

In summary, more work is needed to evaluate NAT and ICE aerosols. In addition to evaluating the SAD, the radius, and size distribution of these aerosols should be examined. Comparison to observations is clearly needed; currently there are not any global data sets available that can be used to evaluate these constituents. In addition, future CCM aerosol evaluations should examine the model distributions and reactivity of sulfate aerosols. In CCMVal-2, the sulfate SAD fields are prescribed, but modelling groups are beginning to couple microphysical models to their CCMs; these types of couplings will allow scientist to examine the future aerosol loading based on assumptions of the evolution of tropospheric sulfate species.

### 6.3.4.3 Chemical ozone depletion in the polar vortices

Heterogeneous processes in the polar lower stratosphere initiate large chemical ozone depletion during late winter and spring in the Antarctic and during cold winters in the Arctic. Within the isolated polar vortex, very cold temperatures result in the formation of polar stratospheric clouds (PSCs). Heterogeneous reactions that convert halogen reservoir species to more active forms occur on the surfaces of PSCs, *e.g.*, nitric acid trihydrate (NAT) particles (Hansen and Mauersberger, 1988), water-ice particles,

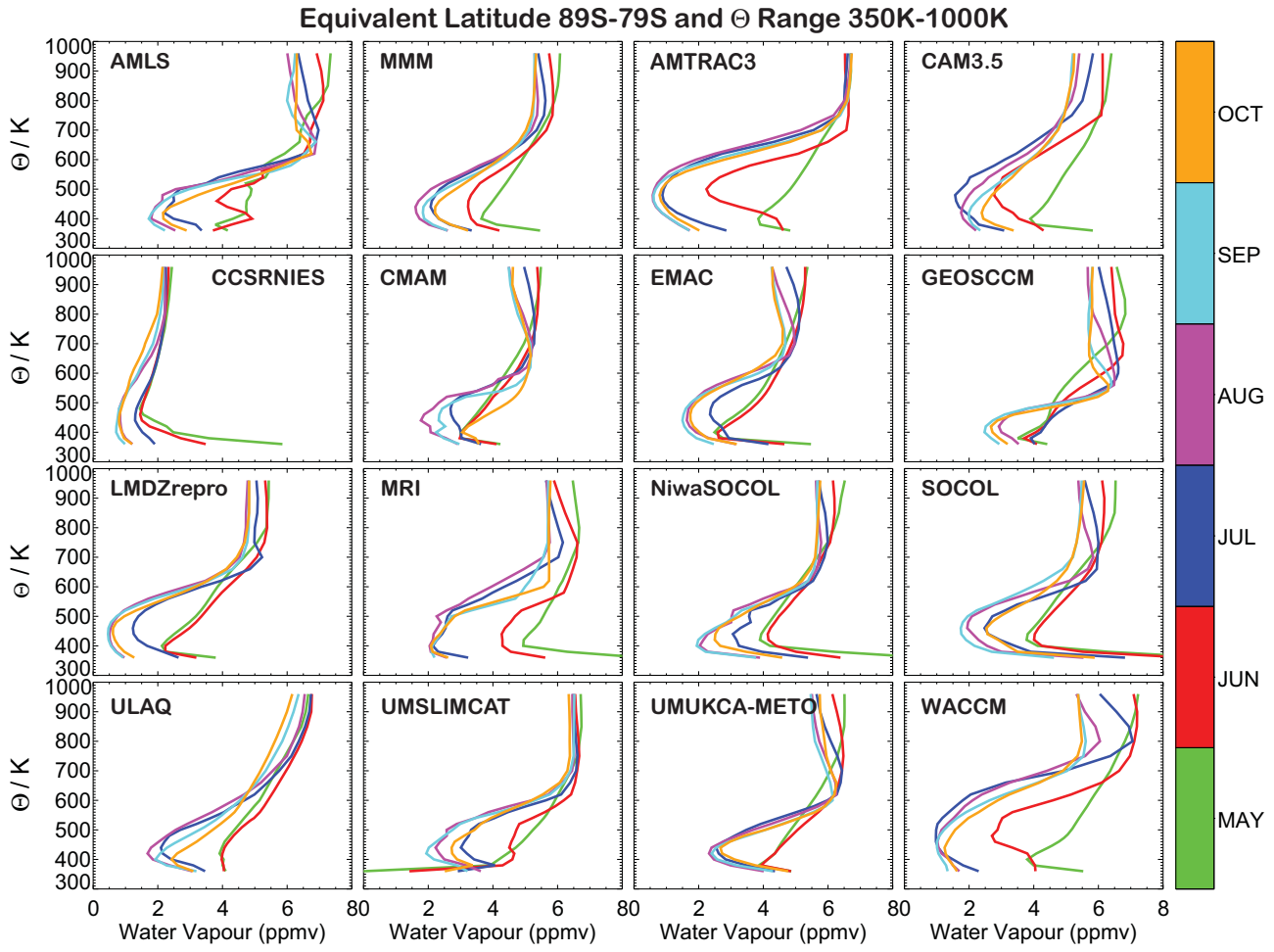


**Figure 6.31:** Climatological profiles of $H_2O$ from mid-May through mid-October for Aura MLS, 14 CCMs, and the multi-model mean.

as well as on liquid sulfate aerosols (*e.g.*, Solomon *et al.*, 1986; Peter 1997). During late winter/spring, the increasing solar illumination of the vortex region increases the photolysis rate of the ClO dimer, enhancing ozone depletion (*e.g.*, Solomon, 1999). This process continues until the vortex temperatures warm past the threshold of PSC formation and/or there is a major stratospheric warming.

### *TRAC Method*

The extent of chemical ozone depletion occurring in the polar vortex during the polar winter and spring depends strongly on: 1) The dynamical conditions in the polar vortex, 2) temperature, 3) the degree of isolation of the vortex, and 4) the duration of chlorine activation. In addition, the abundance of inorganic halogens in the polar stratosphere is also important for determining ozone depletion within the vortex (*e.g.*, Newman *et al.*, 2007). Other important factors that influence chemical ozone depletion include the extent of denitrification and dehydration by sedimentation of PSC particles.

The diagnosis of chemical ozone depletion in the polar-regions is not straightforward. Decreasing ozone mixing ratios in spring, as a result of chemical depletion are often masked by the descent of ozone-rich air at high latitudes, especially in the NH. The tracer-tracer correlation method (TRAC) was developed to quantify chemical ozone depletion in absence of transport processes within an isolated polar vortex (*e.g.*, Proffitt *et al.*, 1993; Müller *et al.*, 1997; Tilmes *et al.*, 2004). This method has the advantage in that it does not rely on any additional model simulations to quantify the passive ozone (*i.e.*, ozone in the absence of chemical loss), which can lead to uncertainties as a result of the simulated transport. The vortex average depth of chemical depletion in column ozone between 350 K - 550 K potential temperature was derived for the period between early winter and spring. For this purpose, we used satellite observations from the HALOE/UARS, ILAS/ADEOS, and ILAS-2/ADEOS-2 instruments, combined with balloon and aircraft observations (Tilmes *et al.*, 2006). The edge of the polar vortex was defined using the criterion of Nash *et al.* (1996). The results derived using the tracer-

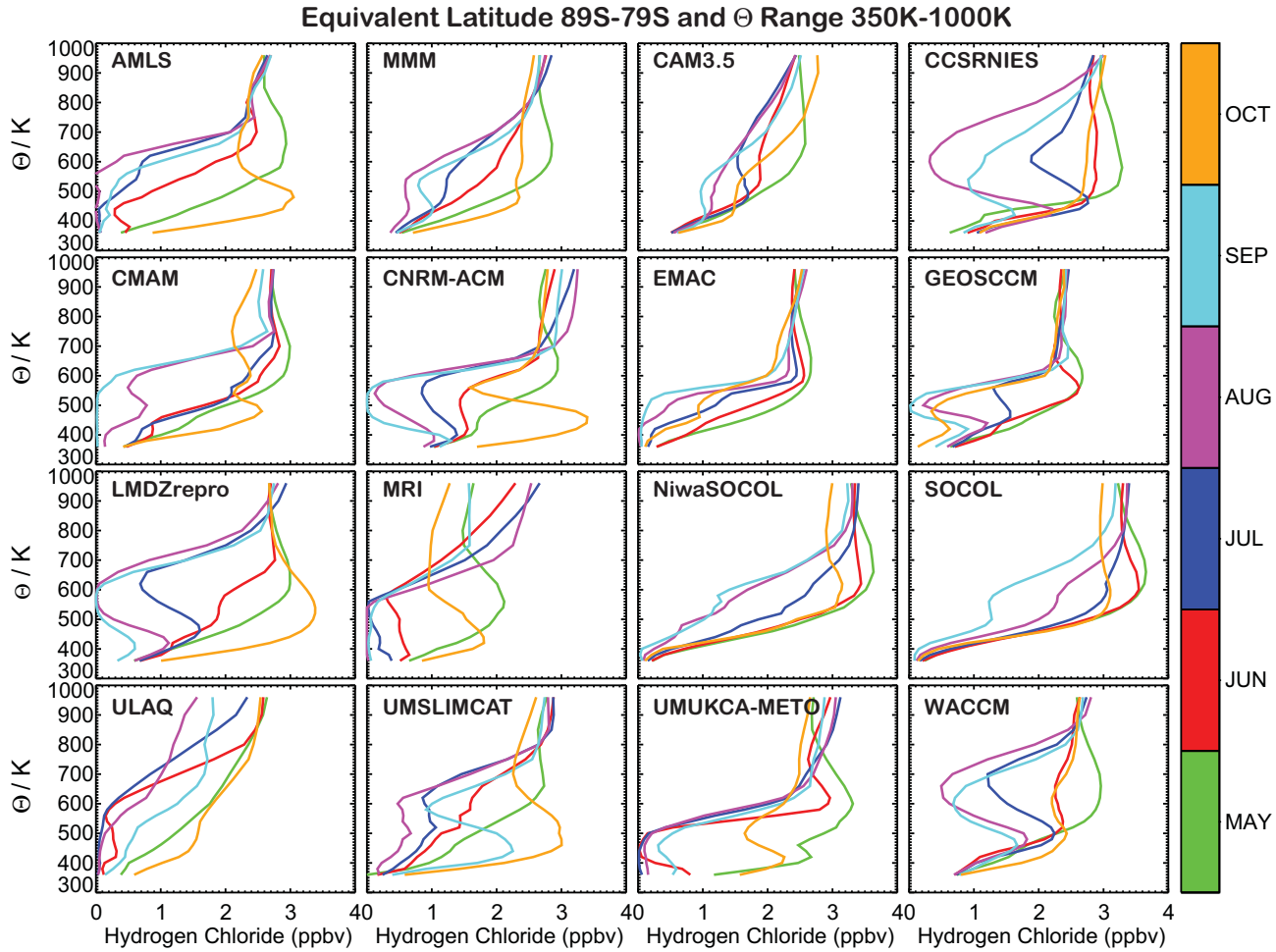


**Figure 6.32:** Climatological profiles of HCl from mid-May through mid-October for Aura MLS, 14 CCMs, and the multi-model mean.

tracer correlation method (TRAC) are in good agreement with results from other established methods (Tilmes *et al*., 2004; WMO, 2007). There are clearly uncertainties in all ozone depletion approaches, however, the TRAC method has been shown to result in an under-estimation of chemical ozone depletion rather than in overestimation in cases of a less isolated polar vortex, as summarized in Müller *et al*. (2005, 2008).

### *Potential for Activation of Chlorine*

Chemical ozone loss depends on temperature conditions in the vortex. However, the averaged vortex temperature is not linearly related to chemical ozone depletion. For example, very cold temperatures in a very small area of the vortex can result in very different amount of ozone depletion than homogeneously distributed moderately cold temperatures over the entire vortex. In addition, the temperature evolution during winter and spring is an important factor. A temperature-based measure was developed that describes the fraction of the vortex where temperatures are low enough to allow the activation of chlorine during winter and spring. This measure is called the potential for chlorine activation (PACl) and details can be found in Tilmes *et al*. (2008). PACl is a measure that quantifies to what amount meteorological conditions allow chlorine to be activated, and therefore ozone depletion to occur. This measure however does not necessarily imply that the model vortex size and temperature distribution are simulated correctly.

$PACl_{met}$ is defined as: $V_{ACl}/V_{vortex}$, where the $V_{vortex}$ is the volume of the vortex derived using the Nash criterion and $V_{ACl}$ is volume of the vortex where the temperature is below a threshold temperature for chlorine activation. This threshold temperature is calculated based on pressure, altitude, surface area densities of liquid sulfate aerosol, and water vapour abundance (Tilmes *et al*., 2007). If the SAD of liquid sulfate aerosols is not available for the given CCM, we use the SAD climatology as specified for the REF-B1 scenario. PACl is averaged over a given potential temperature range and the period considered. This measure allows the comparison of polar vortices with vary-

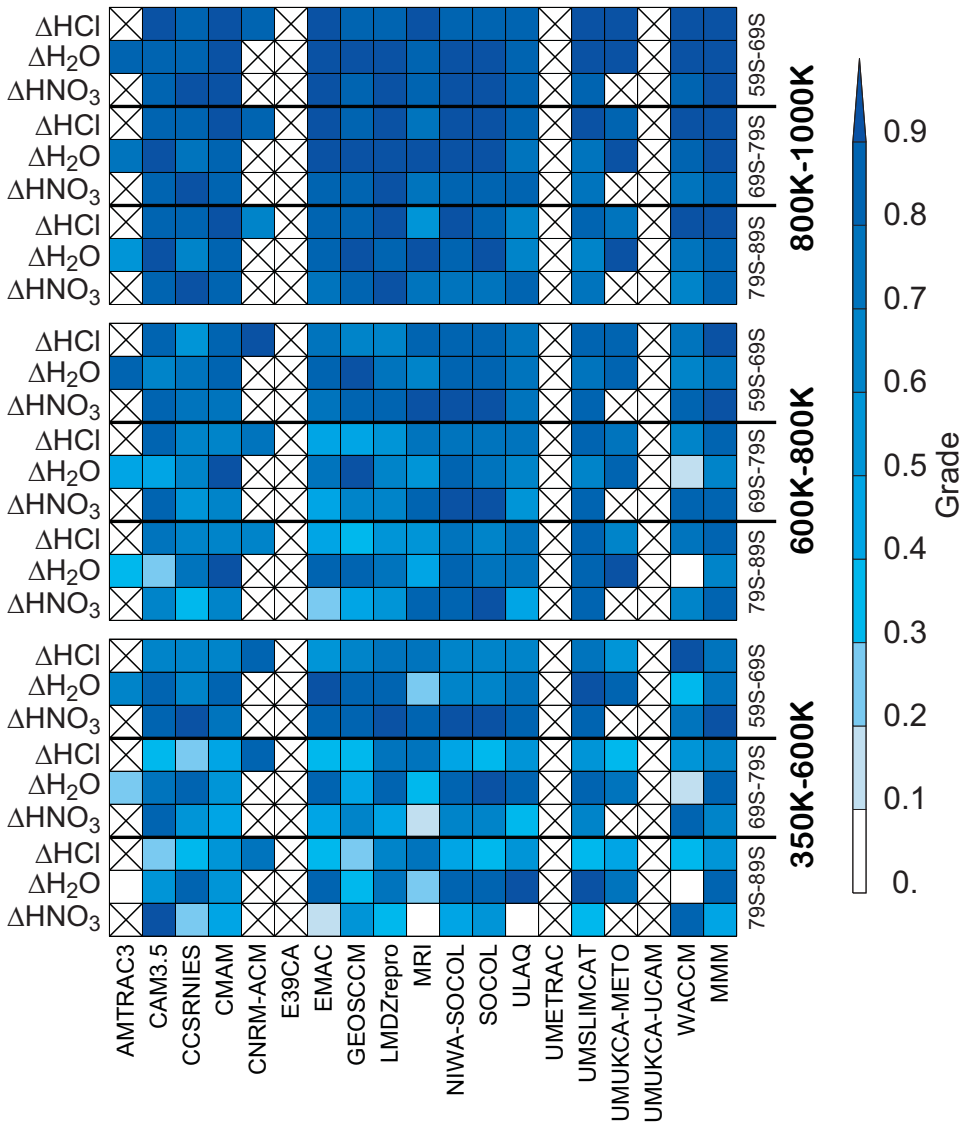


**Figure 6.33:** Summary of grades (shown previously in this section) relating to SH changes in $HNO_3$, $H_2O$, and HCl (from May to October) for 3 EqL bins (centred at 85°S, 75°S, and 65°S). Each plot refers to a different θ range (see legend at bottom).

ing vortex volume, for example the Arctic and Antarctic. It is also useful to evaluate the polar chemistry of various CCMs with varying vortex volumes in both hemispheres, even though models might not reproduce the size of the polar vortex correctly.

A linear relation between Arctic chemical ozone loss and PACl was established based on observations between 1991 and 2005 for a period with maximum stratospheric halogen loading. To consider varying halogen loading in the stratosphere (*e.g.*, Newman *et al.*, 2006), the $PACl_{met}$ value is extended to a measure that includes the impact of changing EESC. Therefore, $PACl = PACl_{met} \times EESC_n$, where $EESC_n$ is the normalised EESC for year *n* (assuming an age-of-air of 5.5 years). A linear relationship between ozone loss and PACl can then be derived for the SH as well, and can be used to summarize the performance of different CCMs (Tilmes *et al.*, 2007). To evaluate the representation of heterogeneous processes in CCMs, the dynamical and chemical conditions for chemical ozone depletion will be compared with available observations. In particular, we consider the ability of the models to reproduce the potential of chlorine activation that is necessary to match observed chemical polar ozone loss.

### *Evaluation of CCM PACl and Chemical Ozone Loss*

The performance of the models is again graded by deriving *g* values, following Equation (6.1). Here, $\mu$ is the

**Table 6.5:** NAT and ICE particle properties derived for different assumptions of the particle number density and precursor molecule abundances. For NAT particles the radius and SAD are derived for 1 and 5 ppbv $HNO_3$ (left and right numbers in the radius and SAD columns). For ICE particles the radius and SAD are derived for 1 and 3 ppmv $H_2O$ (left and right numbers in the radius and SAD columns). The SAD was derived assuming spherical particles. These conditions are only valid inside NAT and ICE clouds. Both particle properties were derived at 30 hPa and 190 K (Thomas Peter and Beiping Luo, personal communication, 2009).

| SAD Type | Number Density ($cm^{-3}$) | Radius (µm) | Surface Area Density ($x10^{-9}$ $cm^2$ $cm^{-3}$) |
|---|---|---|---|
| ***NAT*** | | | |
| | 10 | 0.15 / 0.26 | 28 / 83 |
| | 1 | 0.32 / 0.55 | 13 / 38 |
| | 0.1 | 0.70 / 1.2 | 6.1 / 18 |
| | 0.001 | 3.2 / 5.5 | 1.3 / 3.8 |
| | 0.0001 | 7.0 / 12 | 0.6 / 1.8 |
| ***ICE*** | | | |
| | 10 | 0.96 / 1.4 | 1200 / 2480 |
| | 1 | 2.1 / 3.0 | 540 / 1120 |
| | 0.1 | 4.5 / 6.5 | 250/ 520 |
| | 0.01 | 9.6 / 14 | 120 / 250 |

mean value of ozone loss or PACl over the years between 1990 and 2005. Furthermore, instead of using the standard deviation $\sigma$ of the observations, we use the mean error of the ozone loss in particular years. This is because the standard deviation of the considered distributions in the Arctic is of the same magnitude as the observed values; for the Antarctic, $\sigma$ is much smaller than the uncertainty of the measurements. We use a value 3 for $n_g$.

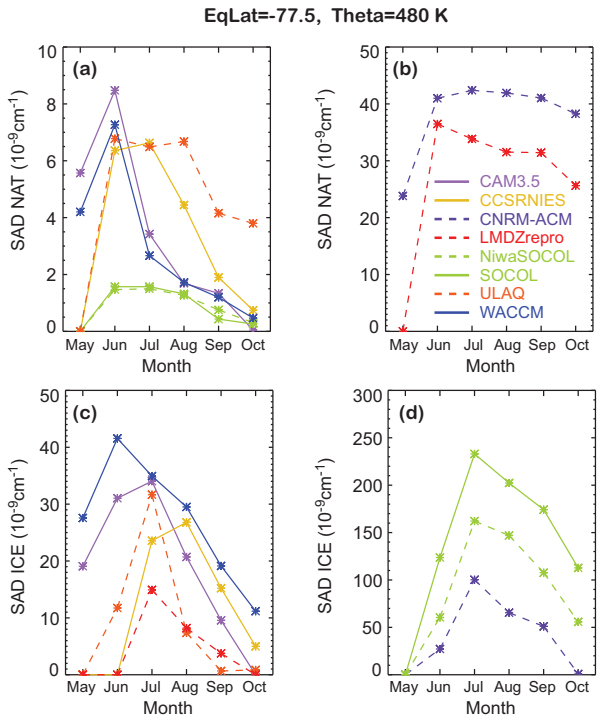


**Figure 6.34:** Comparison of model maximum surfaces area density (SAD) for (a, b) NAT (top row) and (c, d) ICE (bottom row). See text for details on binning procedure.

The following grade ($g$) values for Arctic and Antarctic conditions are employed here:

- $g_{pacl}$ the grading of the models to reproduce conditions for chlorine activation.
- $g_{O3}$ the grading of the models to describe chemical polar ozone depletion.

Both these grades together allow the quantification of the ability of models to reproduce chemical ozone depletion and chlorine activation with regard to observations and, therefore, the ability to reproduce observed chemical ozone depletion as a result of a reasonable representation of meteorological conditions in the polar vortex.

A good grade in PACl does not necessarily lead to a good grade in ozone depletion and *vice versa*. The ability of a model to reproduce the observed chemical ozone depletion is not independent of the simulated volume of the vortex, nor the isolation of the vortex. A smaller vortex will in general lead to less ozone depletion than a larger vortex, since in spring the sun reaches the cold vortex area at a later time. In addition, the location of the vortex relative to the pole is important. Therefore, it is important to evaluate the vortex volume if diagnostics such as ozone hole area are considered. Further, if the polar vortex is not well isolated, the TRAC method will result in an under-estimation of chemical ozone depletion. However, this problem is reduced here by considering only ozone loss in the vortex core (as described in the next section).

For this analysis we use results from the REF-B1 simulations to evaluate the evolution of chemical ozone

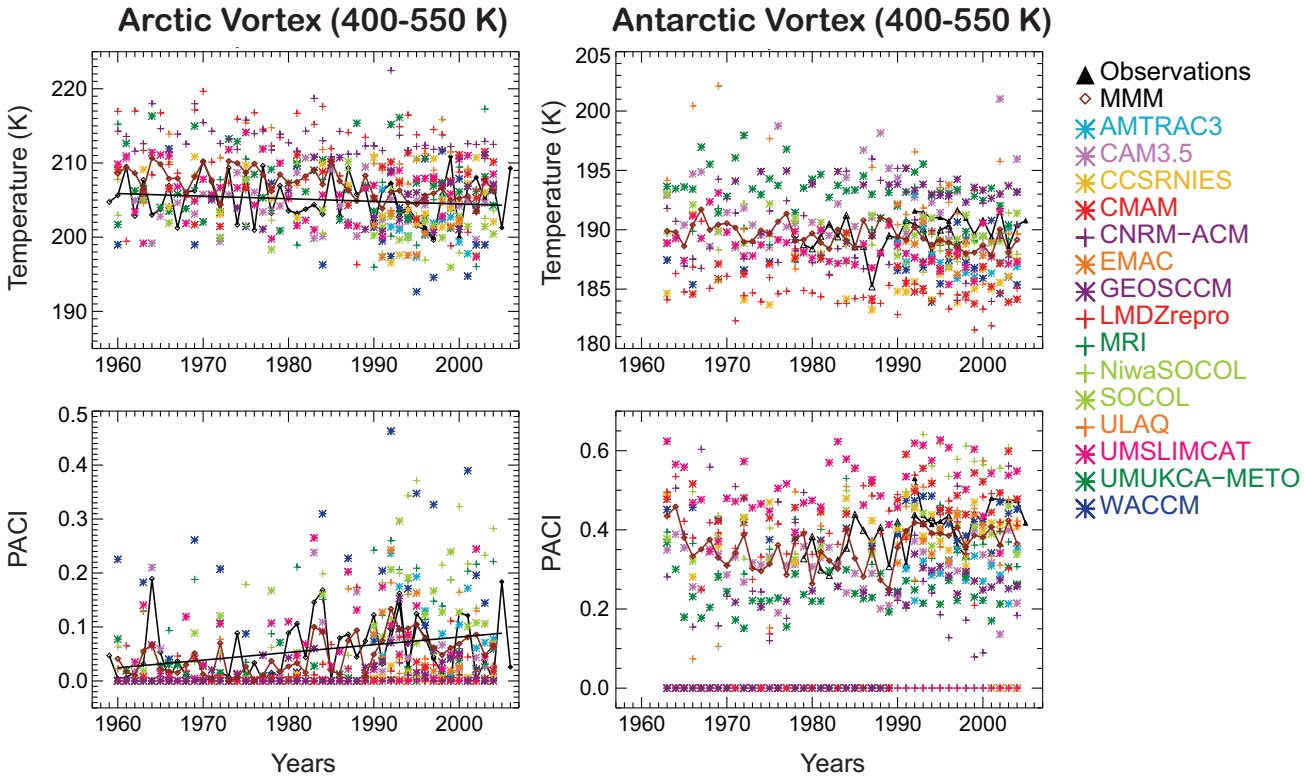


**Figure 6.35:** Vortex average temperatures (top), and PACl (bottom) from January through March for the Arctic (left) and from July through September for the Antarctic (right) and between 440-550K. Values derived from meteorological analyses (UK Met Office between 1991-2005 and ERA-40 1958-1999) are shown in black. The multi-model mean is shown in brown. Model results are shown in different symbols and colours.

depletion with changing atmospheric halogen content between 1960 and 2005. The period between 1990 and 2005, for which sufficient observational information is available, will be graded. We use T3I output for this diagnostic and all model results are transformed to EqLat/θ surfaces.

### 6.3.4.4.1 Meteorological conditions in the polar vortex

*Vortex Temperatures*

Average vortex temperatures for a period between January through March (Arctic) and July through September (Antarctic) were derived between 1960 and 2005 and we use the criterion derived by Nash *et al*. (1996) to identify the edge of the polar vortex. **Figure 6.35** (top panel) compares Arctic and Antarctic temperatures for models and observations. For the Arctic, the majority of models are able to simulate Arctic temperatures in the range of ERA-40 and UK Met Office analyses. In general, models do follow the observed decreasing trend in temperatures between 1960 and 2005. A few models scatter well above or below the observed range. The models that simulate warmer temperatures than the observations are not expected to simulate significant chemical ozone depletion in the Arctic polar vortex; the required threshold temperature where chlorine activation and therefore ozone depletion can be expected will likely not be reached. For the Antarctic, models show a larger spread in polar vortex temperatures than for the Arctic.

*Meteorological Potential for chlorine activation*

$PACl_{met}$ was derived between 1960 and 2005 (Arctic) and 1979 and 2005 (Antarctic) for a period between January through March (Arctic) and July through September (Antarctic). Different meteorological analyses (ERA-40 and UK Met Office, Figure 6.35, bottom panel) result in an uncertainty of observed $PACl_{met}$ values of ~10% for the Antarctic and ~20% for the Arctic. We apply the grading (Equation 6.1) to both, the mean values of the $PACl_{met}$ distribution ($g_{pacl\_mean}$) and the standard deviation of the distribution ($g_{pacl\_std}$) derived from models and observations for the Antarctic and the Arctic between 1990 and 2005. This is then consistent with the period chosen for the grading of ozone loss. Both these values are equally important to quantify the representativeness of the models, because the standard deviation of the distribution is a meas-

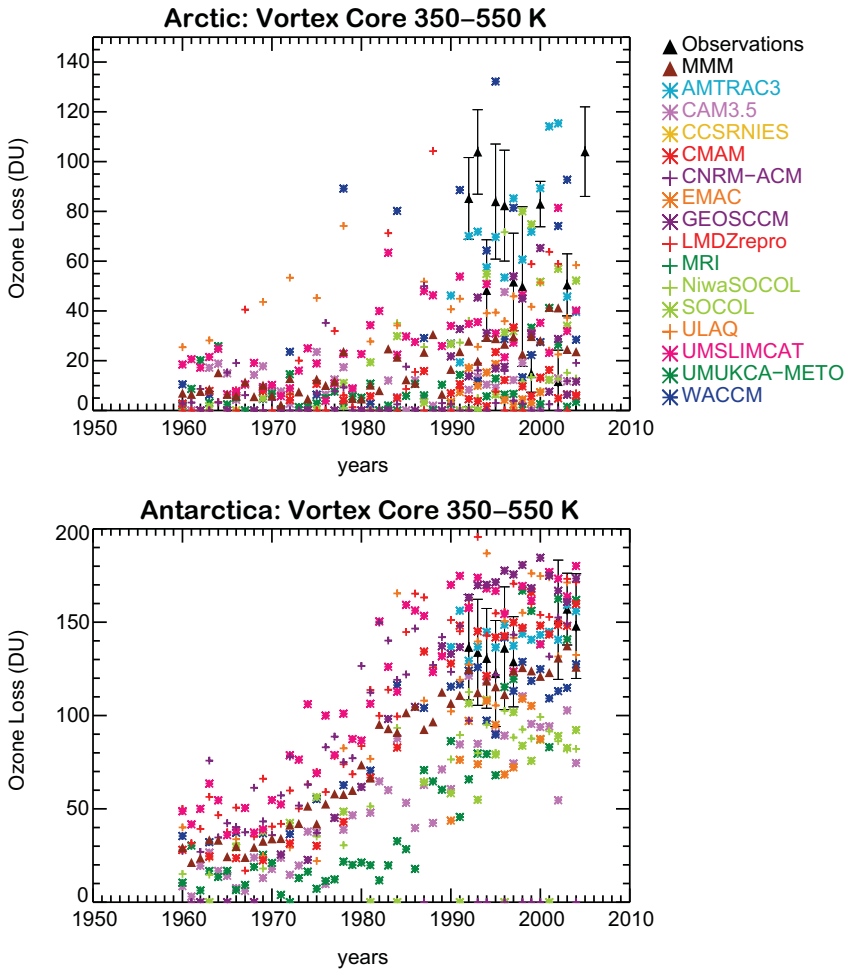


**Figure 6.36:** Chemical ozone depletion in the polar vortex from January through April (top panel) and July through October (bottom panel) between 350-550 K. Results from observations (black triangles) were derived from HALOE/UARS (Tilmes et al., 2006) for the polar vortex core. The multi-model mean (MMM) is shown in brown. Model results are shown in different colours and calculated within Eqlat >80°.

ure for the interannual variability of $PACl_{met}$. Both grades are combined to give the overall grading for $PACl_{met}$: $g_{pacl} = (g_{pacl\_mean} + g_{pacl\_std})/2$ (Figure 6.39, first and third columns).

For the Antarctic, only two models (out of 14) show $g$ values smaller 0.5. Meteorological conditions in most of the models provide the conditions for the occurrence of observed chemical ozone loss (however, as mentioned previously, the temperature distribution and vortex size might still be wrong). In many cases, the standard deviation of the distribution (*i.e.*, the variability) is better represented than the mean values. For the Arctic, about half of the models are able to reproduce PACl values with a grade of 0.5 or better. As for the SH, in general, models reproduce the value of the standard deviation better than the mean values of the distribution.

### 6.3.4.4.2 Evolution of Chemical Ozone Loss in the Polar Vortex

The tracer-tracer correlation method was applied consistently to the output of all CCMs to derive the depth of chemical ozone depletion in the Arctic between January through April and the Antarctic between July through October as shown in **Figure 6.36**. The impact of potential underestimation of chemical ozone depletion, as a result of a less isolated polar vortex in the models will be especially strong at the vortex edge. This impact is reduced by considering the area of the vortex within EqLat > 80°, *i.e.*, within the vortex core. In case of very diffusive models, a strong underestimation of chemical ozone depletion in the polar vortex core points to the inability to reproduce realistic ozone values for that particular CCM. Therefore, the low grades that emerge for excessively diffusive models are appropriate. Possible shortcomings of the models in reproducing the entire polar vortex are not considered here.

All models that are able to simulate chemical ozone loss in the Arctic polar vortex show an increase of ozone depletion in the Arctic between 1960-2005, as expected due to the increasing halogen content in the stratosphere and the increasing PACl as a result of decreasing temperatures with time (Figure 6.36). To evaluate the models with regard to observations, we consider the period between 1991 and 2005. The mean values of chemical ozone loss for this period, as well as the standard deviation of chemical ozone depletion of the model results, are graded compared to observations. As above, we combine the two grades for ozone depletion as follows: $g_{O3} = (g_{O3\_mean} + g_{O3\_std})/2$ (Figure 6.39, second and fourth columns).

For the Antarctic, most of the models that obtained a

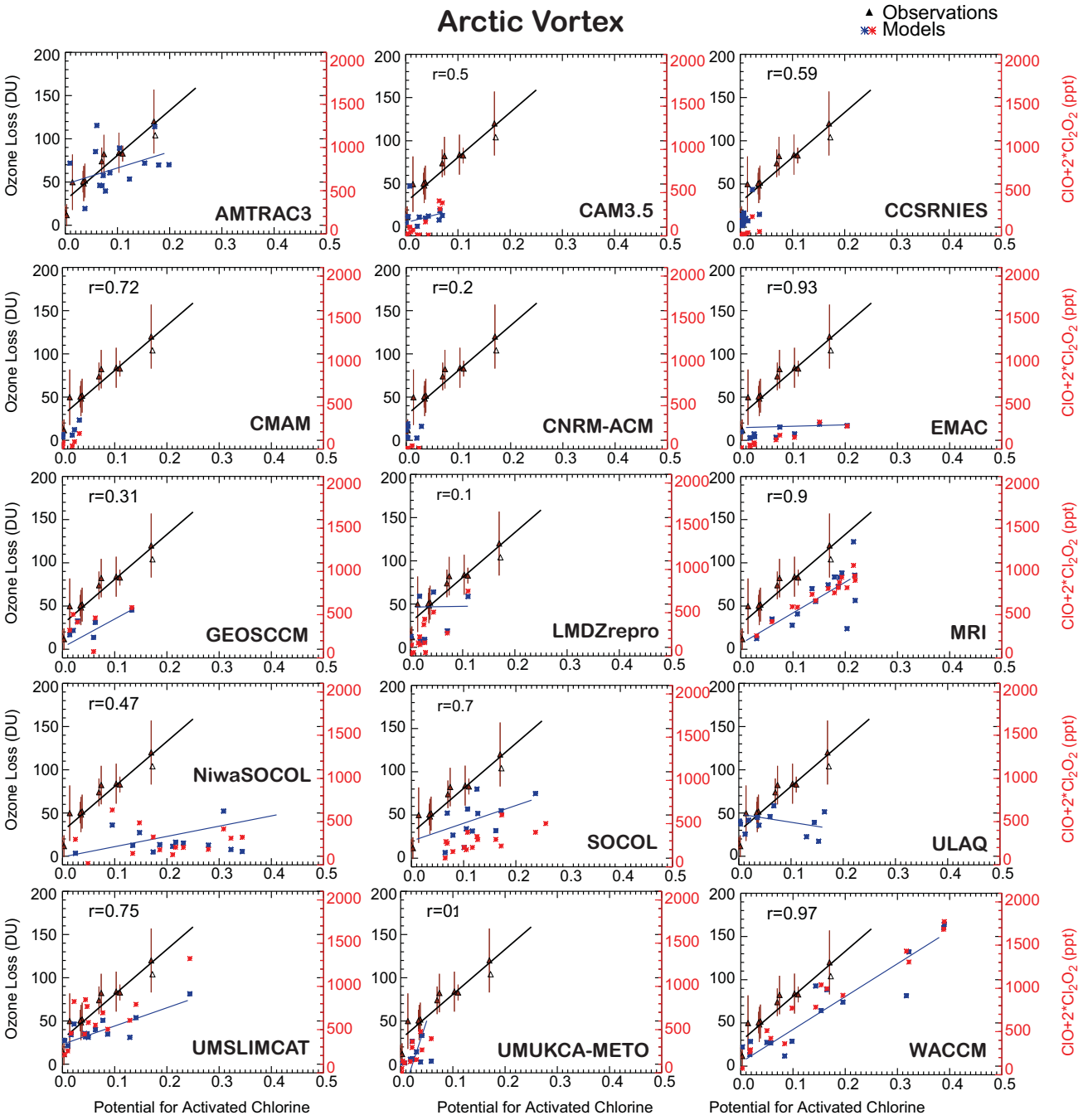


**Figure 6.37:** Relationship between Arctic chemical ozone loss (Figure 6.36) and the potential for activated chlorine (PACl) for the years between 1990 and 2005. Both observations (black triangle) and model results (blue asterisk) are shown. Model $Cl_x$ ($ClO + 2Cl_2O_2$) versus PACl is also shown (red asterisk). The correlation coefficient (r) between model $Cl_x$ and chemical ozone loss is shown in each panel.

high PACl grading also have a high score for the ozone depletion grading. This outcome of the grading is reassuring in so far as the two diagnostics should be connected. Some models do show differences between the two diagnostics. These differences are discussed in the next section. For the Arctic, the grade of the PACl and ozone depletion in the models often varies widely. This points to the uncertainty of models in reproducing Arctic chemical ozone depletion as a result of reasonably reproduced meteorological conditions. Less than half the models reach grades of $g_{O3}$ above 0.5. Only, two models reach grades above 0.8.

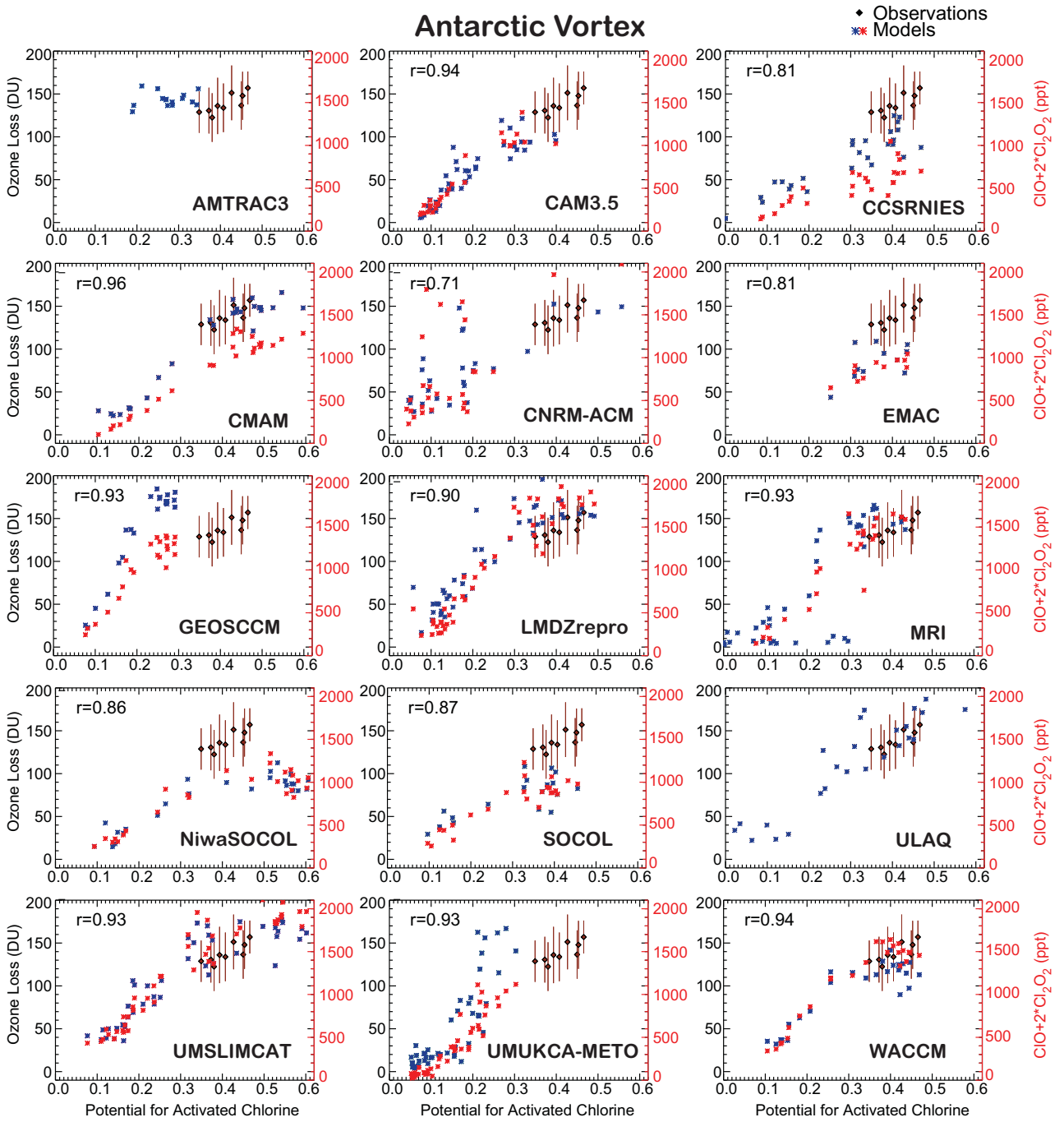


**Figure 6.38:** Relationship between Antarctic chemical ozone loss (Figure 6.36) and the potential for activated chlorine (PACl) for the years between 1960 and 2005 (blue asterisk). Model $Cl_x$ ($ClO + 2Cl_2O_2$) versus PACl for the same period is also shown (red asterisk). The observed chemical ozone loss versus PACl are between 1990 and 2005 (black triangle). The correlation coefficient (r) between model $Cl_x$ and chemical ozone loss is shown in each panel.

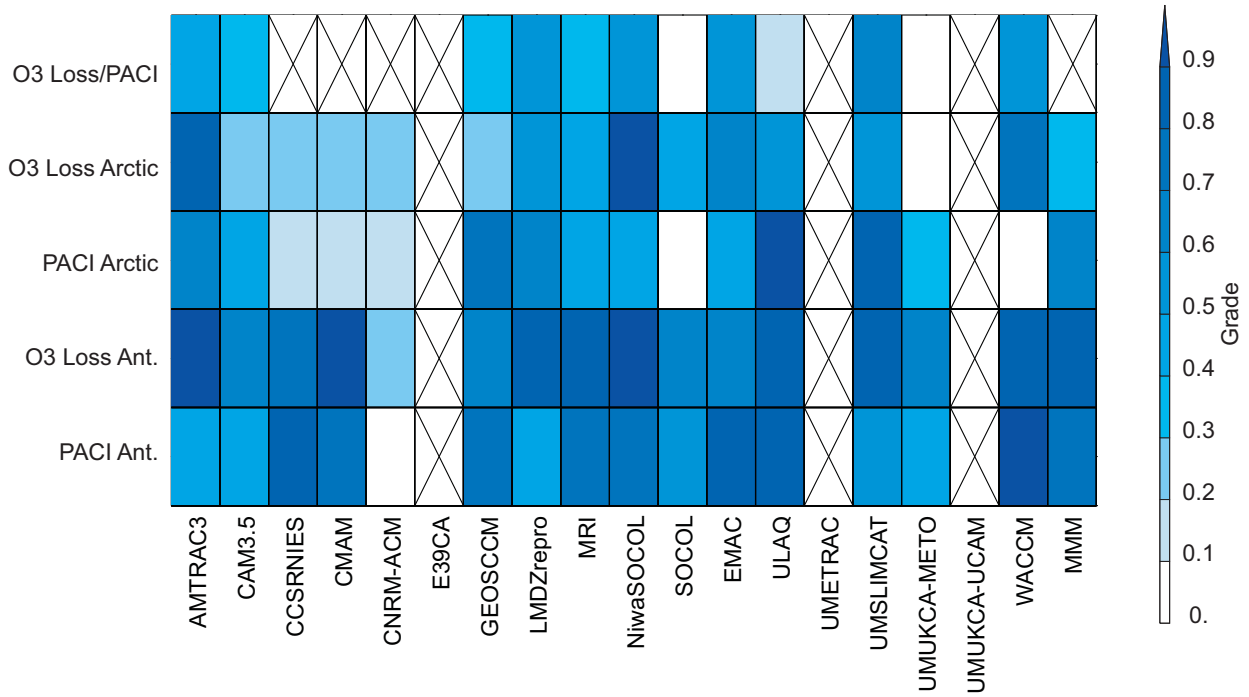


**Figure 6.39:** Summary of grades, as discussed in the text. Crosses indicate those models that could not be evaluated for a specific grade. $O_3$/PACl grading was performed for only those models with at least 2 values larger than 0.03.

### 6.3.4.4.3. Polar Chemical Ozone Depletion vs. PACl and ClOx

The relationship between ozone loss and PACl summarizes the performance of the model with regard to heterogeneous processes and chemical ozone depletion (**Figures 6.37** and **6.38**). In addition we show simulated $Cl_x$ (= ClO + $2Cl_2O_2$) averaged over the entire vortex between 400 K - 550 K (if the model output is available). There are no $Cl_x$ observations available for various years in the polar vortex to evaluate the models. Nevertheless, the amount of $Cl_x$ in the models provides further information to what degree PACl and $Cl_x$ are related in each model, since PACl is based on meteorological conditions and not on the actual simulated chlorine loading. Most models describe a tight relationship between $Cl_x$ and PACl. The different slopes of the relationship between ozone loss and PACl and ozone loss and $Cl_x$ are a result of different sensitivity of $Cl_x$ to PACl in the models. In Figures 6.37 (Arctic) and 6.38 (Antarctic) we present a model-to-model inter-comparison of these relationships between $Cl_x$ and PACl. For the Arctic, available observations allow the evaluation of the polar chemistry in comparing the slope of the relationship between chemical ozone depletion and the PACl. If a model reproduces the slope of this relationship, the meteorology in the model results in appropriate ozone depletion. Therefore, models which show either too much chlorine activation, or too little (to a certain degree if at least two years show PACl values are larger than 0.03) can be still tested for the quality of their chemical mechanism. The uncertainty of the slope of this relationship cannot be estimated precisely, so the outcome of the grading is a matter of the choice of the uncertainty and is therefore rather unreliable. Here we chose an error for the observed slope of 33% to grade the models (**Figure 6.39**, fifth column). The graded slope of the model includes the *y*-axis intercept, as well as the ratio between ozone loss and PACl. Qualitatively, the slope of the relationship between ozone loss and PACl is well reproduced in some models. For example, for WACCM, the PACl values are not graded high, although a reasonable slope shows that the mechanism for chemical ozone loss is reliable even though the meteorology might not allow the observed amount of ozone depletion. For most of the models PACl and $Cl_x$ values correlate well. UMSLIMCAT shows slightly higher $Cl_x$ values and SOCOL slightly lower values with respect to PACl than other models.

For the Antarctic, the slope between ozone depletion and PACl cannot be graded, because chemical ozone loss in the period where observations are available is saturated and no significant change in ozone loss with changing PACl is expected (Tilmes *et al.*, 2006). No significant dependence of ozone loss on PACl values is observed for the years between 1991 and 2005. Most models agree with observed Antarctic ozone loss, although a larger spread exists in the PACl values between the models. Some models show a rather poor representation of PACl with grades be-

low 0.5, although chemical ozone depletion is well within the range of the observations. These models indicate too little chlorine activation. On the other hand, models such as UMSLIMCAT, CMAM and NiwaSOCOL have a larger potential of chlorine activation than observed. Since Antarctic ozone loss is saturated in these models, ozone loss values do not exceed the range of observations. As for the Arctic, $Cl_x$ and PACl are well correlated for most of the models. Some models show a lower sensitivity of $Cl_x$ for a given PACl value compared other models, like CCSRNIES, CMAM and GEOSCCM. On the other hand UMSLIMCAT shows a slightly higher sensitivity of $Cl_x$ for a given PACl values. Note, chemical ozone loss was derived between July and mid-October. Continuous ozone depletion during the first weeks of October in the models might result in better agreement with observed ozone depletion, even if chemical ozone loss is delayed during winter/spring in some models.

In this section, only polar chemical ozone loss in the vortex core was evaluated to eliminate the impact on the inhomogeneous distributed ozone depletion in the entire vortex. Derived inhomogeneous ozone loss can be a result of an under-estimation of chemical ozone depletion at the vortex edge, caused by mixing across a too weak polar vortex edge. On the other hand, PACl was evaluated for the entire polar vortex.

## 6.4 Summary

This section gives a summary of the performance of the 18 CCMs, and the multi-model mean, in the comparisons described in Section 6.3. In the following summary, unless stated otherwise, "polar region" is defined as 79°S-89°S EqL and 350 K - 600 K. Note: One needs to be careful in comparing the HCl grades (Section 6.3.4.1) with the PACl grades below. A low grade for PACl does not mean that there was little chlorine activation. One can get a low grade for PACl with too much chlorine activation (see Section 6.3.4.3). In addition, the PACl is grade over the entire vortex, between 400 K - 550 K, where HCl is examined in the "polar region" (as defined above).

### 6.4.1 Summary by model

**Multi-Model Mean:** There are some chemistry diagnostics where the notion of the multi-model mean (MMM) is not useful or where the mean cannot be graded. Our photolysis comparison compared individual model results with a 'robust' model mean, rather than observations, and so the model mean already provided the benchmark. The PSS comparison is performed model by model; running the PSS code using the mean of the individual chemical species in the CCM schemes would not have any value given their different complexity, rate constants *etc*. Chemical schemes (and other CCM modules) are expected to conserve tracer families. Most CCMs exhibit this desirable behaviour while some others do not. For an analysis of this property, any mean which combines 'correct' models with 'incorrect' models is clearly going to be worse than the 'correct' models. The metrics where the MMM could be analysed are the following. For tracer-tracer correlations the MMM, like most of the CCMs, was good. For the reservoir chemistry the MMM scored relatively well; however, no model scored better than the MMM for all species and the MMM avoids any relatively low values. The MMM would also smooth out any errors in the partitioning of families in the individual CCMs. In the polar region, the MMM did a good job of representing the evolution of $HNO_3$, $H_2O$, and HCl. Most CCMs accurately represent chemical ozone loss in the Antarctic spring. There are clearly exceptions. Only a few models correctly represent the observed chemical ozone loss in the Arctic. This is reflected in the multi-model mean for this process, where the Antarctic is consistent with observations and the Arctic under-estimates chemical ozone loss.

**AMTRAC:** This model generally had a good performance on the photolysis inter-comparison; however there were exceptions for several important odd-oxygen production and loss Js (*e.g.*, J-$O_2$ and J-$Cl_2O_2$). This model did a very good job of representing the radical precursors and the radicals in the PSS section, with the exception of the $Cl_y$ *vs*. $N_2O$ relation and the $ClO/Cl_y$ ratio. Otherwise, it produced excellent tracer-tracer correlations. The model parameterises total chlorine and bromine loadings, so these could not be evaluated. The reservoir chemistry was generally well simulated except for HCl which appeared low. This may be due to a problem with the parameterised halogen loading. AMTRAC did not submit $HNO_3$ and HCl for the polar studies, so these species could not be evaluated there. $H_2O$ was included but was not well simulated in the lower polar region (model too low) although the model did better in the 600 K - 800 K range. The model's polar chemical ozone loss was well simulated in both the Antarctic and Arctic. However, for the Antarctic the chemical ozone loss matched observations at a lower PACl abundance relative to reanalyses. The SAD for the polar ozone loss analysis was not supplied and therefore based on the REF-B1 sulfate time-series. Profiles of SAD provided for the PSS comparisons showed significant differences compared to profiles used by other models, particularly at higher altitudes.

**CAM3.5:** This model did not participate in the photolysis inter-comparison; however, CAM3.5 uses the same LUT approach as WACCM (see comments below). This model did a good job of representing the radical precursors, with

the exception of $NO_y$ *vs*. $N_2O$. In the PSS comparison the model had a good representation of $O_x$, $HO_x$ and $BrO/Br_y$, with slightly poorer results for the $NO_x/NO_y$ and $ClO/Cl_y$ ratios. It had good tracer-tracer correlations except for $NO_y$ *vs*. $N_2O$ and $Br_y$ *vs*. $N_2O$. The reservoir chemistry was generally well simulated except for $ClONO_2$ and $N_2O_5$. CAM3.5 did well in representing $HNO_3$ in the polar region although less well in the 600 K - 800 K range (model too low). The model over dehydrates in the 350 K - 800 K region. This model also exhibited problems in the evolution of HCl (model too high) in the same high polar latitudes, suggesting it under-estimates chlorine activation. The model under-estimated polar chemical ozone loss in both the Antarctic and Arctic, consistent with too low chlorine activation. The sulfate SAD for the polar ozone loss calculation was supplied.

**CCSRNIES:** This model showed discrepancies (*versus* the multi-model mean) for all photolysis rates examined. The model did well in representing the precursors in the PSS section, with the exception of $Cl_y$ in the middle troposphere, and the abundance of total hydrogen *versus* $N_2O$. This model did well in representing most of the PSS radical diagnostics. This model has very good tracer-tracer correlations except for $CH_4$ *vs*. $H_2O$. This model had excessive levels of $Br_y$ in the troposphere and throughout the stratosphere due to inclusion of $CHBr_3$ in boundary conditions. Model levels of $Cl_y$ in the troposphere and lowermost stratosphere are quite high. The model has more inorganic chlorine and bromine in the stratosphere than expected based on the prescribed surface source gases. This indicates a lack of conservation in the model. The reservoir chemistry comparisons showed variable results. In particular, the upper stratosphere loading of HCl is very large due to the excess chlorine. This model had problems representing polar $HNO_3$. The model showed too much $HNO_3$ early in the winter and too little $HNO_3$ later in the winter/spring. The PACl analysis was good for the Antarctic but not for the Arctic. The polar chemical ozone loss was underestimated in the Antarctic. Little chemical ozone loss was derived in the Arctic. The sulfate SAD for the polar ozone loss calculation was supplied.

**CMAM:** Did not participate in the photolysis inter-comparison. The model did very well in representing the radical precursors and radicals in the PSS diagnostic. It also has very good tracer-tracer correlations, although values of total hydrogen ($H_{tot}$) tend to be lower than observation and most of the other models. The reservoir chemistry species appear to be well represented. It should be noted that this model does not represent the sedimentation of $HNO_3$ and $H_2O$ containing particles, but does represent an equilibrium partitioning of these species before they are used in the chemistry solver. This model does well in representing HCl in the polar region. The PACl analysis showed good results for the Antarctic but poorer agreement in the Arctic. The polar chemical ozone loss was also very well represented in the Antarctic. Little chemical ozone loss was derived in the Arctic, consistent with PACl in this region. The sulfate SAD for the polar chemical ozone loss was supplied.

**CNRM-ACM:** Did not participate in the photolysis intercomparison. This model did a very good job in representing the radical precursors in the PSS section, with the exception of $Cl_y$ in the troposphere and lowermost stratosphere (model values too high) and $H_{tot}$ (model has higher values than observed and than found in most other models). The model consistently did a very good job of representing radicals. The model has good tracer-tracer correlations and the reservoir chemistry appears to be well represented. The model shows a slight lack of conservation of total chlorine and total bromine in the mid- to upper stratosphere. This model did a good job representing $H_2O$ and HCl in the Antarctic polar region. However, the PACl analysis revealed large disagreement for both the Antarctic and Arctic, because of a very large variability in the PACl for the Antarctic and too warm temperatures in the Arctic. Chemical ozone loss was generally low in the Antarctic, even though the evolution of polar evolution HCl was adequately represented. Little chemical ozone loss was derived in the Arctic, consistent with PACl in this region. The sulfate SAD for the polar ozone loss calculation was supplied.

**E39CA:** Did not participate in the photolysis inter-comparison, the PSS comparison or the polar studies. The model has good tracer-tracer correlations, although we could not evaluate $NO_y$ *vs*. $N_2O$. The model appears to have a good representation of chlorine and nitrogen reservoir chemistry. This model does not include an explicit treatment of bromine chemistry, but we were unable to evaluate if and how this affects the performance of the model (*e.g.*, for polar ozone loss).

**EMAC:** This model performed well in the photolysis intercomparison. The model did a very good job of representing the radical precursors in the PSS section with the exception that the model under-estimated the abundance of $H_{tot}$. This model also did a good job of representing the radicals in the PSS evaluation. The model simulates good tracer-tracer correlations. The model simulates reservoir chemistry well. The model did not simulate polar $HNO_3$ well (model too high early in the winter) although $H_2O$ and HCl in the same region were better. The model's PACl analysis was good for both the Antarctic and Arctic. The polar chemical ozone loss was well represented in the Antarctic but slightly less loss in the Arctic. Large PACl values in the Arctic did not lead to apparent chemical ozone loss - this may be due to the vortex edge not being isolated and

resulting in mixing processes adding to the uncertainties in the tracer-tracer correlation method. This would result in an under-estimation of chemical ozone loss. This model under-estimated the chemical ozone loss in the Antarctic. The sulfate SAD was supplied for the polar ozone analysis.

**GEOSCCM:** This model performed very well in the photolysis inter-comparison. The model did a good job of representing precursors and radicals in the PSS evaluation. However, the model overestimated the $ClO/Cl_y$ ratio in the upper stratosphere and under-estimates the $Cl_y$ *vs*. $N_2O$ relation. The REF-B1 simulation was run using volcanically clean background aerosol loading, rather than the prescribed sulfate SAD climatology. This model produces good tracer-tracer correlations and appears to have a good description of reservoir chemistry. GEOSCCM did a good of representing the polar evolution of $HNO_3$, however it tended to overestimate $HNO_3$ abundances early in winter (June). This model did a very good job of representing $H_2O$ in the same region. HCl in the polar region was adequately represented, with the exception that the model had too much HCl in the 400 K - 425 K region relative to MLS. Overall, the model's Antarctic chemical ozone loss was consistent with observations. However, in this region, the chemical ozone loss was too large near the end of the winter, likely due to too large of ozone loss during the first half of October. The model did derive some chemical ozone loss in the Arctic, but less than observations would suggest.

**LMDZrepro:** This model performed very well in the photolysis inter-comparison. This model did a good job of representing the radical precursors in the PSS section, with the exceptions of the abundance of $H_{tot}$ *versus* $N_2O$ (model values low) and the $Br_y$ *versus* $N_2O$ diagnostic, which is due to the inclusion of a very short-lived source of $Br_y$. The model did an excellent job of representing the radical partitioning diagnostics in PSS section, although comparisons could not be performed for $O(^1D)$ and $O(^3P)$. The model produces good tracer-tracer correlations, except for $CH_4$ *vs*. $H_2O$ which illustrated a problem in modelled $H_2O$. The model has a reasonable representation of reservoir chemistry. In the polar region the modelled $HNO_3$ was too high but $H_2O$ was more realistic. In this same region the model did a good job representing the evolution of HCl. The PACl analysis gave good results for the Antarctic and Arctic. The modelled polar chemical ozone loss was also very good for both polar regions. The sulfate SAD for the polar chemical ozone loss calculation was supplied.

**MRI:** Did not participate in the photolysis inter-comparison. This model performed well in the radical precursor PSS section, with the exception that there was too much $Br_y$ present in the troposphere and throughout the stratosphere and too much $Cl_y$ in the troposphere and lowermost stratosphere. While the modelled stratospheric total chlorine loading followed the prescribed scenario, the model appeared to produce more inorganic bromine than expected based on specified halocarbons. The $N_2O$ *vs*. $NO_y$ diagnostic showed that model values of $NO_y$ are high in the lower stratosphere and low in the upper stratosphere. The model provided a good representation of $NO_x/NO_y$ and $BrO/Br_Y$ in the PSS evaluation, a fair representation of $O(^1D)$, $O(^3P)$, and $HO_x$, and a poor representation of $ClO/Cl_y$. The large overestimate of $ClO/Cl_y$ by this model is due, in part, to the neglect of HCl production by the ClO + OH reaction. Overall, this model received the lowest numerical score in the fast chemistry evaluation. However, tracer-tracer correlations were well simulated. This model performed relatively poorly in representing the evolution of $HNO_3$, but did a much better job of representing $H_2O$ and HCl in the polar region. The polar chemical ozone loss was very well simulated in both hemispheres. The sulfate SAD was not supplied for the polar chemical ozone loss calculation and therefore based on the REF-B1 sulfate time-series.

**NiwaSOCOL:** NiwaSOCOL provided joint results with SOCOL for the photolysis inter-comparison (see below). Did not participate in the PSS inter-comparisons. The model produced good tracer-tracer correlations except for $NO_y$ *vs*. $N_2O$. The model performed well for the reservoir chemistry. Modelled polar $HNO_3$ was good while the simulation of $H_2O$ was better. In the same region, overall, the model did a good job in representing the evolution of HCl. However, the model overestimated HCl in the 500 K - 600 K region. The PACl analysis was good for the Antarctic but poorer for the Arctic. The Arctic PACl values were very high in the vortex as a result of too large $H_2O$ in the NH for some winters. Polar chemical ozone loss was well simulated in the Antarctic but, to a lesser extent, the Arctic where only very little ozone loss was derived. The sulfate SAD was not supplied for the polar chemical ozone loss analysis and therefore based on the REF-B1 sulfate time-series.

**SOCOL:** This model performed well in the photolysis inter-comparison. This model did well in representing the $H_{tot}$ *vs*. $N_2O$ diagnostics in the PSS section. However, it performed much less well in representing the $Br_y$ *vs*. $N_2O$ relation in the stratosphere. Model values of $Cl_y$ and $Br_y$ are large throughout the troposphere and stratosphere, and in the upper stratosphere exceed the values expected from the prescribed halocarbon scenarios. This indicates a lack of mass conservation. The model did a good job for $HO_x$ diagnostic in the PSS section; model values of $NO_x/NO_y$, $ClO/Cl_y$, and $BrO/Br_y$ differ considerably from the benchmark (comparison for $O(^3P)$ and $O(^1D)$ could not be performed). Overall, the model did not fare well in the PSS evaluation. The model simulated good tracer-tracer correlations, except for $NO_y$ *vs*. $N_2O$, and has a good represen-

tation of reservoir chemistry. Modelled polar $HNO_3$ was good, while the simulation of $H_2O$ was better. In the same region, overall, the model did a good job in representing the evolution of HCl. However, the model overestimated HCl in the 500 K - 600 K region. The PACl analysis was good for the Antarctic but slightly less so for the Arctic. The simulation of polar chemical ozone loss was good for both regions. The sulfate SAD was not supplied for the polar chemical ozone loss analysis and therefore based on the REF-B1 sulfate time-series.

**ULAQ:** Did not participate in the photolysis inter-comparison. This model did a good job in representing the radical precursors in the PSS section with the exception of exhibiting large $Cl_y$ in the troposphere and throughout the lower stratosphere. The model also used a different sulfate SAD than what was prescribed for REF-B1. This model did a good job of representing $O(^3P)$, $O(^1D)$, $HO_x$, and $NO_x/NO_y$ for one time period of the PSS evaluation (Sept 1993), and a poor job of representing these species for the other time period (Feb 1996). The model did a fair job for the representation of the partitioning of $ClO/Cl_y$ and $BrO/Br_y$ for both time periods. It is not clear why this model represented fast chemistry much better for one time period than another time period; no other model exhibited such behaviour. The model simulated good tracer-tracer correlations. The model has a good description of reservoir chemistry though results for $HNO_3$ showed a larger disagreement. For the polar region the model performed fairly for $HNO_3$ (model too high) but better for $H_2O$. In the same region the model did well in representing the evolution of HCl. The PACl analysis was good for both the Antarctic and Arctic, and the simulated polar chemical ozone loss was also good for both regions. The sulfate SAD was supplied for the polar chemical ozone loss analysis.

**UMETRAC:** Did not participate in any of the Chapter 6 chemistry diagnostics. Some tracer fields were supplied late in the CCMVal process and were included in reservoir species figures where possible.

**UMSLIMCAT:** Performed well in the photolysis inter-comparison. This model did a good job in the radical and radical precursor diagnostics for the PSS section, except for the $Br_y$ *vs*. $N_2O$ relation. Values of $Br_y$ were higher than found by other models due to the inclusion of a source of very short-lived $Br_y$ (an additional 6 pptv of $Br_y$ was added). Comparisons could not be performed for $O(^3P)$ and $O(^1D)$. The model produced good tracer-tracer correlations. The model has a good description of reservoir chemistry although a slightly larger discrepancy existed for $ClONO_2$. This model had a good representation of $HNO_3$ (though model was too high) and $H_2O$ in the polar region. In the same region the model performed fairly well for HCl. The PACl results were good for the Antarctic and Arctic. The simulation of polar chemical ozone loss was also good for both regions (though note that the model run has larger $Br_y$). The sulfate SAD was not supplied for the polar chemical ozone loss analysis and therefore based on the REF-B1 sulfate time-series.

**UMUKCA-METO:** Did not participate in the photolysis inter-comparison. This model compared well in the radical precursor diagnostics in the PSS section with the exception that this model had too much $Cl_y$ at the tropopause and throughout the troposphere, due to errors in treating the rainout of HCl. This led to an excess of total chlorine throughout the stratosphere. The model did a good job of representing radicals in the PSS diagnostics. The model tended to overestimate stratospheric $NO_x/NO_y$ by a large amount and under-estimate stratospheric $HO_x$, also by a large amount. The comparisons for $O(^1D)$ could not be performed. The model produced good tracer-tracer correlations, except for $CH_4$ *vs*. $H_2O$. The model generally did a fair job of reservoir chemistry. In the polar region the model did a fair job of $HNO_3$ (model too high) but better for $H_2O$. In the same region the model was good at representing the evolution of HCl. The PACl analysis gave relatively poor results for the Antarctic and Arctic. The simulation of polar chemical ozone loss was good for the Antarctic but poorer for the Arctic. The sulfate SAD was not supplied for the polar chemical ozone loss and therefore based on the REF-B1 sulfate time-series. This model ran with a slightly different surface chlorine and bromine scenario to that prescribed for the REF-B2 run.

**UMUKCA-UCAM:** Did not participate in the photolysis inter-comparison, the PSS inter-comparison or the polar studies. However, this model is very similar to UMUKCA-METO and the performance of the chemical scheme should therefore be expected to be very similar. Chemical output could be analysed for the climatological comparisons. The model produced good tracer-tracer correlations. For the reservoir chemistry the model performed reasonably with the notable exception of $HNO_3$. An outstanding issue is the apparent differences in chemical behaviour with the METO version of UMUKCA for these climatological comparisons. Like UMUKCA-METO, this model ran with a slightly different surface chlorine and bromine scenario to that prescribed for the REF-B2 run.

**WACCM:** This model performed very well in the photolysis inter-comparison. The model did an excellent job representing radicals and radical precursors. Peak values of $NO_y$ are a bit lower than found in most of the other models and observed during Sept 1993. This model received the highest overall score in the fast chemistry metric. The model produced good tracer-tracer correlations and appears to

have a good description of reservoir chemistry. In the polar region WACCM was performed well in its representation of $HNO_3$ but less well for $H_2O$ (model too low). It should be noted that this model stayed denitrified too long into spring. In the same region the model was good in representing the evolution of HCl. The PACl comparison was good for the Antarctic but poorer for the Arctic where the PACl values were too large. The simulation of polar chemical ozone loss was very good for both the Antarctic and Arctic. The sulfate SAD was supplied for the polar chemical ozone loss analysis.

## 6.4.2 Overall Summary

This chapter is the first *major* attempt at quantifying the accuracy of different components of the stratospheric chemistry modules contained within global 3D CCMs. This work has shown some very good agreement, but at times significant discrepancies, in how the state-of-the-art CCMs represent radicals and their precursors.

A wide range of chemical observations are available for testing CCMs. However, the effective use of these observations sometime requires specific temporal sampling of the model runs. For example, satellite observations of key radicals for ozone loss are now available over many years but these species tend to have strong diurnal variations. Uncertainties in modelled polar ozone loss could be reduced by critical comparison with climatologies of polar ClO. Future CCM runs should look to sample the model to produce output files directly comparable to such observations.

## References


Bernath, P. F., C. T. McElroy, M. C. Abrams, C. D. Boone, M. Butler, C. Camy-Peyret, M. Carleer, C. Clerbaux, P.-F. Coheur, R. Colin, P. DeCola, M. DeMazière, J. R. Drummond, D. Dufour, W. F. J. Evans, H. Fast, D. Fussen, K. Gilbert, D. E. Jennings, E. J. Llewellyn, R. P. Lowe, E. Mahieu, J. C. McConnell, M. McHugh, S. D. McLeod, R. Michaud, C. Midwinter, R. Nassar, F. Nichitiu, C. Nowlan, C. P. Rinsland, Y. J. Rochon, N. Rowlands, K. Semeniuk, P. Simon, R. Skelton, J. J. Sloan, M.-A. Soucy, K. Strong, P. Tremblay, D. Turnbull, K. A. Walker, I. Walkty, D. A. Wardle, V. Wehrle, R. Zander, and J. Zou, 2005. Atmospheric Chemistry Experiment (ACE): Mission overview, *Geophys. Res. Lett.*, **32**, doi:10.1029/2005GL022386.

Cantrell, C. A., J. G. Calvert, A. Bais, R. E. Shetter, B. L. Lefer, and G. D. Edwards, Overview and conclusions of the International Photolysis Frequency Measurement and Modeling Intercomparison (IPMMI) study, *J. Geophys. Res.*, **108**, 8542, 2003.

Chang, A., R. J. Salawitch, H. A. Michelsen, M. R. Gunson, M. C. Abrams, R. Zander, C. P. Rinsland, M. Loewenstein, J. R. Podolske, M. H. Proffitt, J. J. Margitan, D. W. Fahey, R.-S. Gao, K. K. Kelly, J. W. Elkins, C. R. Webster, R. D. May, K. R. Chan, M. M. Abbas, A. Goldman, F. W. Irion, G. L. Manney, M. J. Newchurch and G. P. Stiller, 1996. A Comparison of Measurements from ATMOS and Instruments Aboard the ER-2 Aircraft: Tracers of Atmospheric Transport, *Geophys. Res. Lett.*, **23**, 2389-2392.

Christensen, L. E., M. Okumura, S. P. Sander, R. J. Salawitch, G. C. Toon, B. Sen, J.-F. Blavier, and K. W. Jucks, 2002. Kinetics of HO2 + HO2 → H2O2 + O2: Implications for stratospheric H2O2, *Geophys. Res. Lett.*, **29**, 10.1029/2001GL014525.

Dessler, A. E., 2002. The effect of deep, tropical convection on the tropical tropopause layer, *J. Geophys. Res.*, **107**, doi:10.1029/2001JD000511.

Douglass, A., M. Prather, T. Hall, S. Strahan, P. Rasch, L. Sparling, L. Coy, and J. Rodriguez, 1999. Choosing meteorological input for the global modeling initiative assessment of high-speed aircraft, *J. Geophys. Res.,* **104**, 27545-27564.

Evans, J.T., M.P. Chipperfield, H. Oelhaf, M. Stowasser, and G. Wetzel, 2003. Effect of near-IR photolysis of HO2NO2 on stratospheric chemistry, *Geophys. Res. Lett.*, **30**,, doi:10.1029/2002GL016470.

Eyring, V., N. R. P. Harris, M. Rex, T. G. Shepherd, D. W. Fahey, G. T. Amanatidis, J. Austin, M. P. Chipperfield, M. Dameris, P. M. De F. Forster, A. Gettelman, H. F. Graf, T. Nagashima, P. A. Newman, S. Pawson, M. J. Prather, J. A. Pyle, R. J. Salawitch, B. D. Santer, and D. W. Waugh, 2005. A strategy for process-oriented validation of coupled chemistry-climate models, *Bull. Am. Meteorol. Soc.*, **86**, 1117–1133.

Eyring, V., D. W. Waugh, G. E. Bodeker, E. Cordero, H. Akiyoshi, J. Austin, S. R. Beagley, B. Boville, P. Braesicke, C. Brühl, N. Butchart, M. P. Chipperfield, M. Dameris, R. Deckert, M. Deushi, S. M. Frith, R. R. Garcia, A. Gettelman, M. Giorgetta, D. E. Kinnison, E. Mancini, E. Manzini, D. R. Marsh, S. Mat-

thes, T. Nagashima, P. A. Newman, J. E. Nielsen, S. Pawson, G. Pitari, D. A. Plummer, E. Rozanov, M. Schraner, J. F. Scinocca, K. Semeniuk, T. G. Shepherd, K. Shibata, B. Steil, R. Stolarski, W. Tian, and M. Yoshiki, 2007. Multimodel projections of stratospheric ozone in the 21st century, *J. Geophys. Res.*, **112**, doi:10.1029/2006JD008332.

Fahey, D. W., S. G. Donnelly, E. R. Keim, R. S. Gao, R. C. Wamsley, L. A. Del Negro, E. L. Woodbridge, M. H. Proffitt, K. H. Rosenlof, M. K. W. Ko, D. K. Weisenstein, C. J. Scott, C. Nevison, S. Solomon and K. R. Chan, 1996. In situ observations of NOy, O3, and the NOy/O3 ratio in the lower stratosphere, *Geophys. Res. Lett.*, **23**, 1653-1656.

Froidevaux L., Y. B. Jiang, A. Lambert, N. J. Livesey, W. G. Read, J. W. Waters, R. A. Fuller, T. P. Marcy, P. J. Popp, R. S. Gao, D. W. Fahey, K. W. Jucks, R. A. Stachnik, G. C. Toon, L. E. Christensen, C. R. Webster, P. F. Bernath, C. D. Boone, K. A. Walker, H. C. Pumphrey, R. S. Harwood, G. L. Manney, M. J. Schwartz, W. H. Daffer, B. J. Drouin, R. E. Cofield, D. T. Cuddy, R. F. Jarnot, B. W. Knosp, V. S. Perun, W. V. Snyder, P. C. Stek, R. P. Thurstans, and P. A. Wagner, 2008. Validation of Aura Microwave Limb Sounder HCl measurements, *J. Geophys. Res.*, **113**, doi:10.1029/2007JD009025.

Gao, R.S., L. A. Del Negro, W. H. Swartz, R. J. Salawitch, S. A. Lloyd, M. H. Proffitt, D. W. Fahey, S. G. Donnelly, J. A. Neuman, R. M. Stimpfle, and T. P. Bui, 2001. J at high solar zenith angle in the lower stratosphere, *Geophys. Res. Lett.*, **28**, 2405-2408.

Hamill, T. M, J. S. Whitaker, 2005. Accounting for the error due to unresolved scales in ensemble data assimilation: A comparison of different approaches, *Mon. Wea. Rev.*, **133**, 3132 - 3147.

Hanson, D. R., and K. Mauersberger, 1998. Laboratory studies of the nitric acid trihydrate: Implications for the south polar stratosphere, *Geophys. Res. Lett.*, **15**, 855–858, doi:10.1029/88GL00209.

Hofzumahaus, A., B. L. Lefer, P. S. Monks, S. R. Hall, A. Kylling, B. Mayer, R. E. Shetter, W. Junkermann, A. Bais, J. G. Calvert, C. A. Cantrell, S. Madronich, G. D. Edwards, A. Kraus, M. Müller, B. Bohn, R. Schmitt, P. Johnston, R. McKenzie, G. J. Frost, E. Griffioen, M. Krol, T. Martin, G. Pfister, E. P. Röth, A. Ruggaber, W. H. Swartz, S. A. Lloyd, and M. Van Weele, 2004. Photolysis frequency of O3 to O(1D): Measurements and modeling during the International Photolysis Frequency Measurement and Modeling Intercomparison (IPMMI), *J. Geophys. Res.*, **109**, doi:10.1029/2003JD004333.

Jucks, K. W., D. G. Johnson, K. V. Chance, W. A. Traub, J. J. Margitan, G. B. Osterman, R. J. Salawitch, and Y. Sasano, 1998. Observations of OH, $HO_2$, $H_2O$, and $O_3$ in the upper stratosphere: implications for $HO_x$ photochemistry, *Geophys. Res. Lett.*, **25**, 3935-3938, doi:10.1029/1998GL900009.

Jucks, K. W., D. G. Johnson, K. V. Chance, W. A. Traub, and R. J. Salawitch, 1999. Nitric acid in the middle stratosphere as a function of altitude and aerosol loading, *J. Geophys. Res.*, **104**, 26,715-26,723.

Kawa, S.R., R.A. Plumb, and U. Schmidt, 1993. Simultaneous observations of long-lived species, Chapter H, The atmospheric effects of stratospheric aircraft: Report of the 1992 models and measurements workshop, NASA Ref. Publ. 1292, 352pp, NASA Goddard Space Flight Center, Greenbelt, MD,.

Kondo, Y., U. Schmidt, T. Sugita, A. Engel, M. Koike, P. Aimedieu, M.R. Gunson, and J. Rodriguez, 1996. NOy correlation with $N_2O$ and $CH_4$ in the midlatitude stratosphere, *Geophys. Res. Lett.*, **23**, 2369-2372.

Kovalenko, L. J., K. W. Jucks, R. J. Salawitch, G. C. Toon, J.-F. Blavier, D. G. Johnson, A. Kleinböhl, N. J. Livesey, J. J. Margitan, H. M. Pickett, M. L. Santee, B. Sen, R. A. Stachnik, and J. W. Waters, 2007. Observed and modeled HOCl profiles in the midlatitude stratosphere: Implications for ozone loss, *Geophys. Res. Lett.*, **34**, doi:10.1029/2007GL031100.

Lanzendorf, E. J., T. F. Hanisco, P. O. Wennberg, R. C. Cohen, R. M. Stimpfle, J. G. Anderson, R. S. Gao, J. J. Margitan, and T. P. Bui, 2001. Establishing the dependence of [HO2]/[OH] on temperature, halogen loading, O3, and NOx based on in situ measurements from the NASA ER-2, *J. Phys. Chem. A,* **105**, 1535–1542.

Lambert A., W. G. Read, N. J. Livesey, M. L. Santee, G. L. Manney, L. Froidevaux, D. L. Wu, M. J. Schwartz, H. C. Pumphrey, C. Jimenez, G. E. Nedoluha, R. E. Cofield, D. T. Cuddy, W. H. Daffer, B. J. Drouin, R. A. Fuller, R. F. Jarnot, B. W. Knosp, H. M. Pickett, V. S. Perun, W. V. Snyder, P. C. Stek, R. P. Thurstans, P. A. Wagner, J. W. Waters, K. W. Jucks, G. C. Toon,

R. A. Stachnik, P. F. Bernath, C. D. Boone, K. A. Walker, J. Urban, D. Murtagh, J. W. Elkins, and E. Atlas, 2007. Validation of the Aura Microwave Limb Sounder middle atmosphere water vapor and nitrous oxide measurements, *J. Geophys. Res.*, **112**, doi:10.1029/2007JD008724.

Lipson, J. B., T. W. Beiderhase, L. T. Molina, M. J. Molina, and M. Olzmann, 1999. Production of HCl in the OH + ClO reaction: Laboratory measurements and statistical rate theory calculations, *J. Phys. Chem. A*, **103**, 6540–6551.

Manney G. L., W. H. Daffer, J. M. Zawodny, P. F. Bernath, K. W. Hoppel, K. A. Walker, B. W. Knosp, C. Boone, E. E. Remsberg, M. L. Santee, V. L. Harvey, S. Pawson, D. R. Jackson, L. Deaver, C. T. McElroy, C. A. McLinden, J. R. Drummond, H. C. Pumphrey, A. Lambert, M. J. Schwartz, L. Froidevaux, Sean McLeod, L. L. Takacs, M. J. Suarez, Charles R. Trepte, D. C. Cuddy, N. J. Livesey, R. S. Harwood, and J. W. Waters, 2007. Solar occultation satellite data and derived meteorological products: Sampling issues and comparisons with Aura Microwave Limb Sounder, *J. Geophys. Res.*, **112**, doi:10.1029/2007JD008709.

McElroy, M. B., and R. J. Salawitch, 1989. Changing composition of the global stratosphere, *Science*, **243**, 763–770.

Michelangeli, D. V., M. Allen, and Y. L. Yung, 1989. El Chichon volcanic aerosols: impact of radiative, thermal, and chemical perturbations, *J. Geophys Res.*, **94**, 18,429-18,443.

Millard, G. A., A. M. Lee, and J. A. Pyle, 2002. A model study of the connection between polar and midlatitude ozone loss in the Northern Hemisphere lower stratosphere, *J. Geophys. Res.*, **107**, doi:10.1029/2001JD000899.

Müller, R., P. J. Crutzen, J.-U. Grooss, C. Bruehl, J. M. Russell II, H. Gernandt, D. S. McKenna and A. F. Tuck, 1997. Severe chemical ozone loss in the Arctic during the winter of 1995-1996, *Nature*, **389**, 709-712.

Müller, R. and R. J. Salawitch (lead authors), P. J. Crutzen, W. A. Lahoz, G. L. Manney, and R, Toumi, Chapter 6: Upper Stratospheric Processes, Scientific Assessment of Ozone Depletion: 1998, World Meteorological Organization, Global ozone research and monitoring project, Report No. 44, Geneva, Switzerland, 1999.

Müller, R., S. Tilmes, P. Konopka, J.-U. Grooß, and H.-J. Jost, 2005. Impact of mixing and chemical change on ozone-tracer relations in the polar vortex, *Atmos. Chem. Phys.*, **5**, 3139–3151.

Müller, R., J.-U. Grooß , C. Lemmen, D. Heinze, M. Dameris, and G. Bodeker, 2008. Simple measures of ozone depletion in the polar stratosphere, *Atmos. Chem. Phys.*, **8**, 251–264.

Murtagh, D., U. Frisk, F. Merino, M. Ridal, A. Jonsson, J. Stegman, G. Witt, P. Eriksson, C. Jiménez, G. Megie, J. de la Noë, P. Ricaud, P. Baron, J. R. Pardo, A. Hauchcorne, E. J. Llewellyn, D. A. Degenstein, R. L. Gattinger, N. D. Lloyd, W. FJ Evans, I. C. McDade, C. S. Haley, C. Sioris, C. von Savigny, B. H. Solheim, J. C**.** McConnell, K. Strong, E. H. Richardson, G. W. Leppelmeier, E. Kyrölä, H. Auvinen, and L. Oikarinen, 2002. An overview of the Odin atmospheric mission, *Can. J. Phys.*, **80**, 309-319.

Nash, E. R., P. A. Newman, J. E. Rosenfield, and M. R. Schoeberl, 1996. An objective determination of the polar vortex using Ertel's potential vorticity, *J. Geophys. Res.*, **101**, 9471–9478.

Newman, P. A., E. R. Nash, S. R. Kawa, S. A. Montzka, and S. M. Schauffler, 2006. When will the Antarctic ozone hole recover?, *Geophys. Res. Lett.*, **33**, doi:10.1029/2005GL025232.

Newman, P. A., J. S. Daniel, D. W. Waugh, and E. R. Nash, 2007. A new formulation of equivalent effective stratospheric chlorine (EESC), *Atmos. Chem. Phys.*, **7**, 4537–4552.

Osterman, G. B., R. J. Salawitch, B. Sen, G. C. Toon, R. A. Stachnik, H. M. Pickett, J. J. Margitan, J.-F. Blavier, and D. B. Peterson., 1997. Balloon-borne measurements of stratospheric radicals and their precursors: implications for the production and loss of ozone, *Geophys. Res. Lett.,* **24**, 1107–1110.

Osterman, G. B. B. Sen, G. C. Toon, R. J. Salawitch, J. J. Margitan, J.-F. Blavier, D. W. Fahey, and R. S. Gao, 1999. Partitioning of NOy species in the summer Arctic stratosphere, *Geophys. Res. Lett.*, **26**, 1157-1160.

Park, J.H., et al., Models and Measurements Intercomparison II, NASA/TM-1999-209554, 1999.

Peter, T., 1997. Microphysics and heterogeneous chemistry

of polar stratospheric clouds, *Ann. Rev. Phys. Chem.*, **48**, 785-822.

Pierson, J., S. Kawa, R. Salawitch, T. Hanisco, E. Lanzendorf, K. Perkins, and R. Gao, 2000. Influence of air mass histories on radical species during the Photochemistry of Ozone Loss in the Arctic Region in Summer (POLARIS) mission, *J. Geophys. Res.*, **105**, 15,185-15,199.

Prather, M.J. and E.E. Remsberg, (eds.), 1993. Report of the 1992 Stratospheric Models and Measurements Workshop, Satellite Beach, FL, February 1992, NASA Ref. Publ. 1292, 144+268+352 pp.

Proffitt, M. H., K. Aikin, J. J. Margitan, M. Loewenstein, J. R. Podolske, A. Weaver, K. R. Chan, H. Fast, and J. W. Elkins, 1993. Ozone loss inside the northern polar vortex during the 1991-1992 winter, *Science*, **261**, 1150–1154.

Pundt, I., J.-P. Pommereau, M. P. Chipperfield, M. Van Roozendael, and F. Goutail, 2002. Climatology of the stratospheric BrO vertical distribution by balloon-borne UV–visible spectrometry, *J. Geophys. Res.*, **107**, doi:10.1029/2002JD002230.

Rex, M., R. J. Salawitch, P. von der Gathen, N. R. Harris, M. P. Chipperfield, and B. Naujokat, 2004. Arctic ozone loss and climate change, *Geophys. Res. Lett.*, **31**, doi:10.1029/2003GL018844.

Rinsland, C.P., E. Mathieu, R. Zander, N.B. Jones, M.P Chipperfield, A. Goldman, J. Anderson, J.M. Russell, P. Demoulin, J. Notholt, G.C. Toon, J.F. Blavier, B. Sen, R. Sussmann, S.W. Wood, A. Meier, D.W.T. Griffith, L.S. Chiou, F.J. Murcray, T.M. Stephen, F. Hase, S. Mikuteit, A. Schulz, and T. Blumenstock, 2003. Long-term trends of inorganic chlorine from ground-based infrared solar spectra: Past increases and evidence for stabilization, *J. Geophys. Res.*, **108**, doi:10.1029/2002JD003001.

Rozanov, A., H. Bovensmann, A. Bracher, S. Hrechanyy, V. Rozanov, M. Sinnhuber, F. Stroh and J.P. Burrows, 2005. $NO_2$ and BrO vertical profile retrieval from SCIAMACHY limb measurements: Sensitivity studies, *Adv. Space Res.*, **36**, 846-854.

Salawitch, R. J., S. C. Wofsy, P. O. Wennberg, R. C. Cohen, J. G. Anderson, D. W. Fahey, R. S. Gao, E. R. Keim, E. L. Woodbridge, R. M. Stimpfle, J. P. Koplow, D. W. Kohn, C. R. Webster, R. D. May, L. Pfister, E. W. Gottlieb, H. A. Michelsen, G. K. Yue, J. C. Wilson, C. A. Brock, H. H. Jonsson, J. E. Dye, D. Baumgardner, M. H. Proffitt, M. Loewenstein, J. R. Podolske, J. W. Elkins, G. S. Dutton, E. J. Hintsa, A. E. Dessler, E. M. Weinstock, K. K. Kelly, K. A. Boering, B. C. Daube, K. R. Chan, and S. W. Bowen, 1994a. The distribution of hydrogen, nitrogen, and chlorine radicals in the lower stratosphere: implications for changes in $O_3$ due to emission of $NO_y$ from supersonic aircraft, *Geophys. Res. Lett.*, **21**, 2543–2546.

Salawitch, R. J., S. C. Wofsy, P. O. Wennberg, R. C. Cohen, J. G. Anderson, D. W. Fahey, R. S. Gao, E. R. Keim, E. L. Woodbridge, R. M. Stimpfle, J. P. Koplow, D. W. Kohn, C. R. Webster, R. D. May, L. Pfister, E. W. Gottlieb, H. A. Michelsen, G. K. Yue, J. C. Wilson, C. A. Brock, H. H. Jonsson, J. E. Dye, D. Baumgardner, M. H. Proffitt, M. Loewenstein, J. R. Podolske, J. W. Elkins, G. S. Dutton, E. J. Hintsa, A. E. Dessler, E. M. Weinstock, K. K. Kelly, K. A. Boering, B. C. Daube, K. R. Chan, and S. W. Bowen, 1994b. The diurnal variation of hydrogen, nitrogen, and chlorine radicals: implications for the heterogeneous production of HNO2, *Geophys. Res. Lett.*, **21**, 2547–2550.

Salawitch, R. J., P. O. Wennberg, G. C. Toon, B. Sen, and J.-F. Blavier, 2002. Near IR photolysis of HO2NO2: Implications for HOx, *Geophys. Res. Lett.*, **29**, doi:10.1029/2002GL015006.

Salawitch, R. J., D. K. Weisenstein, L. J. Kovalenko, C. E. Sioris, P. O. Wennberg, K. Chance, M. K. W. Ko, and C. A. McLinden, 2005. Sensitivity of ozone to bromine in the lower stratosphere, *Geophys. Res. Lett.*, **32**, doi:10.1029/2004GL021504.

Sander, S. P., et al.,Chemical Kinetics and Photochemical Data for Use in Atmospheric Studies, Evaluation No. 14, JPL Publication 02-25, Jet Propulsion Lab, Pasadena, CA, 2003.

Sander, S. P. et al., Chemical Kinetics and Photochemical Data for Use in Atmospheric Studies, Evaluation Number 15, JPL Publication 06-02, Jet Propulsion Laboratory, Pasadena, Calif., 2006.

Santee M. L., A. Lambert, W. G. Read, N. J. Livesey, R. E. Cofield, D. T. Cuddy, W. H. Daffer, B. J. Drouin, L. Froidevaux, R. A. Fuller, R. F. Jarnot, B. W. Knosp, G. L. Manney, V. S. Perun, W. V. Snyder, P. C. Stek, R. P. Thurstans, P. A. Wagner, J. W. Waters, G. Muscari, R. L. de Zafra, J. E. Dibb, D. W. Fahey, P. J. Popp, T. P. Marcy, K. W. Jucks, G. C. Toon, R. A. Stachnik,

P. F. Bernath, C. D. Boone, K. A. Walker, J. Urban, and D. Murtagh, 2007. Validation of the Aura Microwave Limb Sounder HNO3 measurements, *J. Geophys. Res.*, **112**, doi:10.1029/2007JD008721.

Sen, B., G. C. Toon, G. B. Osterman, J.-F. Blavier, J. J. Margitan, R. J. Salawitch, and G. K. Yue, 1998. Measurements of reactive nitrogen in the stratosphere, *J. Geophys. Res.*, **103**, 3571-3585.

Sen, B., G. B. Osterman, R. J. Salawitch, G. C. Toon, J. J. Margitan, J.-F. Blavier, A. Y. Chang, R. D. May, C. R. Webster, R. M. Stimpfle, G. P. Bonne, P. B. Voss, K. K. Perkins, J. G. Anderson, R. C. Cohen, J. W. Elkins, G. S. Dutton, D. F. Hurst, P. A. Romashkin, E. L. Atlas, S. M. Schauffler, and M. Loewenstein, 1999. The budget and partitioning of stratospheric chlorine during the 1997 Arctic summer, *J. Geophys. Res.*, **104**, 26,653-26,665.

Sinnhuber, B.-M., A. Rozanov, N. Sheode, O. T. Afe, A. Richter, M. Sinnhuber, F. Wittrock, J. P. Burrows, G. P. Stiller, T. von Clarmann, and A. Linden, 2005. Global observations of stratospheric bromine monoxide from SCIAMACHY, *Geophys. Res. Lett.*, **32**, doi:10.1029/2005GL023839.

Solomon, S., R. R. Garcia, F.S. Rowland and D.J. Wuebbles, 1998. On the depletion of Antarctic ozone, *Nature*, **321**, 755–758.

Solomon, S., Stratospheric ozone depletion: A review of concepts and history, *Rev. Geophys.*, **37**, 275–316, 1999.

Thomason, L. W., L. R. Poole, and T. Deshler, A global climatology of stratospheric aerosol surface area density deduced from Stratospheric Aerosol and Gas Experiment II measurements: 1984-1994, *J. Geophys. Res.*, **102**, 8967-8976, 1997.

Tilmes, S., R. Müller, J.-U. Grooß, and J. M. Russell, 2004. Ozone loss and chlorine activation in the Arctic winters 1991–2003 derived with the tracer-tracer correlations, *Atmos. Chem. Phys.*, **4**, 2181–2213.

Tilmes, S., R. Müller, A. Engel, M. Rex, and J. M. Russell III, 2006. Chemical ozone loss in the Arctic and Antarctic stratosphere between 1992 and 2005, *Geophys. Res. Lett.*, **33**, doi:10.1029/2006GL026925.

Tilmes, S., E. D. Kinnison, R. R. Garcia, R. Mueller, B. A. Boville, F. Sassi, D. R. Marsh, 2007. Evaluation of heterogeneous processes in the polar lower stratosphere in WACCM3, *J. Geophys. Res.*, **112**, doi:10.1029/2006JD008334.

Tilmes, S., R. Müller, and R. Salawitch, 2008. The sensitivity of polar ozone depletion to proposed geoengineering schemes, *Science*, **320**, 1201-1204, doi:10.1126/science.1153966.

Wamsley, P. R., J. W. Elkins, D. W. Fahey, G. S. Dutton, C. M. Volk, R. C. Myers, S. A. Montzka, J. H. Butler, A. D. Clarke, P. J. Fraser, L. P. Steele, M. P. Lucarelli, E. L. Atlas, S. M. Schauffler, D. R. Blake, F. S. Rowland, W. T. Sturges, J. M. Lee, S. A. Penkett, A. Engel, R. M. Stimpfle, K. R. Chan, D. K. Weisenstein, M. K. W. Ko, and R. J. Salawitch, 1998. Distribution of halon-1211 in the upper troposphere and lower stratosphere and the 1994 total bromine budget, *J. Geophys. Res.*, **103**, 1513–1526.

Waters, J. W., et al., The Earth Observing System Microwave Limb Sounder (EOS MLS) on the Aura Satellite, IEEE Trans. Geosci. Remote Sensing, 44, no. 5, 1075-1092, 2006.

Waugh, D. and V. Eyring, 2008. Quantitative performance metrics for stratospheric-resolving chemistry-climate models, *Atmos. Chem. Phys.*, **8**, 5699-5713.

Weinstock, E. M., E. J. Hintsa, D. B. Kirk-Davidoff, J. G. Anderson, A. E. Andrews, R. L. Herman, C. R. Webster, M. Loewenstein, J. R. Podolske, and T. P. Bui, 2001. Constraints on the seasonal cycle of stratospheric water vapor using in situ measurements from the ER-2 and a CO photochemical clock, *J. Geophys. Res.*, **106**, 22,707–22,724.

Wennberg, P.O., R. C. Cohen, R. M. Stimpfle, J. P. Koplow, J. G. Anderson, R. J. Salawitch, D. W. Fahey, E. L. Woodbridge, E. R. Keim, R. S. Gao, C. R. Webster, R. D. May, D. W. Toohey, L. M. Avallone, M. H. Proffitt, M. Loewenstein, J. R. Podolske, K. R. Chan, and S. C. Wofsy, 1994. Removal of stratospheric ozone by radicals: in situ measurements of OH, HO2, NO, NO2, ClO, and BrO, *Science,* **266**, 398-404.

Wennberg, P. O. R. J. Salawitch, D. J. Donaldson, T. F. Hanisco, E. J. Lanzendorf, K. K. Perkins, S. A. Lloyd, V. Vaida, R. S. Gao, E. J. Hintsa, R. C. Cohen, W. H. Swartz, T. L. Kusterer, and D. E. Anderson, 1999. Twilight observations suggest unknown sources of HOx, *Geophys. Res. Lett.,* **26**, 1373-1376.

Whitaker, J.S., T.M. Hamill, X. Wei, Y. Song and Z. Toth, 2008. Ensemble data assimilation with the NCEP global forecast system, *Mon. Wea. Rev.*, **136**, 463-

482.

Wild, O., X. Zhu, M.J. Prather, 2000. Fast-J: Accurate simulation of in- and below-cloud photolysis in tropospheric chemical models, *J. Atmos. Chem.*, **37**, 245-282.

World Meteorological Organization (WMO)/United Nations Environment Programme (UNEP), 2007. *Scientific Assessment of Ozone Depletion: 2006*, World Meteorological Organization, Global Ozone Research and Monitoring Project, Report No. 50, Geneva, Switzerland.

Woodbridge, E. L., J. W. Elkins, D. W. Fahey, L. E. Heidt, S. Solomon, T. J. Baring, T. M. Gilpin, W. H. Pollock, S. M. Schauffler, E. L. Atlas, M. Loewenstein, J. R. Podolske, C. R. Webster, R. D. May, J. M. Gilligan, S. A. Montzka, K. A. Boering, and R. J. Salawitch, 1995. Estimates of total organic and inorganic chlorine in the lower stratosphere from in situ and flask measurements during AASE II, *J. Geophys. Res.*, **100**, 3057–3064.